FABRICATION AND MICROSTRUCTURAL CONTROL OF ADVANCED CERAMIC COMPONENTS BY THREE DIMENSIONAL PRINTING

by

Jaedeok Yoo

B.S. Metallurgical Engineering and Materials Science, Carnegie Mellon University, 1991

Submitted to the Department of Materials Science and Engineering in
Partial Fulfillment of the Requirements for the Degree of

DOCTOR OF PHILOSOPHY IN CERAMICS

at the

Massachusetts Institute of Technology

September, 1996

Signature of Author _____
Department of Materials Science and Engineering
August 9, 1996

Certified by _____
Professor Michael J. Cima
Norton Professor of Ceramics
Thesis Supervisor

Accepted by _____
Professor Linn W. Hobbs
John F. Elliot Professor of Materials
Chairman, Departmental Committee on Graduate Students

FABRICATION AND MICROSTRUCTURAL CONTROL OF ADVANCED CERAMIC COMPONENTS BY THREE DIMENSIONAL PRINTING

Jaedeok Yoo

Submitted to the Department of Materials Science and Engineering
on August 9, 1996 in partial fulfillment of the
requirements for the Degree of Doctor of Philosophy

ABSTRACT

Three Dimensional Printing (3DP) is a solid freeform fabrication technique to manufacture functional prototypes directly from computer models. 3D-printed monolithic structural ceramic parts such as alumina, zirconia toughened alumina, and glass ceramic parts exhibit mechanical properties comparable to conventionally processed materials. Moreover, 3DP has a unique ability to place second phase matter within a component in a precisely controlled fashion. Thus, any macroscopically complex shaped parts can be made with user-defined microstructures. Zirconia toughened alumina (ZTA) system was chosen to exercise this spatial control of composition. Stability of each zirconia particles in the alumina matrix is controlled by the local compositional variation caused by the selective deposition of stabilizer. ZTA components with designed phase distribution were fabricated by 3DP process. These components include compositionally graded multilayer stacks, specimens with compressive surface, and compression test specimen with shielded notch tips.

Mechanical properties of 3D-printed monolithic ZTA specimens were comparable to that of conventionally prepared ZTA. 3D-printed tetragonal ZTA (t-ZTA) showed flexural strength of 670 MPa and fracture toughness of 4 MPa $\sqrt{m}$. Coefficient of thermal expansion of 3D-printed t-ZTA and monoclinic ZTA (m-ZTA) were $9.2 \times 10^{-6}/°C$ and 8.4×10^{-6}, respectively, which are similar to that of conventionally prepared ZTA. The strain associated with the monoclinic to tetragonal transformation was measured as 1.75×10^{-3}. These characteristics were used to design compositional gradients in 3DP ZTA specimens. X-ray diffraction techniques were used to confirm the proportion of each zirconia phase present at various locations of 3D-printed ZTA components. The results show that 3DP's selective doping technique is effective in controlling the local distribution of zirconia polymorphs. This was also evident from the mechanical testing of ZTA components with surface compression. The residual compressive stress, designed and placed by 3DP, caused the flexural strength to increase by 25% from that of the monolithic ZTA specimens. Compression tests of notched ZTA specimens also demonstrated that microstructure and properties can be designed and fabricated by 3DP.

Thesis Supervisor: Prof. Michael J. Cima
Title: Norton Professor of Ceramics

DEDICATION

To Jean, for your love and encouragement

.

ACKNOWLEDGMENTS

TABLE OF CONTENTS

LIST OF FIGURES

13

LIST OF TABLES

1. Introduction

1.1 SOLID FREEFORM FABRICATION

Computer Aided Design (CAD) has become an integral part of product development for variety of industries. CAD eliminates many time-consuming steps and drastically increases productivity in design process. Designers can accelerate development processes further by incorporating computers to fabricate prototypes. Solid Freeform Fabrication (SFF) methods use CAD models of solid objects to build three dimensional components.[1-4] A wide range of materials are used by current SFF processes. Each SFF process has unique forming principles, but most are fundamentally different from conventional manufacturing processes. Most conventional techniques use either deformation (e.g., forging, slip casting, injection molding) or removal (e.g., milling, grinding, drilling) processes to manufacture solid objects. In contrast, SFF processes involve building objects in a laminated fashion through sequential addition of patterned thin layers.[5-7] The information needed to form these 2-D segment is obtained by calculating the intersection of a series of planes with the CAD rendering of the object. This approach is fundamentally different from numeric controlled machining where the selection of tools and calculation of tool paths can limit the topologies that can be generated.

SFF also dramatically reduces the time required to prepare the first prototype part. Usual lead-time for any parts in SFF processes is in the order of hours while it could take months to prepare prototypes through conventional techniques. SFF processes are also cost-effective. Conventionally prepared structural ceramic prototypes involve very expensive tooling prepared by machining. Therefore, elimination of the machining step dramatically reduces the cost for each advanced ceramic component. SFF processes can also eliminate strength limiting flaws associated with conventional forming techniques. Thus, low-cost functional ceramic prototypes can be fabricated by SFF.

The additive nature of these processes leads to remarkable flexibility in shape of the components that can be fabricated. This flexibility is the justification for calling these

processes solid "free-form" fabrication methods. Cavities, overhangs, undercuts, etc. are resolved into multiple 2-D patterning problems. Another advantage of SFF processes over conventional manufacturing methods is the control over both the macrostructure and microstructure. One can utilize the SFF processes to create parts with layered composite structures, localized compositional variation, anisotropic mechanical and/or thermal properties, and microengineered porosity.

SFF processes can be divided into three categories: methods that involve the combination of addition and removal of matter, processes that deposit energy to fuse materials, and processes that deposit matter to form objects. Variations on each of the major processes depicted here exist and detailed descriptions are available through many other publications.[1-8]

1.1.1 ADDITION/REMOVAL COMBINATION

Laminated Object Manufacturing

Laminated object manufacturing (LOM) uses a combination of addition and subtraction of matter to build arbitrary three dimensional objects.[9-11] Starting material in the form of sheets are stacked and laminated to the previous layers in order to build three dimensional objects. Individual layers are cut by directing a CO_2 laser beam over the surface of each layer. Information from the CAD file is used to determine the path and speed of the laser beam. The scan speed is tightly controlled to ensure that the laser beam does not cut through more than a layer thickness, thus, damaging previous layers. It is also necessary to use the laser to cut a rectilinear pattern in all the material that is *external* to the final component. This facilitates the final part removal since the matrix material is now diced into small tiles. The LOM process is illustrated in Figure 1.1.

The LOM process has been implemented to produce components out of paper. These paper models are used to test ergonomic design, or fit, in the same fashion as the prototypes made of foams or card board. Other materials can be directly produced from LOM. For example, LOM-derived ceramic parts have been produced by using tape cast ceramic sheets[10]. These sheets consist of a polymer matrix in which fine ceramic

particles are dispersed. The sheets are easily cut in the path of the laser since the polymer decomposes at high temperature. The resulting polymer-ceramic part is then fired to burn away the polymer and to sinter the ceramic powder to form a dense object.
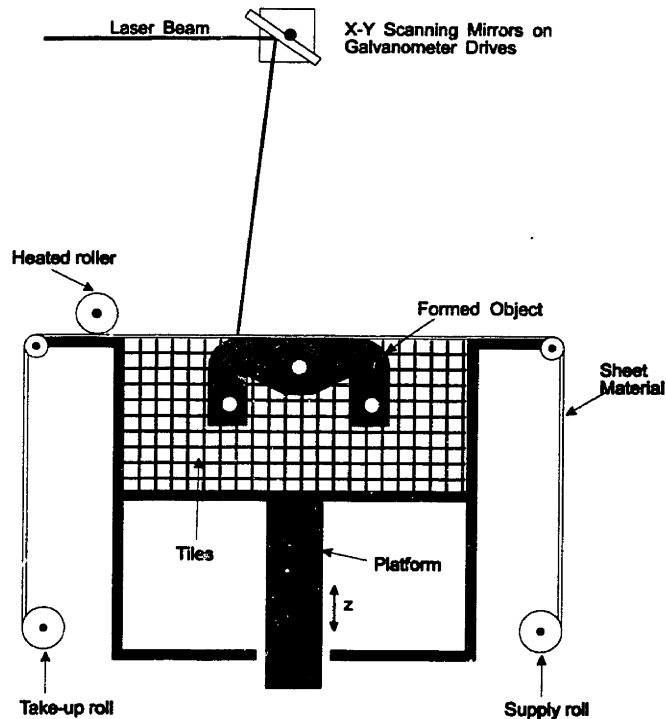
Figure 1.1:   Laminated object manufacturing (LOM) builds components by laminating and cutting roll stock of material.

The LOM process can be adapted easily to create structures with locally controlled composition. One needs to prepare tape cast sheets with varying proportions of two materials, for example, to build compositionally graded structures.[12] Components with very complex geometries can be built by LOM. Compositional gradients in LOM components are however, restricted to be along the build-axis.

1.1.2 DEPOSITION OF ENERGY

Stereolithography

Stereolithography uses lasers to selectively cure resins in a laminated fashion to build complex shapes[7,13]. A schematic of the stereolithography process is shown in Figure 1.2. Thin layers of liquid photopolymer are spread and a laser beam is tracked over the surface of the reservoir. Curing of the resin is initiated by the laser, and only the

region which was exposed to the beam undergoes polymerization. A new layer of liquid is spread as the cured component is lowered by a small increment. The speed of the laser scan and intensity of the beam determine the depth of polymerization. The uncured resin is drained to reveal the completed part once laser scanning is completed. The uncured liquid medium in stereolithography facilitates part removal. Complexities occur, however, when building complex shapes. Components with such features as overhangs or undercuts can only be built with temporary support structures. These features would be temporarily unsupported during the build operation if it were not for the addition of these temporary "struts".[13]
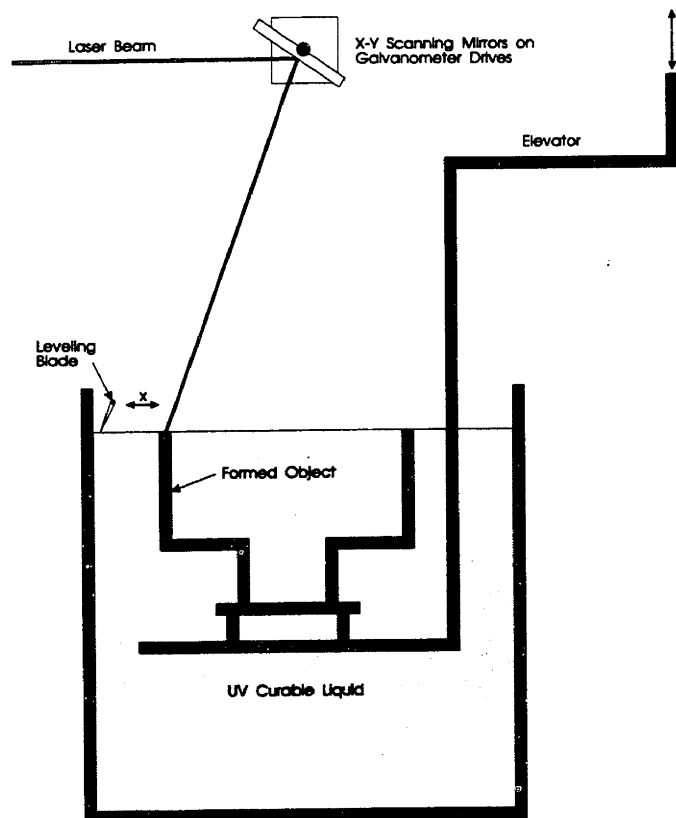
Figure 1.2:   Stereolithography uses laser light to locally initiate polymerization in a resin bath.

Many commercially available stereolithography machines are used to produce acrylic or epoxy components for prototyping applications. Some of these components are also used as the master patterns for casting processes and have proven to effectively

reduce the lead time for new products. Although most of the work in stereolithography has been with resin parts, experiments with ceramic-filled resins have also been reported. Researchers at the University of Michigan have dispersed ceramic particles in special polymerizable resins and built components on stereolithography machines[14]. Composite structures made of resin and ceramic particles are then fired to decompose resin and fully densify the ceramic. It is conceivable that components with varying composition could be fabricated by loading resins with various material systems. Structures with one dimensional compositional gradient may be constructed just as might be done with LOM.
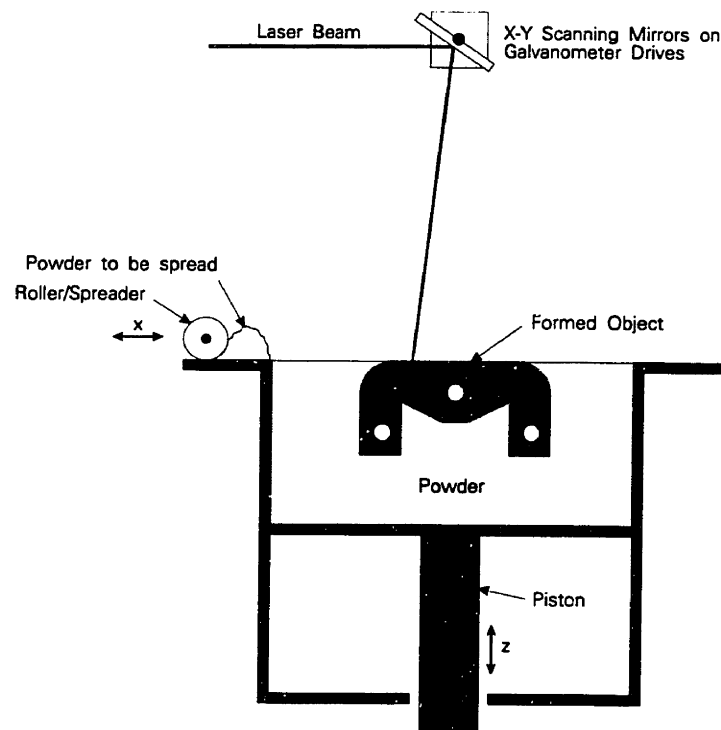
Figure 1.3: Selective laser sintering (SLS) builds parts from fusible powder. Laser light fuses the powder by locally heating the surface of a powder bed.

Selective Laser Sintering

Selective laser sintering (SLS) also uses a laser. In this case, laser energy is directed toward the surface of the layer to initiate localized bonding.[15-16] The bonding mechanism for SLS, unlike stereolithography, involves partial melting and fusing of granular thermoplastic material. Granular material is spread in thin layers and the laser beam is traced over the surface of the powder bed as shown in Figure 1.3. This causes melting of the thermoplastic material in regions of the powder bed exposed to laser light.

Subsequent resolidification causes local bonding of the granular material within a layer and to the layer below. Powder spreading and the laser scanning steps are repeated until the part is completed. Part retrieval is performed by simply brushing away the loose granules since the area not exposed to the laser remains unsolidified. Unlike the stereolithography process, support structures are not required since the packed granules are rigid enough to prevent the solidified portions from moving.

Structures with compositional variation may be created by SLS in the same fashion as LOM and stereolithography. Green bodies containing compositional gradients may be built by spreading powder mixtures of varying composition.

1.1.3 DEPOSITION OF MATTER

Three Dimensional Printing

Three Dimensional Printing (3DP) uses ink jet printing technology to selectively bind particulates and form objects.[17-19] A schematic for a typical 3DP process is shown in Figure 1.4. A thin layer of a powder is spread in a box, and then printhead assembly scans over the powderbed, depositing binder droplets on selected regions. 3DP employs ink-jet printing technology to generate and place binder droplets. A continuous binder jet is broken into small droplets by piezo-driven vibration of the nozzle. Binder droplets are selectively charged to allow the deflection and collection of undesired droplets. Thus, the uncharged droplets selectively bind the particulate medium beneath the nozzle assembly. (Figure 1.5) The floor of the power box drops down to spread new powder once a layer has been "printed". Information for the next layer is relayed from computer and is then printed. These steps are repeated until the last layer is printed. The binder locally bonds the powder within the layer and to the layer below. Loose powder is then removed to reveal the 3D printed green body, which is then ready for post-printing processes designed to strengthen and densify the component.
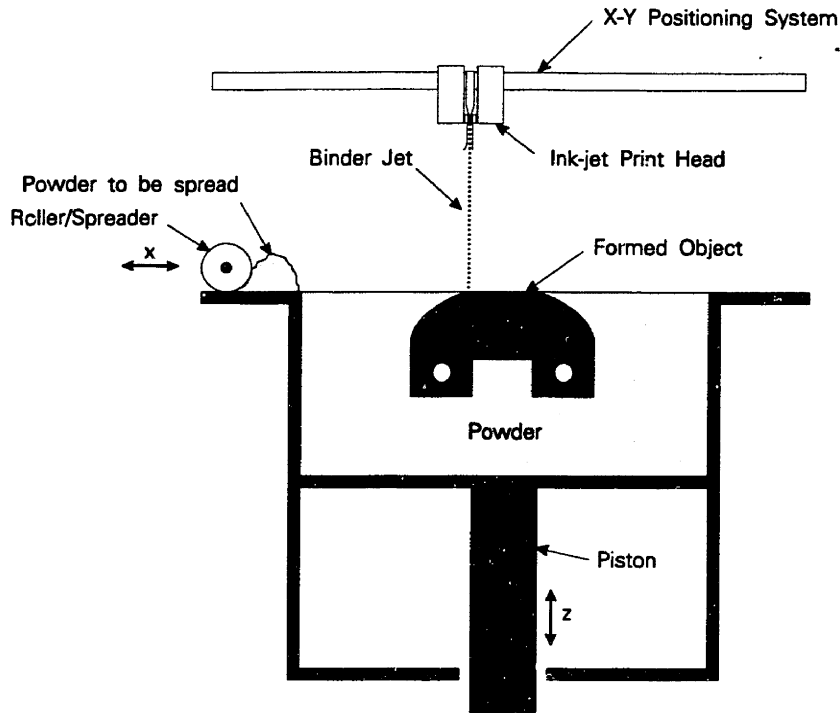
Figure 1.4: Three dimensional printing (3DP) builds parts by ink-jet printing binder into a powder bed. The resulting green bodies are then processed by conventional powder component manufacturing methods.

The 3DP has been used to produce complex components with wide range of material systems including ceramic[20], glass[21], metal[22], and polymer[23]. The support gained from the powder bed allows 3DP to take full advantage of SFF's flexibility in creating structures with overhangs, undercuts, and internal volumes without the need for temporary support structures. Further, different materials can be dispensed through separate nozzles, which is a concept analogous to color ink jet printing. Materials can be deposited as particulate matter in a liquid vehicle, as dissolved matter in a liquid carrier, or as molten matter. The proper placement of droplets can be used to control the local composition and to fabricate components with true three dimensional composition gradients. This advantage in compositional control is unique feature of SFF processes that use the deposition of matter to build objects.

Ceramic
Nozzle

Piezoelectric
Transducer

Charging
Cell

Deflection
Cell

Charged
Droplets

Catcher

Uncharged
Droplets
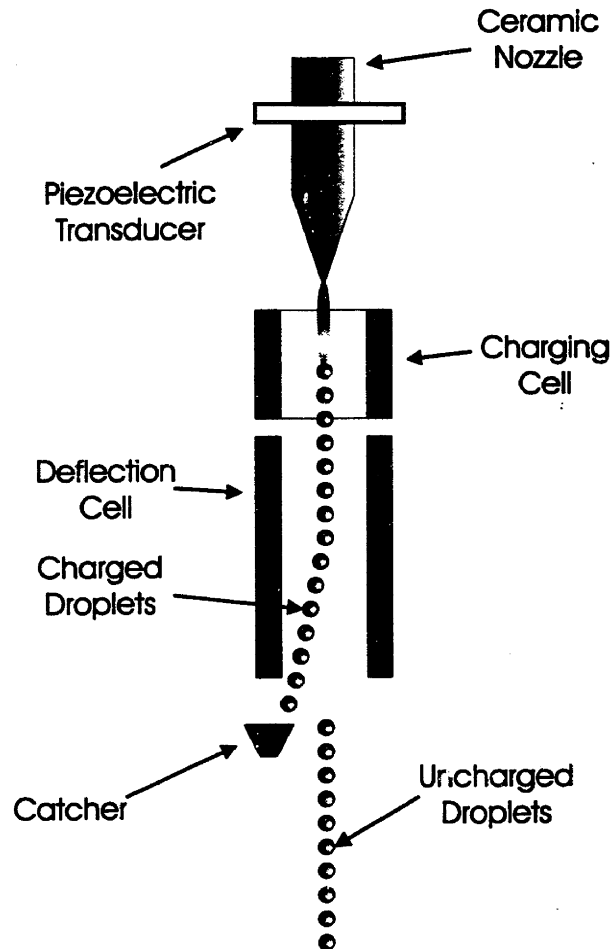
Figure 1.5: Print modulation schematic. Binder stream is broken into droplets and selectively charged. Charged droplets are deflected into a catcher while the uncharged droplets fall through.

Fused Deposition Modeling

Fused deposition modeling (FDM) uses thermoplastic fibers to build three dimensional objects.[24] Figure 1.6 shows a schematic of the FDM process. Starting material in a form of fiber is fed to a heated dispenser. Molten thermoplastic is then extruded through the head. Three dimensional objects are made by controlling the movement of the extrusion head to control the placement of the thermoplastic melt. The process is analogous to placing toothpaste on a tooth brush or placing icing on a cake. It is important to control the extrusion head transitional velocity and the extrusion rate in order to ensure accuracy in the component's dimensions. The rheology of the thermoplastic needs to be tightly controlled since the final part quality is closely linked to the knitting of adjacent beads and the ability to make crisp cuts in the extrudate beads.

Heated Extrusion Head

Formed Object

Fiber Spool

Fixtureless Foundation
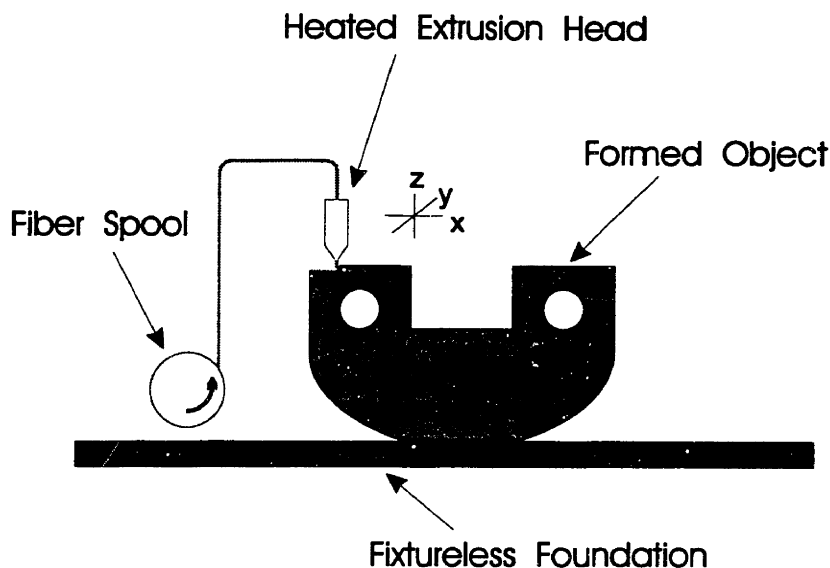
Figure 1.6 : Heated extrusion head is used to shape three dimensional objects in Fused Deposition Modeling (FDM) process.

FDM has recently been used to make ceramic parts by using fiber that is heavily filled with ceramic particles, typically around 60% of the overall volume. Researchers at Rutgers University [25] produced ceramic green bodies in this way and sintered to form fully dense ceramic samples. Binder from FDM-derived ceramic green bodies is removed in a delicate fashion to prevent slumping and distortion. This is a common problem in green bodies with high binder content as in injection molding and tape casting. Binder rheology, setter design, and heat treatment schedule need to be optimized to prevent distortion during binder removal.[26] Binder design for FDM ceramic fibers is slightly more complicated. The viscosity needs to be low enough to accommodate extrusion and merging of beads during the build cycle, yet it should be sufficiently high to avoid slumping during the burnout stage. There has been no attempts to create compositionally graded structures by FDM to date. However, it is conceivable that thermoplastic fibers, pre-loaded with various materials systems, could be used to build such structures.

1.2 THREE DIMENSIONAL PRINTING

1.2.1 COMPUTER-DERIVED MICROSTRUCTURE

3DP is the only SFF technology which has demonstrated deposition of second phase matter onto the base material.[23,27] Dispensing second phase through the nozzle

may be used to cause localized compositional variation in the final 3DP part. Second phase can also be added as dispersions, dissolved matter in liquid vehicle, or molten matter. One can build components with spatially controlled composition (SCC) by precisely monitored deposition of second phase as illustrated in Figure 1.7. Possible benefits of this unprecedented control in green body formation are innumerable. Designers will not only be able to fabricate any macroscopic shape of choice, but can control the microstructure and composition within the object. A single component with several regions of different properties suited for different tasks can be designed with CAD and manufactured by 3DP. Manufacturers can benefit from these "Function Integration" (FI) components by lowered part counts, inventory, cost and weight. Functionally Gradient Materials (FGM) are examples of FI components that can be fabricated by 3DP.[28-30] For example, gradual blending of materials with different coefficient of thermal expansion (CTE) is possible with 3DP. Ceramic coating of metal parts for high temperature applications can be carried out with 3DP. Wear resistant species can be selectively deposited near the wear-prone surfaces. Internal residual stresses can be modified with second phases to strengthen or toughen materials. These are just few of the possible applications of 3DP in SCC. Incorporation of a multiple jet printhead will increase the complexity of possible microstructures by introducing third and fourth phases. Production rates can be also increased by using multiple jet printing. The scale-up potential of 3DP guarantees a smooth transition between prototyping and production of advanced ceramic components.

The ZTA system was chosen as a model system in this work to demonstrate microstructural control capabilities of the 3DP technique. Incorporation of ZrO_2 particles into numerous ceramic matrices can lead to substantial enhancement in mechanical properties, such as toughness and strength, and the ZTA system has been widely studied for structural applications. The relationship between compositional variation and mechanical properties of zirconia-containing ceramics has been studied by many[31-35]. Details of the toughening and strengthening mechanisms are outlined in Chapter 3. 3DP's ability to control microstructure and macroscopic shape simultaneously was used in this study to control mechanical properties of ZTA specimens.

Second Phase Deposited through Nozzle

Matrix Printed with Binder

Powder Cylinder
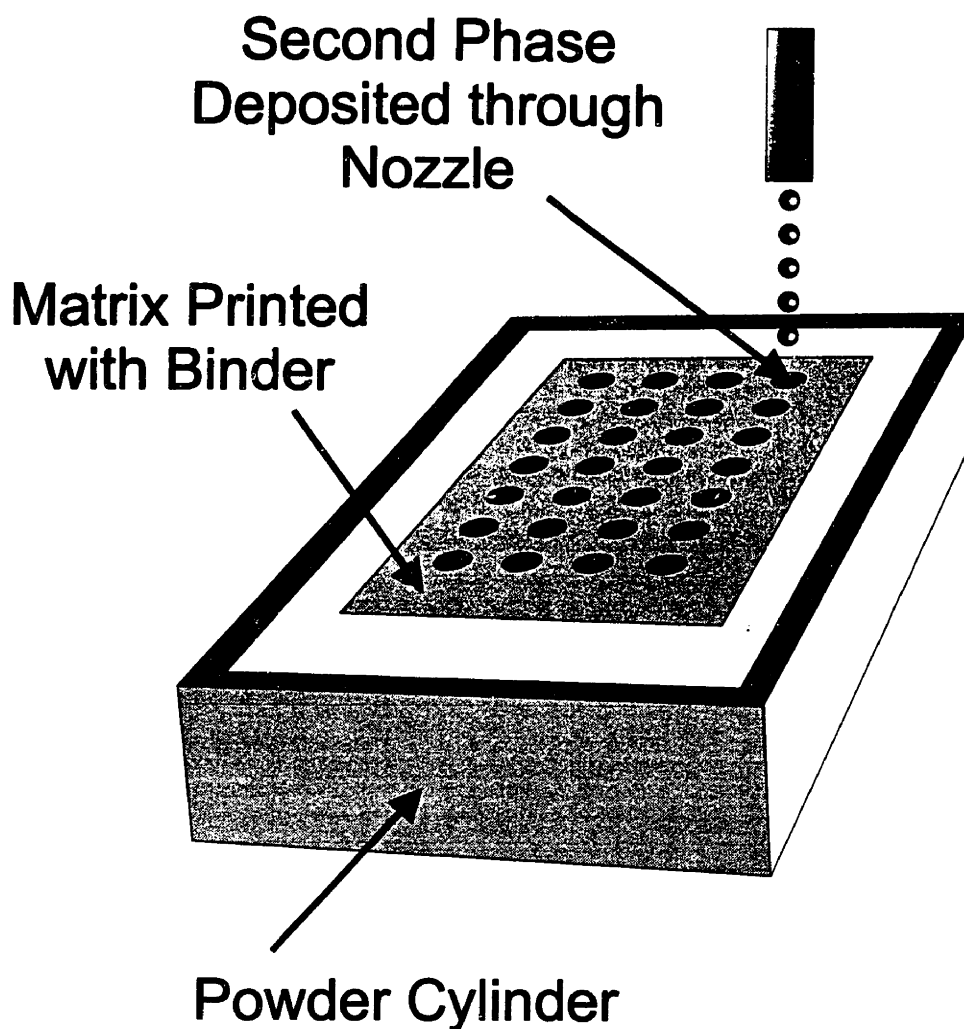
Figure 1.7: Schematic of Spatially Controlled Composition (SCC) by 3DP.

1.2.2 SCOPE OF THE THESIS

Chapter 2 introduces various methods developed to prepare structural ceramic components by 3DP. The baseline process to prepare ZTA samples with computer-derived microstructure was selected as a result on this study. Chapter 2 also discusses the process parameters involved in 3DP and their impact on the microstructural development. Changes in microstructure according to these variables are outlined in the chapter. These parameters were manipulated to fabricate zirconia toughened alumina components and results are reported in the chapters that follow. Chapter 3 discusses the properties of monolithic ZTA specimens prepared by 3DP and how it compares with conventionally prepared ones. Results from ZTA components with Y_2O_3 gradients are discussed in Chapter 4. Examples of both sharp and gradual change in the composition are described

in Chapter 4. Analytical solution developed to predict and design compositional gradients is also introduced in the chapter. Results from the ZTA specimens with surface compression are also reported in Chapter 4. Chapter 5 introduces a case in which mechanical response of the components were prescribed through various computation tools. 3DP was used to construct specimens with tailored mechanical responses. Chapter 5 also discusses different types of applications that 3DP can be used to exploit the computer-derived microstructure.

2. Structural Ceramics through 3DP

2.1 INTRODUCTION

Earlier work has demonstrated the effectiveness of 3DP as a rapid prototyping tool for investment casting [17,18]. Typical 3DP ceramic molds for metal casting are created by printing colloidal silica to bind coarse alumina powder. An example of such a mold is shown in Figure 2.1. 3D-printed molds are then fired at 900°C to cause the glassy phase to form strong bonds between alumina particles. Final density of the ceramic molds for metal casting is typically around 65% of the theoretical density. The alumino-silicate system is not suited for structural applications which usually require full density and superior mechanical properties. Fine ceramic powder, typically in the submicron range, needs to be incorporated to ensure effective densification of the components. Solid state sintering is caused by the reduction in free energy through eliminating solid-vapor interfaces [36]. Therefore, the high surface area in submicron powder provides the driving force for densification. Use of submicron powder is an essential but not sufficient criterion in creating high performance structural ceramic parts. Other requirements, such as high and homogeneous green density have to be met. Bruch has demonstrated that it is important to have high green density in the components to ensure the acceleration and completion of the densification process [37]. Density gradients in green parts, on the other
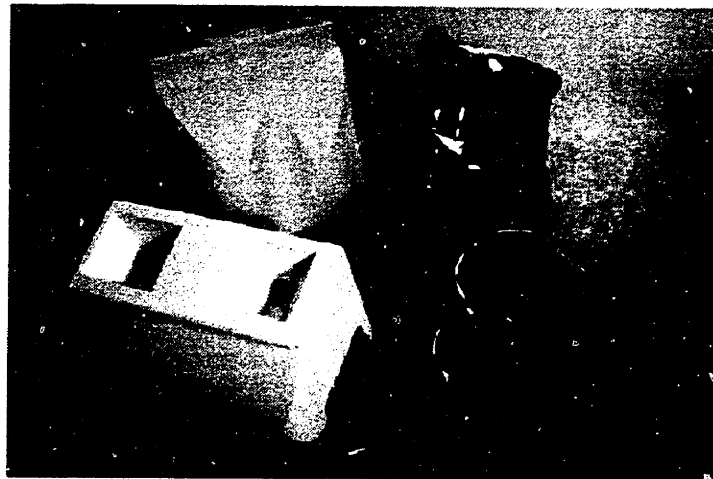
Figure 2.1: 3D-printed alumino-silicate mold and casting for knee replacement.

hand, lead to defect formation and distortion during firing. Lange's study on powder compacts showed the development of crack-like defects due to the differential shrinkage caused by the variation in packing density [38]. These defects have deleterious effects on the strength of the parts since they serve as the crack initiation sites upon loading. Thus, it is important to satisfy all of the above mentioned criteria: fine powder, high and uniform green density, elimination of defects.

Fine powders pose several challenges for direct application in the 3DP process. First, the current generation of 3DP machines spread dry powder across a piston in thin layers. Fine powders do not generally flow well enough to spread into defect-free layers. Their high surface area and the Van der Waal's attractive force between particles cause extensive agglomeration. Cohesive strength of the unpacked powder also increases, and as a result, flowability of fine powders is substantially poorer than large particles. The packing density of submicron alumina powder bed is typically around 28% of the theoretical value[20]. Green density of at least 55% is desired to sinter alumina components to full density at 1600°C. Modifications in the basic 3DP process were necessary to overcome the difficulties in the fabrication of fully dense ceramic parts.

2.1.1 PROCESS DEVELOPMENT STRATEGIES

Several approaches were investigated to create fully dense ceramic components by 3DP. Variations in the powder layer generation techniques and the post printing treatments were explored to find a baseline process for 3DP structural ceramic parts. These various approaches may be categorized by the post-processing requirements.

The *press-rolling technique* and the *spray dried granule technique* were devised for building greenbodies with relatively low initial density [20]. They require an isostatic pressing step to increase the green density prior to sintering. 3D-printed greenbodies are encapsulated in a latex bag under vacuum in both of the techniques, and then submerged in a hydrostatic medium such as oil. Pressurization of the oil chamber results in the isostatic loading on the sample. The green density of an isopressed sample exceeds 55% of the theoretical density which is adequate for pressureless sintering.

A second set of processes involve careful selection of material systems to enable either liquid phase sintering or the infiltration of second phase. Compositions involving substantial amount of glassy phase may be sintered to full density even when the green density is very low. Nammour and Rynerson have fabricated glass components by printing on glass powder and directly firing them [21,39]. Dense ceramic/glass composites were also created by a glass infiltration technique. 3D-printed ceramic bodies were used as a porous preform for glass infiltration. This technique is suitable for applications where very small or no shrinkage is desired. Alumina/glass components prepared by Nammour and Rynerson using this technique showed the final density of 99% while exhibiting total linear shrinkage of 1.5% [21].

A third set of techniques were designed to create dense green bodies directly from 3DP, thereby eliminating post-pressing steps in general. *Press-compaction* and *spray-deposition techniques* were studied for this purpose. Components created by these methods were directly fired to full density. Processing issues related to the implementation of these techniques were investigated by Khanuja [40] and Grau. The obvious advantage of these methods is the elimination of post-printing process steps, such as isostatic pressing or melt infiltration. Spray deposition, for example, uses an atomizer to produce a fine mist of ceramic slurry which is directed toward the powder bed. An intermediate drying step is required prior to printing binder droplets to minimize interaction with the liquid vehicle used for powder spraying. Uncontrolled interactions are undesirable since they may lead to printing defects such as delamination and poor edge definition [41].

2.1.2 PROCESS PARAMETERS AND MICROSTRUCTURE

The microstructure and properties of structural ceramic components are largely dependent on the process parameters. Variations in these parameters can lead to drastic changes in the final microstructure of the components. Close attention has to be paid to optimize the process parameters since the overall performance of the product is controlled by the microstructure. Powder molding processes, for example, involve deformation of powder masses into dies to form complex shapes. The mass typically

includes rather large amounts of organic binder to increase plastic flow into the mold, as is done in powder injection molding [26]. The shear history of each volume element of the component is different because of the complex shape of the mold. This results in non-uniform powder packing in the green part and uncontrolled shrinkage and distortion during sintering. Each volume element of a laminated object is, however, prepared in the same way, regardless of shape or dimension. Properties of 3D-printed components are also very closely related to their build conditions. 3DP dense alumina specimens, for example, exhibited final densities ranging from 88% to 99%, depending on the build parameters.

2.1.3 ORGANIZATION OF THE CHAPTER

Process development and properties of dense alumina components are described in the following sections of this chapter. The press-rolling technique, spray-dried granule method, and spray deposition technique were used to build dense alumina parts. Sections 2.2, 2.3, and 2.4 describe these methods in detail. Particular attention is given to the microstructural variation caused by different process parameters in each of the methods. Advantages and limitations of each method are also discussed in each section. Baseline process for constructing dense ceramic components with compositional variation was selected based on the results from these dense alumina studies. Section 2.5 introduces the printing variables with the greatest impact on microstructure and properties of 3DP structural ceramic parts. Emphasis was given to identifying various ways to control the amount of binder within a greenbody. These conditions were directly implemented to construct dense ceramic components with spatially controlled composition in the later chapters of this thesis.

2.2 PRESS ROLLING APPROACH

2.2.1 EXPERIMENTAL PROCEDURE

Powder Spreading

The powder used for this study was Reynolds RC172-DBM alumina, both undoped and MgO doped, with the mean primary particle size of 0.8μm. The as-received

powder was sieved to collect agglomerates of sizes between 75 and 150 μm. The apparent density and the tap density of the selected agglomerates were measured by using the apparatus and the techniques described by Lee [42].

Lower the platform by one layer spacing plus excess and dispense powder

Spread powder while counter-rotating and vibrating the rod

Level the surface by press rolling the excess while vibrating the rod

Raise the platform by the excess heigh to present a uniform distribution
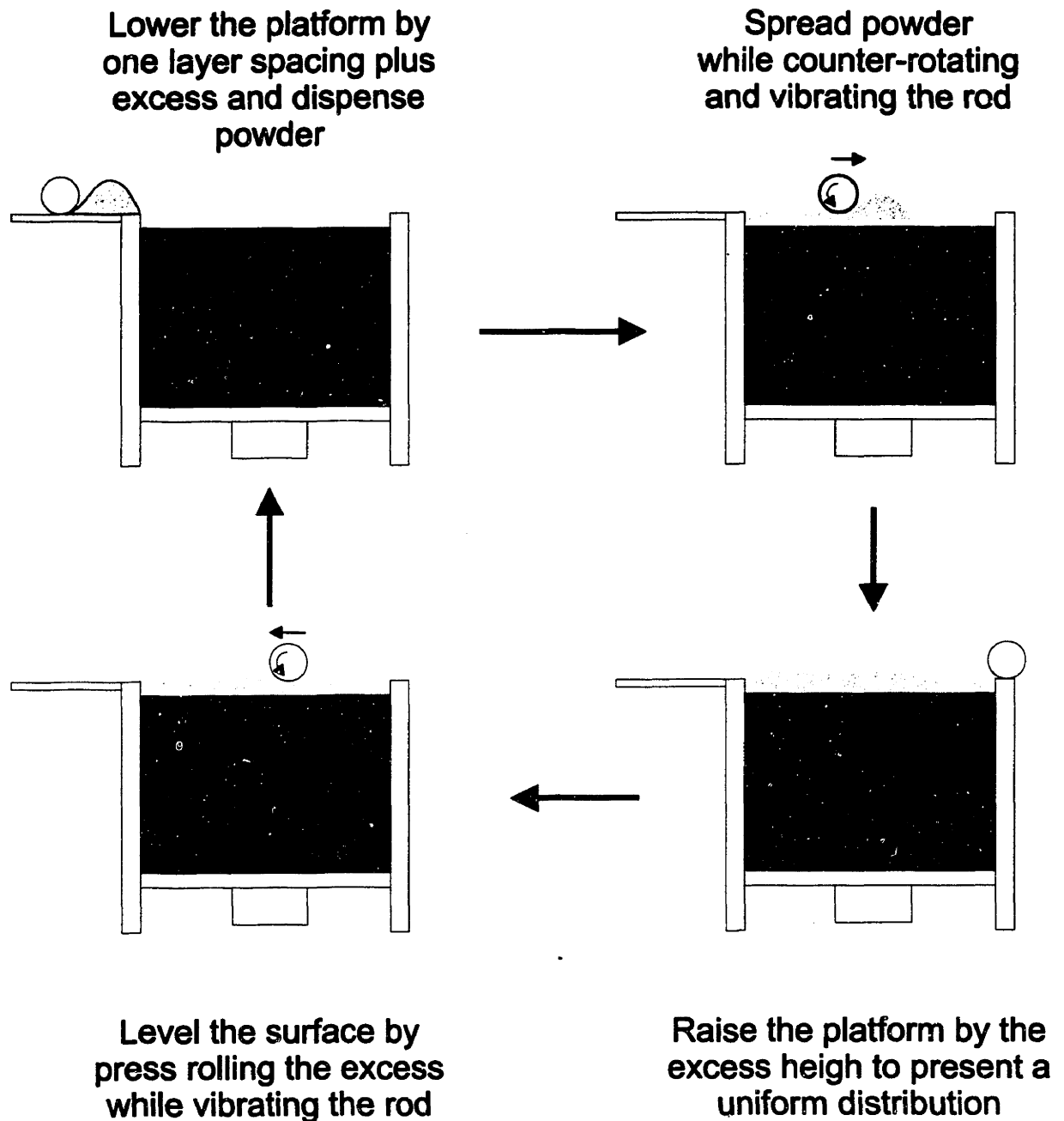
Figure 2.2: Press-rolling sequence for powder layering.

Modifications have been made to the spreading sequence to enhance the packing density and layer quality. Figure 2.2 shows the schematic of the spreading sequence. The piston is lowered in the first step, and a layer of loosely, but fairly uniformly packed agglomerates is produced by traversal of a counter-rotating spreader rod over the piston. The piston is raised on the second pass to expose part of the loosely packed layer. The spreader rod is then forward rotated across the piston to pack the powder rather than shearing away the excess powder. This procedure results in a well packed uniform layer that is ready for printing.

Binder and Printing

The binder used for this study was the Acrysol WS-24 (Rohm and Haas Company, Philadelphia, PA) which is an acrylic copolymer dispersion resin. A continuous jet of Acrysol droplets was made by passing the liquid through a 45μm diameter ceramic nozzle vibrated at 60kHz by piezoelectric transducers. The binder flow rate was 1.25cc/min. The printhead was rastered across the piston with a velocity of 1.65m/sec with 178μm spacing between the lines. The layer thickness was 127μm. Three different concentrations of the binder were used for printing so that the weight fraction of the binder in the final component would be 3, 6, and 12 wt%.

Isostatic Pressing and Sintering

The piston containing the powder bed was removed after the entire build operation and heated at 125°C for one hour to remove water from the bed and cure the binder. The printed parts were then separated from the unprinted region by gently brushing away the matrix powder with a soft brush. The samples were put in a latex bag, evacuated, and sealed before being placed in the chamber of the isostatic press. The pressure used to compact 3D-printed greenbodies was 275 MPa. Samples were either pressed at room temperature (cold isostatic press, CIP) or in heated hydraulic fluid at 80°C (warm isostatic press, WIP). Successfully isopressed samples were then placed in a furnace for binder removal at 450° C and then further fired for densification at 1650° C for 2 hours. The bulk densities of the green, isopressed, and fired samples were measured by using an automated mercury porosimeter (Micromeritics, Norcross, GA).

Mechanical Properties

Four point bending tests were conducted to find the flexural strength of the fabricated material. Precision grinding of the surface of bending specimens was performed prior to testing in order to measure the intrinsic strength of the material and eliminate effects due to surface defects. Grinding was performed by Bomas Machine Specialties Inc. (Sommerville, MA). The size and the shape of the specimens, and the testing procedures were in strict compliance with the ASTM standard C1161-90.

2.2.2 RESULTS AND DISCUSSION

Powder Spreading

The fine alumina powder used for this study has considerably lower apparent and tap density than other common powders used for 3DP, as shown in Figure 2.3. Spreading these agglomerates with the conventional *counter-rolling* sequence as illustrated in Figure 2.4 resulted in layers that are inhomogeneous and had low particle packing density.
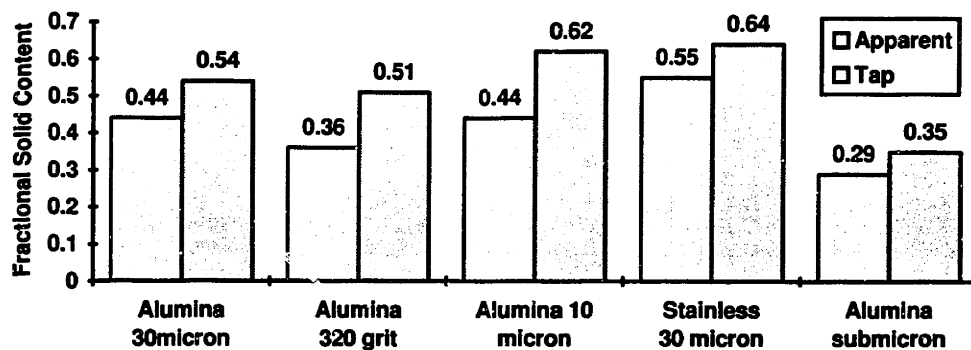
Figure 2.3: Apparent and tap densities of various powders used for 3DP

The *press-rolling* technique has proven to be very effective in creating well packed layers of dry fine powder. The packing density of the resulting powder bed was 40% which is even higher than the tap density of the material. The cohesive strength of the resulting powder bed was quite remarkable and ballistic ejection of particles upon impact of binder droplets was completely eliminated. Ballistic ejection is a common observation for highly flowable powders used in 3DP and must be overcome by

increasing the cohesive strength of the powder bed by different methods such as adding moisture prior to printing [43,44]. The top surface finish was excellent due to the absence of both the ballistic ejection and particle rearrangement caused by capillary force.
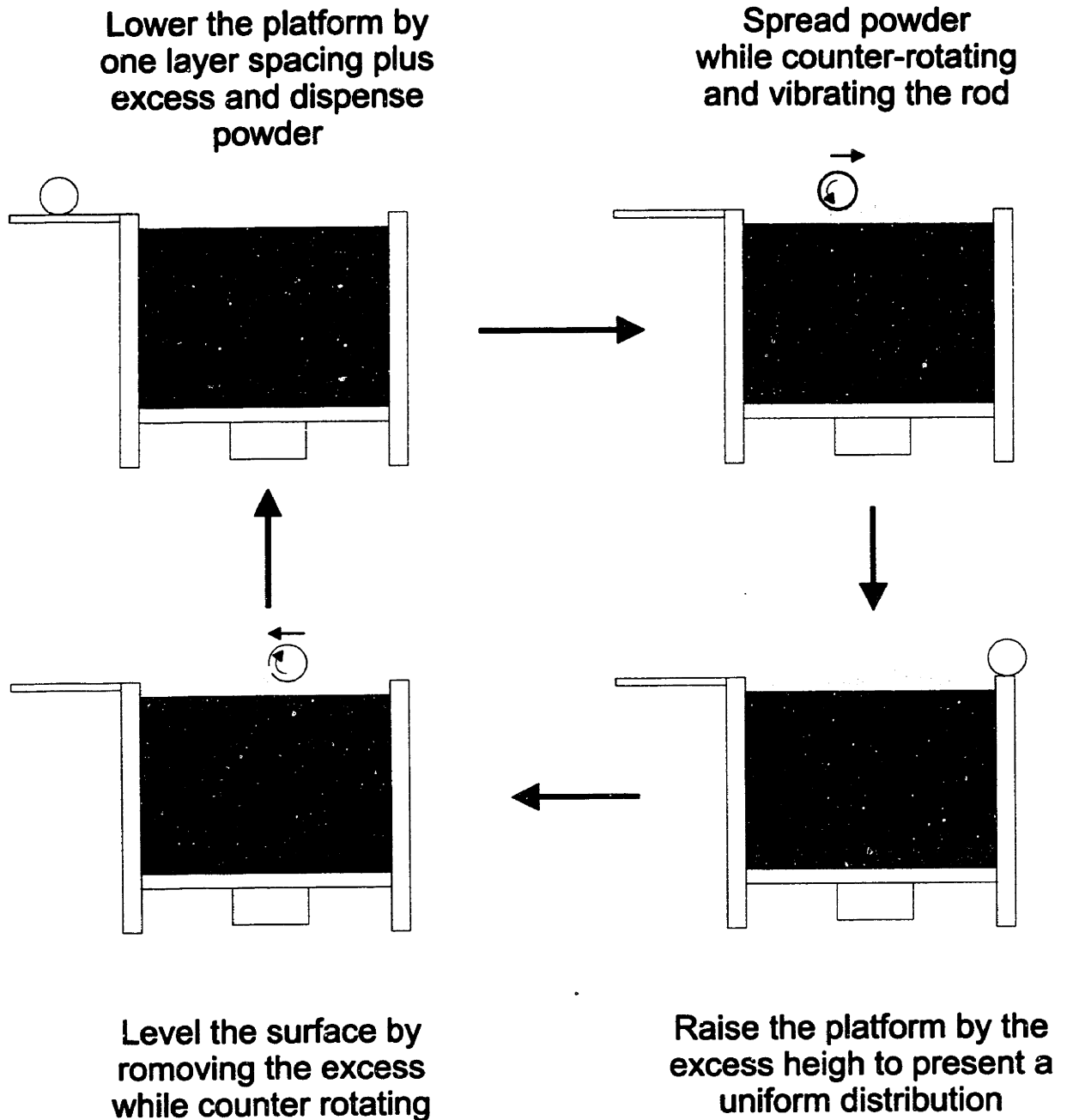
Figure 2.4: Counter-rolling sequence for powder layering. (Lee [42])
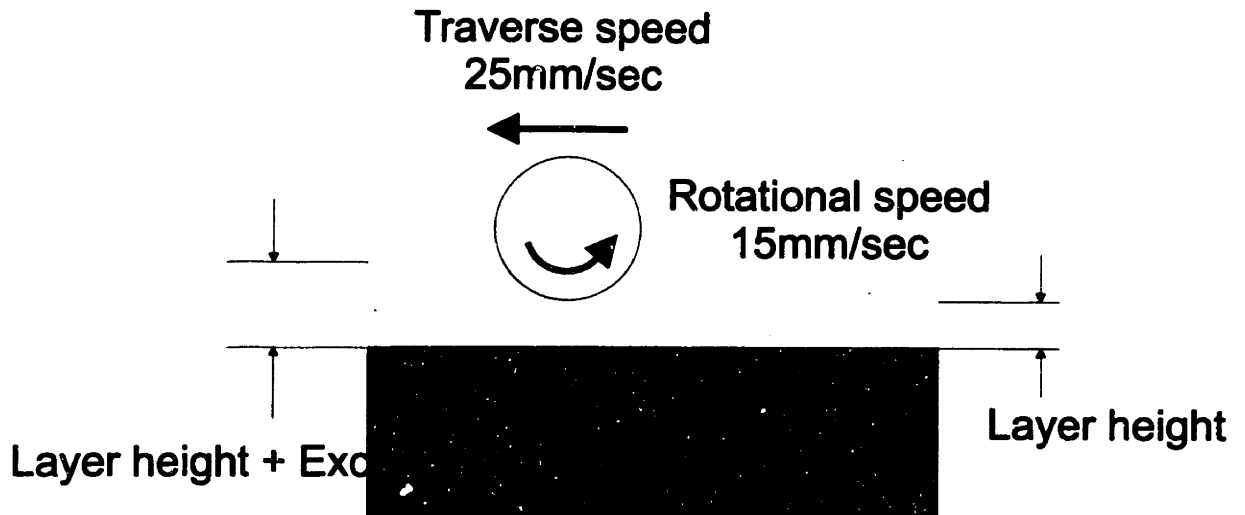
Figure 2.5 Details of the press-rolling parameters.
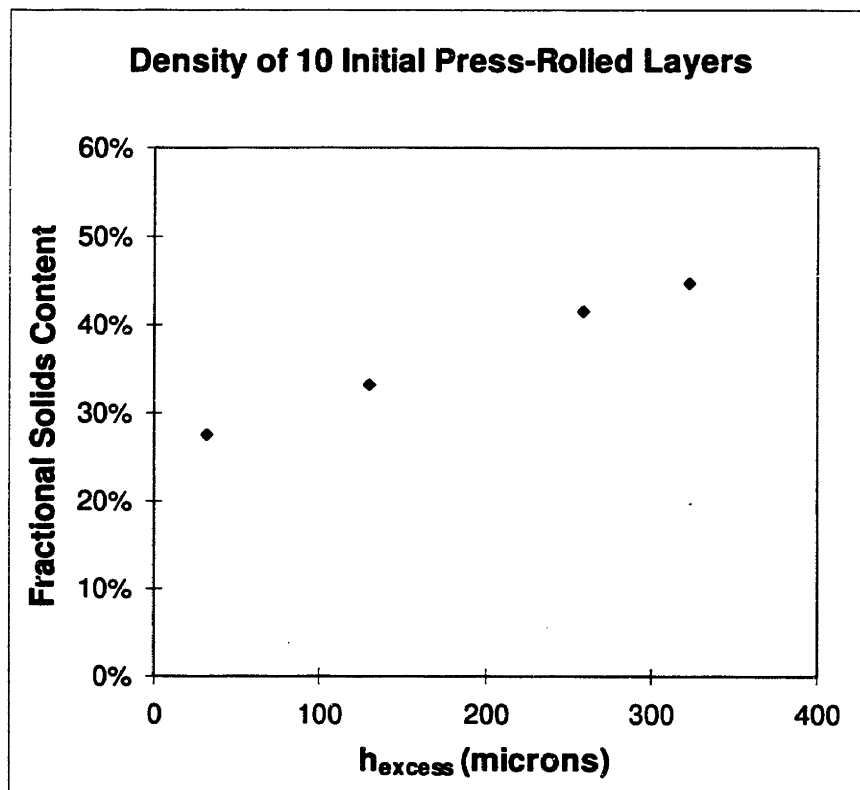
Figure 2.6: Variation in packing density of initial ten layers of press-rolled fine alumina.

Packing density of the press-rolled powder layers is closely related to the layering parameters. The most important factor is the amount of powder exposed to the press-rolling of the spreader rod as illustrated in Figure 2.5. Figure 2.6 shows the powderbed density as a function of excess powder height, h_{excess}. The packing density of initial press-rolled layers increases as the amount of powder being compacted increases.

Figure 2.7: Cross sectional SEM of press-rolled powderbed.

Figure 2.7 shows a polished cross section of the press-rolled alumina powder layers. The alumina agglomerates deform during the press-rolling process and orient themselves at an angle as evident from the micrograph. This phenomenon is the result of the spreading parameters used for press-rolling sequence. The spreader rod traverse speed at the contact with the powder was kept at 25 mm/sec while the rotational speed at the contact with the powder was 15 mm/sec. Figure 2.5 illustrates the movements of the spreader rod and how a net shear force results from these conditions. These aligned agglomerates, or conversely the aligned pores, cause the shear deformation of the green body upon isostatic pressing. Khanuja successfully implemented a bi-directional press-rolling sequence to align the pores in the alternating layers to negate the shear distortion[40]. The micrograph shown in Figure 2.8 shows the complimentary pores in alternating layers.

40
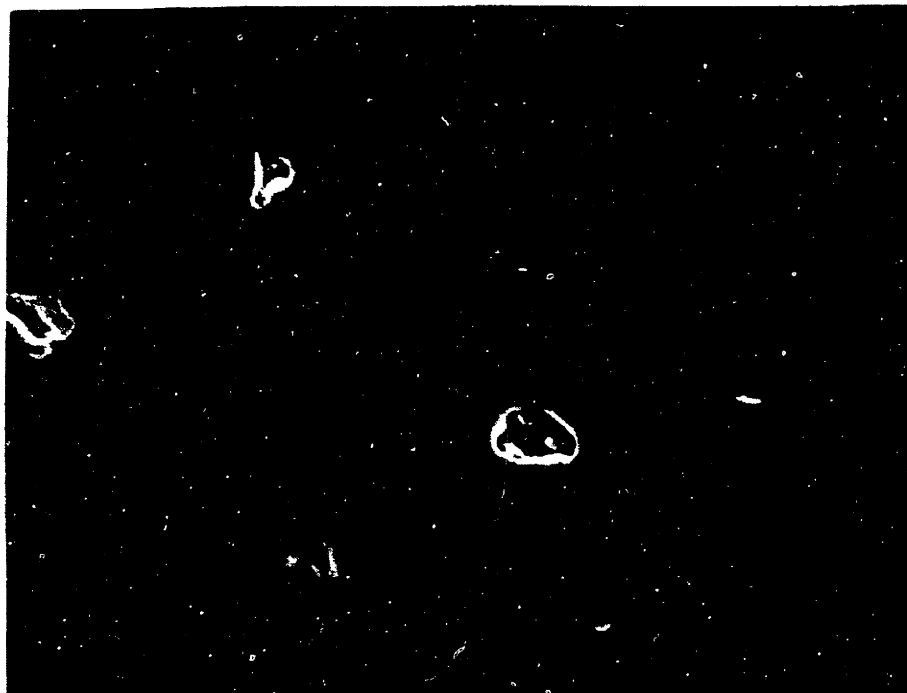
Figure 2.8: SEM micrograph showing the polished cross-section of a green part made by the bi-directional press-rolling process. (Khanuja [40])

Density and Microstructure of Greenbodies

The green density of the as-printed samples was found to range from 33 to 36% of alumina's theoretical density which is too low to fire to full density by sintering. As described earlier, an isostatic pressing of these 3DP green bodies was required to effectively increase the green density. CIP, and WIP at 80°C of the parts were effective in increasing the green density of the samples, as shown in Figure 2.9. Isostatic pressing dramatically increases the final density of the material.

The strength of the green parts varied with the concentration of Acrysol. Samples printed with 3wt% Acrysol were strong enough to hold their shape, but not enough to withstand the handling. Samples with 6wt% binder had adequate strength for both loose powder removal and subsequent handling. Excess polymer from the samples with 12wt% Acrysol was found to segregate at the surface of each layer and is detrimental to the lamination of the layers. Shown in Figure 2.10 is a cross section of a press-rolled alumina specimen which contains 12% Acrysol by the final dry weight. The excess binder

segregates to the top of each layer, as evident from Figure 2.10. Isostatic pressing or sintering do not completely eliminate these types of defects and the final density and microstructure suffer from the adverse effects as will be discussed in the following section. Figure 2.7 is taken from the cross section of a similar component which only contained 6 wt% Acrysol. Excess binder is not observed in second sample.
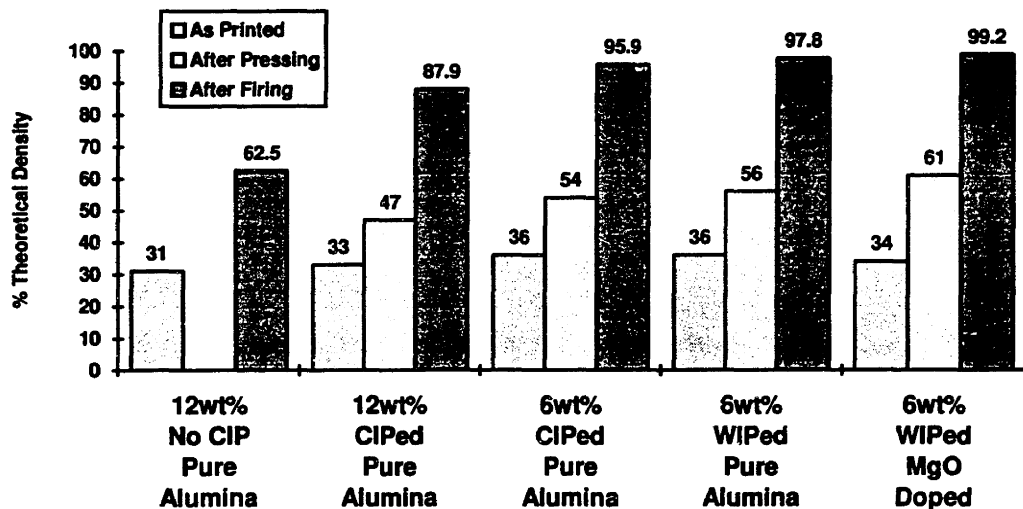
Figure 2.9: Bulk densities of 3DP parts at each stages.
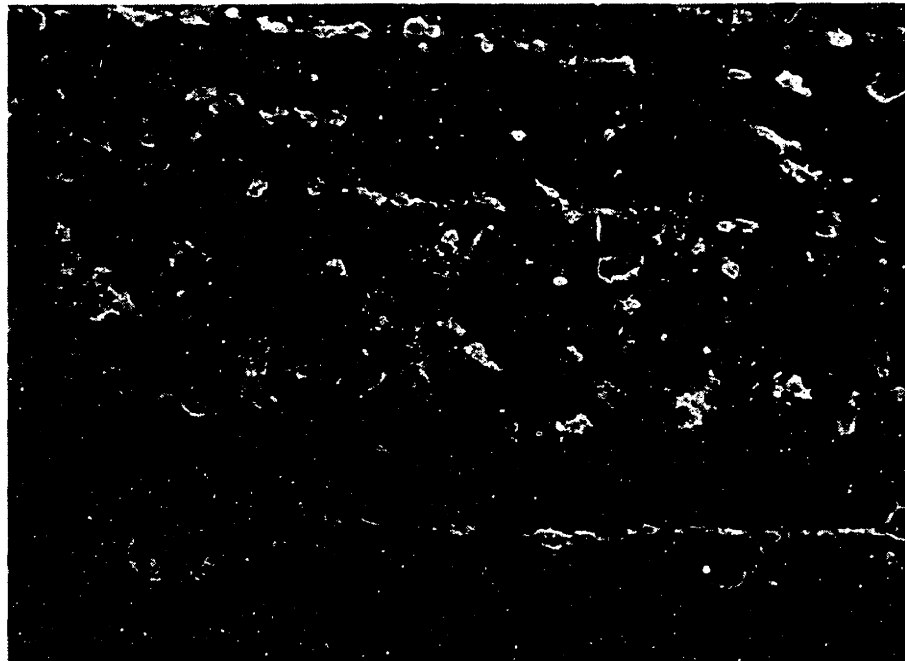
Figure 2.10: Polished cross section of an as-printed press-rolled alumina component with 12wt% Acrysol.
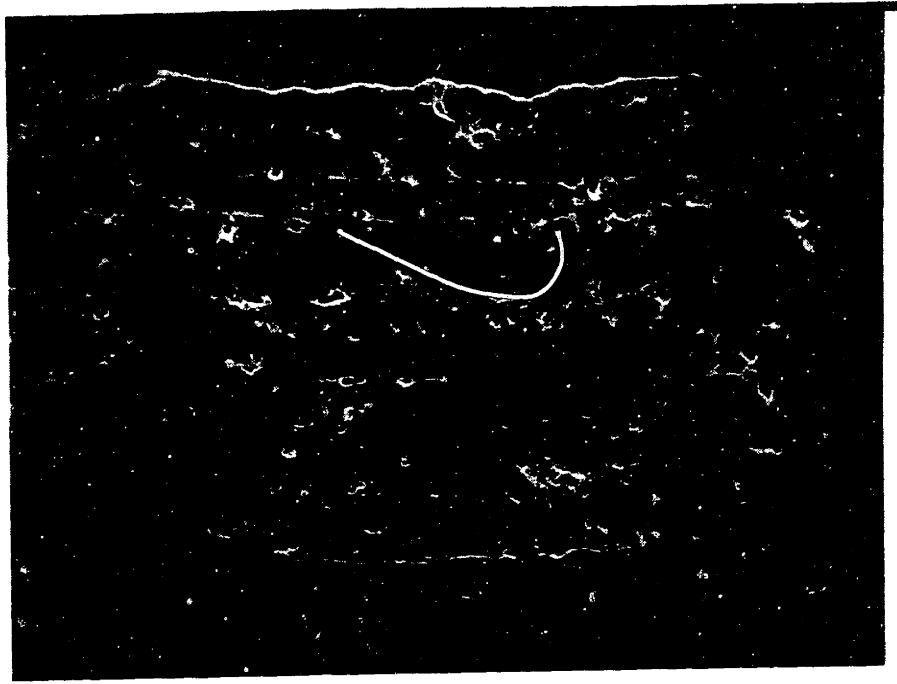
Figure 2.11: Polished cross section of a press-rolled alumina component with 12wt% Acrysol. Specimen was CIPed and fired.
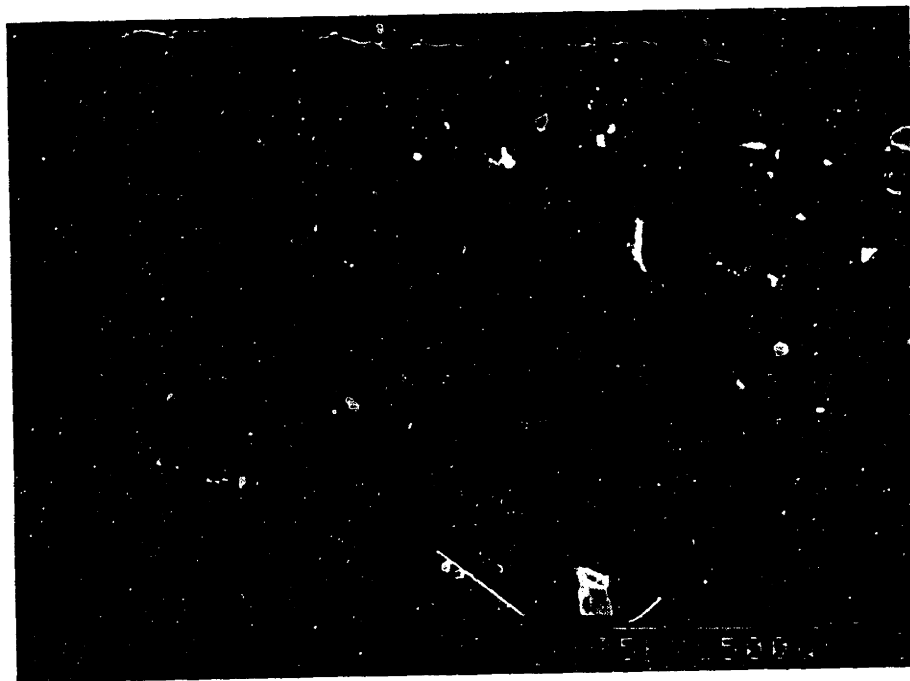
Figure 2.12: Polished cross section of a press-rolled alumina component with 6wt% Acrysol. Specimen was WIPed at 80°C and fired.

Density and Microstructure

The final density depends on the binder content as can be shown by comparing the samples with 12wt% and 6wt% binder in the green state. The fired density of lower binder-content specimens increased to 96% as compared to 88% for the higher binder-content specimen. Excess binder between the laminates contributes porosity that can not be removed by sintering. A polished cross section of the higher binder content sample in Figure 2.11 shows huge cracks between fully dense laminates obviously caused by the presence of excess binder. Density measurements on the samples with same binder content but different isopressing technique also show interesting behavior. Warm isostatic pressing is carried out above the glass transition temperature (46°C) of the Acrysol binder. Thus, the polymer viscosity decreases and causes the greenbody to become more compliant. Green density of the WIPed alumina components are slightly higher than the CIPed specimens as a result. Laminar defects were absent in WIPed specimens since the polymer binder with decreased viscosity redistributes during the pressure-induced densification. The final densities of the subsequently fired parts have shown average value of 99% of the theoretical density of alumina. Figure 2.12 shows the

Figure 2.13: Polished cross section of a press-rolled MgO-doped alumina component with 6wt% Acrysol. Specimen was WIPed at 80°C and fired.

cross section of a sample produced by WIP and sintering at 1650°C. No defects associated with lamination are apparent in the micrograph. The results with the MgO-doped alumina powder have shown the effectiveness of its role as the grain growth inhibitor and resulted in parts with 99.2% density. Figure 2.13 shows the MgO-doped sample fabricated by the identical conditions as the above mentioned undoped samples.

Mechanical Properties

The mean flexural strength of the 3D printed bars upon four point bending was 231.6 MPa and 324 MPa for undoped and MgO doped samples, respectively. MgO normally is added as an alumina grain growth inhibitor. Absence of MgO caused obvious signs of discontinuous grain growth which accounts for the 1.5% residual porosity and the relatively low strength in the case of undoped samples. Fractured surfaces of undoped alumina specimens showed exaggerated grain growth as shown in Figure 2.14. Samples with MgO-doped alumina powders do not exhibit discontinuous grain growth. Fractograph of MgO-doped alumina specimen is shown in Figure 2.15. No obvious signs of structural defects associated with the build process have been found as reflected by the high mechanical strength.

Advantages and Limitations

The powder preparation step for press-rolling technique is relatively simple. The only time consuming step in the fine powder sieving process is the frequent screen cleaning operation. Fine particles tend to adhere to the screen and decrease the effective mesh size. Screens need to be cleaned periodically. Densely packed layers of press-rolled fine particles help eliminate the ballistic ejection upon printing which is commonly observed in other powder systems. Powder removal in complex components, however, becomes complicated due to the highly cohesive nature of the fine particles. This problem is common to most of the methods developed to spread fine ceramic powder in 3DP. One can circumvent this issue by using spray dried granules as will be discussed in section 2.3. High flowability of the spray dried granules dramatically reduces the difficulty in powder removal.
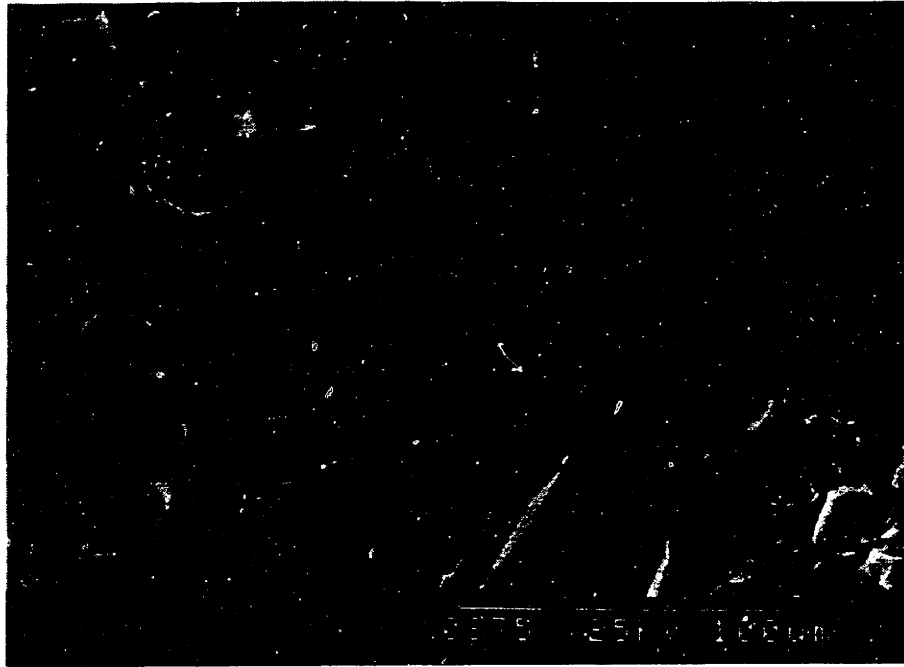
Figure 2.14: Fractured surface of an undoped alumina specimen. Intragranular fracture is evident due to the exaggerated grain growth.
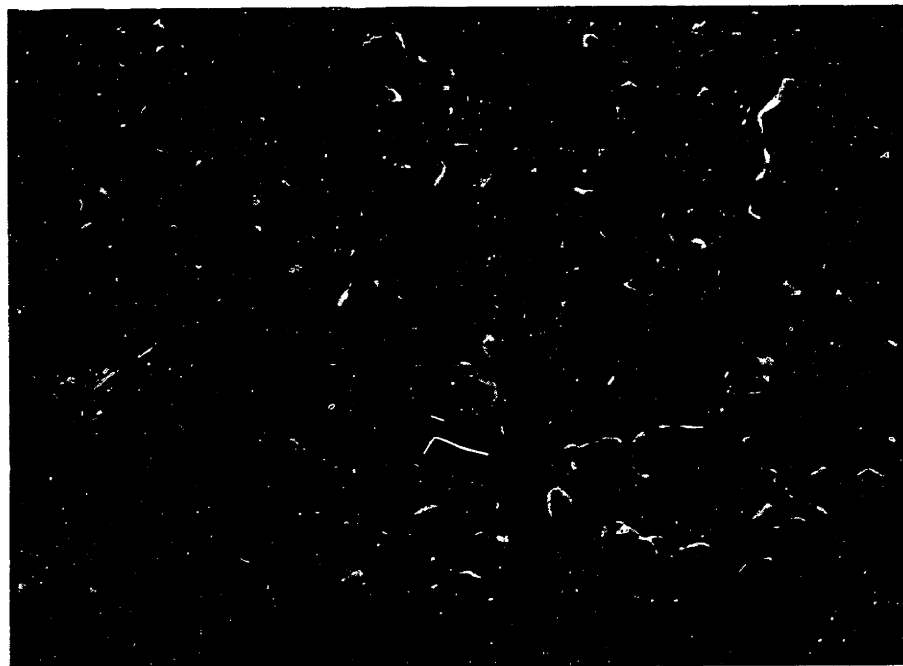
Figure 2.15: Fractured surface of MgO-doped alumina specimen. No exaggerated grain growth is observed and fracture is along intergranular boundaries.

2.3 SPRAY DRIED GRANULES

2.3.1 EXPERIMENTAL PROCEDURE

Spray drying is routinely practiced to prepare highly flowable granules from fine powders in many different industries [45]. Spray dried fine alumina particles were spread to prepare uniformly packed layer for 3DP. Reynolds RC172-DBM alumina powder was used to prepare the spray dried granules. Various organic binders such as Polyethylene glycol (PEG), Polyvinyl alcohol (PVA) and Polyacrylic acid (PAA) were added to the alumina slurry prior to the spray drying process to provide strength to the granules. Although characteristics of the granules depended on the binder system, all of the granules had excellent flowability. Conventional counter-rotation spreading was used to produce uniformly packed layers of spray dried alumina granules. A schematic of counter rotation spreading sequence is shown in Figure 2.4.

The binder system used to print on the spray-dried granules was Acrysol WS-24, identical to that used for press-rolled powder. The amount of polymer in the binder system was adjusted to provide adequate green strength for post-printing handling of the parts. The printing conditions were kept identical to the press-rolled samples with an exception of the layer thickness. Each layer of spray-dried granules was 178μm in thickness.

Isostatic pressing was required in these parts to increase the green density as was necessary for press-rolled parts. Isostatic pressing of complex shapes is a challenging process issue for 3DP. Conventional latex bagging techniques can only be used for limited range of shapes. Several different techniques were developed to encapsulate the complex shapes for isostatic pressing. The concept of filling up the latex bag with a temporary filler material to enclose the cavities and surrounding 3D-printed components was tested. Several different powders were evaluated for isopressing filler material, such as 30 μm alumina platelets, 10 μm spherical alumina, spray-dried alumina granules with various polymeric binder and low molecular weight Polyethylene glycol (PEG) powder.

Binder removal and sintering conditions for 3DP components from spray dried granules were kept identical to that of components built by press-rolling method. Isopressed samples were fired at 450°C for binder removal and 1650°C for 2 hours for sintering.

Four point bending tests were also conducted on sintered specimens. Samples were ground to the standard size and tested according to the ASTM specifications.

2.3.2 RESULTS AND DISCUSSION

Powder Spreading and Green Density

Typical packing density of the powderbed was between 30 and 35% of the theoretical density. Bulk density of the spray dried granules were found to be 50% of the theoretical value. This suggests that the physical packing density of the granules are in the range of 60 to 70%. Powder layers produced by spreading spray-dried granules also exhibited highly uniform packing. Figure 2.16 shows a polished cross section of SD powderbed embedded in epoxy. Unlike the press-rolled powder layers, the packing density of SD granules does not vary significantly with spreading parameters.

The binder-powder interaction in SD granule-derived layers lead to localized decrease in the packing density as evident from Figure 2.16. This is undesirable since some of the inhomogeneities introduced by the printing defects cannot be completely eliminated by the isostatic pressing process. Giritlioglu has observed these inter-granular defects on the fractured surfaces of 3DP alumina and they are believed to be the fracture origins [46]. It is, therefore, important to have not only an uniform packing density, but also to have high enough cohesive strength so that will not be easily distributed by the interactions with binder droplets.

Powder removal from completed components were quite simple since the granules from the unprinted regions can be shaken off easily. This is in sharp contrast to the parts built by the press-rolling method, where even the unprinted portions of the powderbed have substantial green strength. Repeated soft brushing was required to remove loose powder from the press-rolled powderbed.

Unprinted region   Printed region
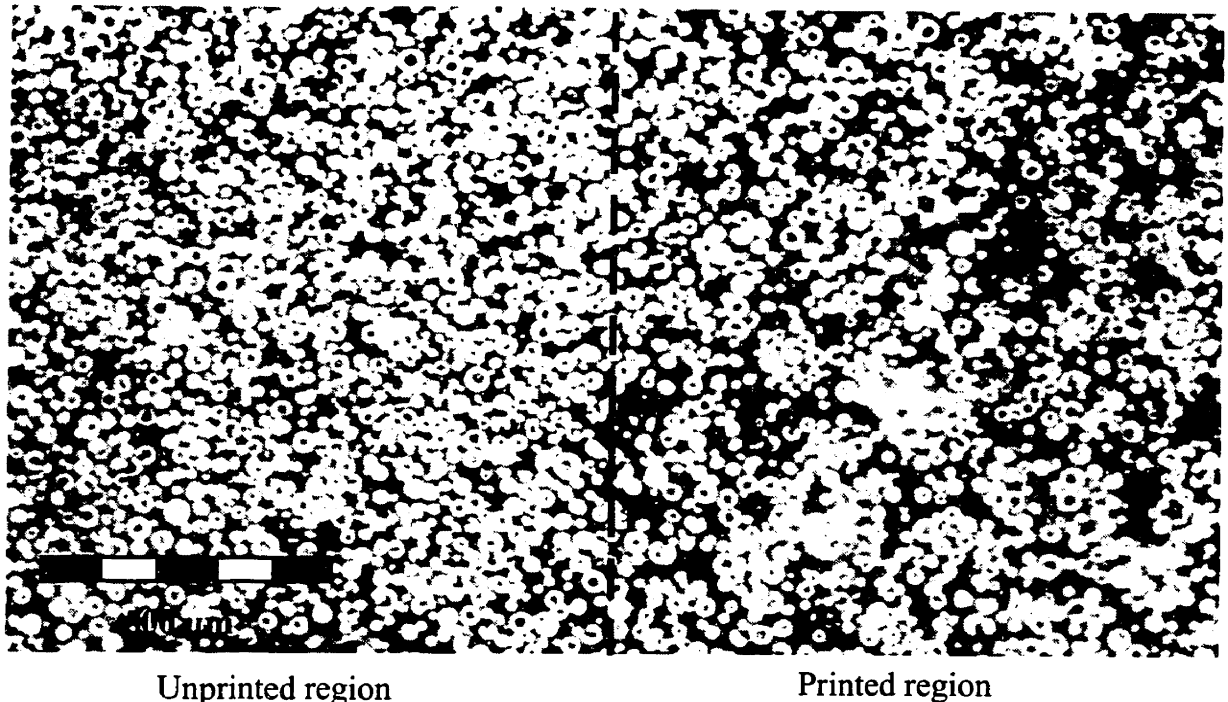
Figure 2.16:   Decrease in the packing density of spray-dried granules as a result of binder-powder interaction. Left portion of the micrograph shows the unprinted region while the other half shows lower packing due to rearrangement of granules.

Isostatic Pressing of Complex Parts

The concept of filling up the latex bag with a temporary filler material to enclose the cavities and surrounding 3D-printed components has proven effective. The ideal material system for the task has proven to be the low molecular weight Polyethylene glycol (PEG) powder [46]. Figure 2.17 illustrates each of the steps involved in the PEG encapsulation technique. In this technique, the latex bag is filled with PEG powder and then the complex shape is placed in the bag. More PEG powder is added to completely encapsulate the component before the bag is evacuated and sealed. The PEG powder acts as a semi-fluidic buffer upon pressurization to 275 MPa, and the pressure is transferred to the greenbody through the PEG compact. The complex shape is embedded in a fully dense PEG shell when the isopressing is completed. PEG is then dissolved in water to reveal the densified green body ready for firing.
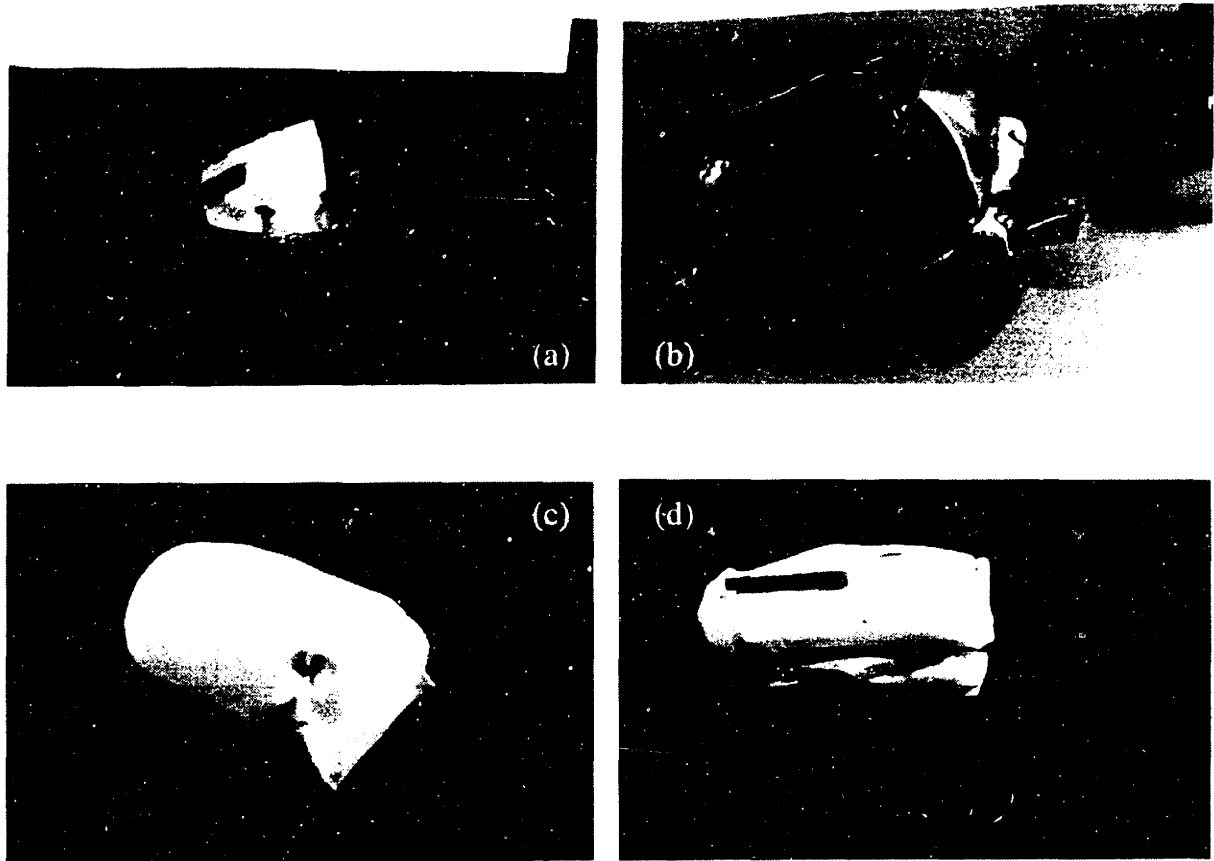
Figure 2.17: PEG encapsulation technique used to isostatically press complex shapes. (a) Component is embedded in PEG powder. (b) The isopressing bag is evacuated and sealed. (c) After pressing, the specimen is encapsulated in PEG. (d) PEG is dissolved in water to reveal compacted specimen. (Giritlioglu [47])

Warping

The interaction between binder droplets and spray dried granules caused the parts to deform during printing. Spray dried granules experience an extensive ballistic ejection when the droplets land on the powder layer. Binder droplets are then redistributed within and between the granules to form structural building blocks known as primitives. Lauder has found that the size of primitives depend on the size and shape if the starting powder[48]. It is the knitting of these primitives that allow the formation of 3D-shapes in 3DP. Spray dried granules pose an unique challenge in this process due to the presence of fine pores. Liquid from the binder droplets undergo a redistribution driven by the capillary suction from both the intra- and inter-granular pores present in the powderbed. Significant amount of shrinkage occurs in the parts even before the printing cycle is completed for the layer. This problem is accentuated when another layer is built on top of the already shrunken layer of material. The newly printed layer attaches to the previous layer and begins to shrink. The resulting stress on the top layer causes the two layer structure to warp out of the powderbed surface. This is analogous to the thermal stress mismatch in bimetallic strips. Layer upon layer, the shrinkage is compounded and the warpage becomes amplified. This warpage stops eventually when the thickness of the previously printed layers increase, thereby providing enough stiffness to overcome the drying stress from the top layer [40].

Many factors influence the extent of warpage, such as pore distribution in the powderbed (both inter- and intra-granular), the polymer content of the binder system, print style, and drying conditions. Combinations of the above process parameters were identified to eliminate the warping phenomenon in spray dried granule derived 3DP parts. Warpage-free alumina components, for example, were built by using spray dried granules that had been fired to remove the polymer binder prior to printing. This increases the pore volume within the granules and effectively reduces the amount of binder in the intergranular pores. The polymer content in the binder system is also adjusted so that only minimal amount of polymer bridge is present between granules. Another approach is the addition of plasticizer in the binder system to reduce the drying

stress [40]. These factors are, however, chosen carefully so that the overall strength of the printed components is not significantly reduced.

Microstructure and Properties

The density of the isopressed and fired spray dried alumina components were 99% of theoretical density or higher. No noticeable distortion was observed during isopressing and sintering of these components. This is in sharp contrast to the press-rolled components. This can be attributed to the uniformity in the powder packing. Cross sectional SEM of these components showed no signs of laminar defects as illustrated in Figure 2.18. Average flexural strength of these components was 400 MPa which is comparable to conventionally prepared alumina components.
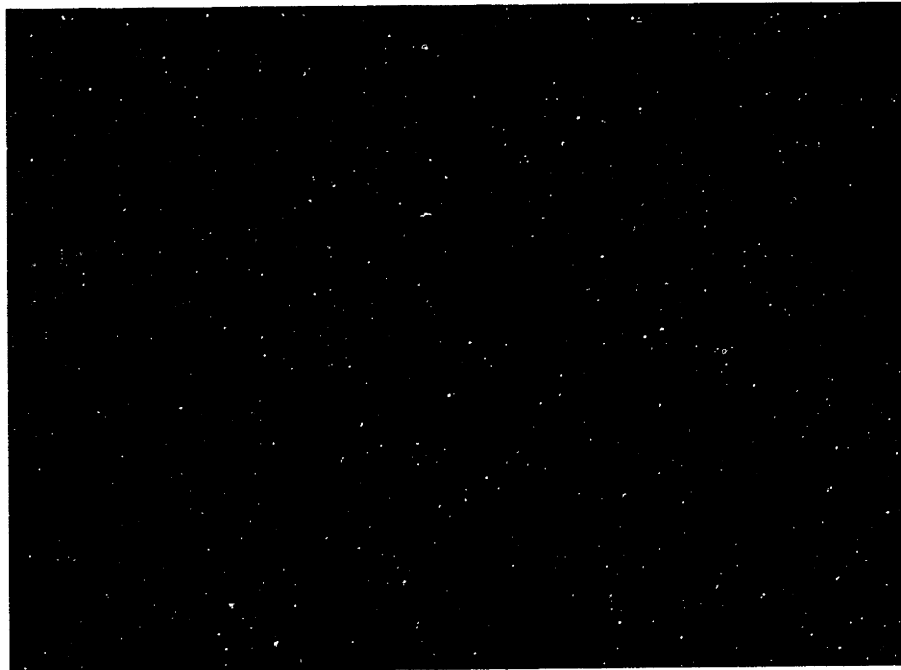
Figure 2.18: Polished cross section of a WIPed and fired alumina component constructed by using spray dried granules.

Advantages and Limitations

The ease of powder removal and elimination of distortion in the 3DP components out of spray dried granules are significant improvement over the press-rolling method. Various complex shapes have been fabricated by using this method. One of the most challenging issues facing this method is the optimization of the process variables to eliminate warping of parts during printing cycles.

While the isostatic pressing step is an effective and reliable way of increasing green densities and eliminating large pores, it adds time and complexity to the overall process. It is indeed desirable to produce components with high initial density, thus eradicating the need for intermediate step in the process. Press-compaction and spray deposition techniques have been investigated by Khanuja to prepare dense powder layers for 3DP [40].

2.4 SPRAY DEPOSITION

Lange has pointed out that many of the strength limiting flaws in structural ceramic components can be eliminated by using colloidal processing in green forming[49]. The uniformity of green bodies prepared by wet processing is typically superior to the ones fabricated by dry powder processes such as die pressing. The spray deposition technique has been proposed to take advantage of this wet powder handling to spray down uniform and high density powder layers for printing.

2.4.1 PRELIMINARY RESULTS

Powder Deposition

Khanuja has demonstrated the concept by using a commercial paint brush head to spray alumina slurry on porous substrates to produce powder layers [40]. The thickness of each sprayed layer was chosen carefully to avoid cracking in the layer driven by the biaxial drying stress. Dense powder layers were prepared by this method with 50% or higher packing density.

Spray deposition method addresses both high and uniform green density requirements. Moreover, the quality of layers can be tailored by manipulating the spray parameters. The quality of the spray deposited alumina layers, for example, depends on factors such as the stability and drying characteristics of the slurry. Spray parameters can be adjusted to achieve an optimum in powder layer characteristics. The working distance, raster speed of spray head, and distance between each spray pass are just few examples of those spray parameters. Figure 2.19 is a polished cross section of a spray deposited alumina powderbed. The specimen had been fired directly without any intermediate step

to increase the density. No apparent lamination defects are evident from the micrograph. Khanuja reported that the packing density of the green cake was more than 50% of the theoretical density [40].
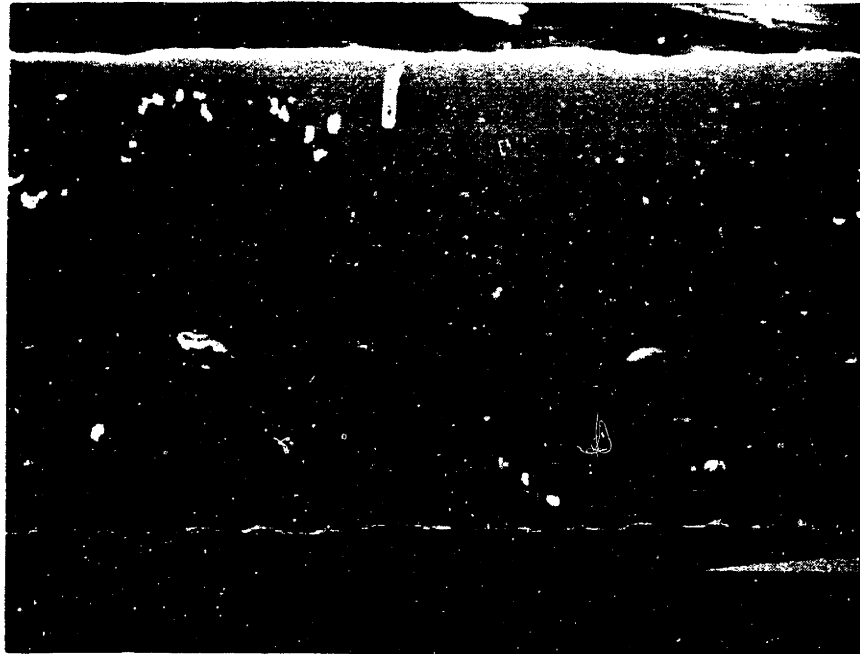
Figure 2.19:   Polished cross section of spray deposited alumina powderbed. The specimen was fired at 1650°C for 2 hours. (Khanuja [40])

Powder-Binder Interaction

A binder material system was chosen carefully to meet complex requirements. One of the most important criteria is the interaction with the powder surface to form a strong bond. This is especially crucial in the spray deposition method since the completed part is embedded in well packed powder cake that must be removed without affecting the printed portion. Khanuja developed an aqueous part retrieval method where the unprinted region redisperses in aqueous bath while the printed region is unaffected by the liquid [40]. This was possible because the binder molecules chemisorbed onto the powder surface. Alumina components prepared by this process have been directly fired to full density. Systematic studies by Grau and Caradonna are in progress to fine tune the powder spray process [50].

The binder-powder interaction in the spray deposited powder layers differ significantly from the spray-dried granule system. No ballistic ejection of powder was observed in the layers generated by the spray deposition method due to the high cohesive strength from the dense packing. The binder droplets land on the powder surface and then infiltrate into the fine pores. The permeability of the powderbed, wetting characteristics and the viscosity of the binder solution determine the kinetics of the binder infiltration process. Controlling the binder kinetics is crucial to avoid printing defects. Arthur observed the splashing of binder droplets on the surface of spray deposited powder layers[41]. This is a consequence of the significant time required for binder droplets to wet into powderbed. A transient pool of binder forms on the top of the powderbed and splashing occurs when the trailing droplets hit the liquid at high velocity. Khanuja also reported that uncontrolled excess binder on the surface of layers have introduced laminar defects in the spray deposited 3DP components as shown in Figure 2.20 [40].
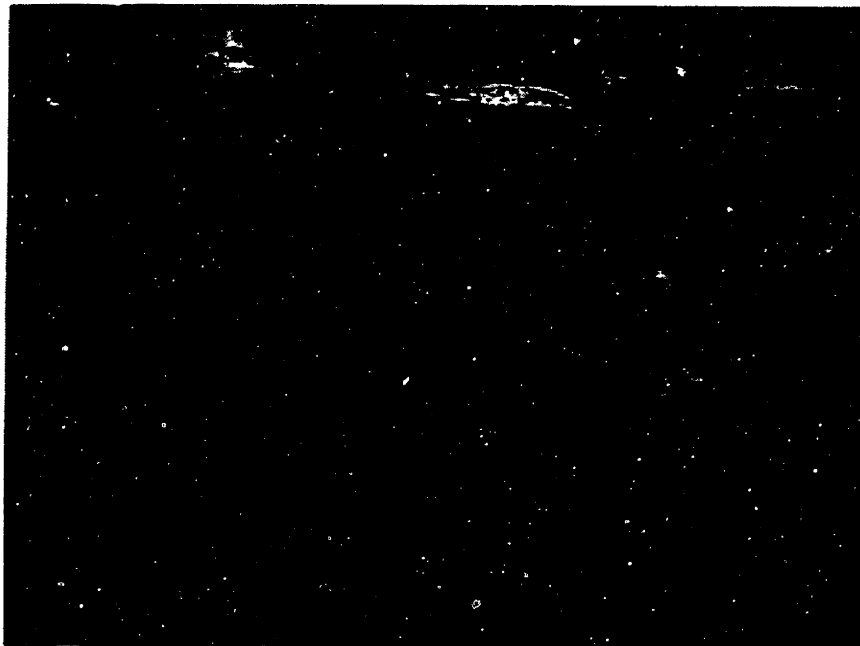
Figure 2.20: Polished cross section of spray deposited alumina specimen. Excess binder between layers led to delamination and cracking during firing (Khanuja [40]).

Advantages and Limitations

The final microstructure of 3DP structural ceramic components are largely dependent on the powder spreading method, as described above. The spray deposition method is capable of creating high density uniform powderbed for printing. This is a significant advantage over the previous two methods because spray deposition technique can completely eliminate the isostatic pressing step. Uniform microstructure also ensures the elimination of distortion and strength-limiting defects in the final component.

The required characteristics for the binder, however, is much more complex than that of press-rolling or spray-dried granule methods. Wetting characteristics, chemical interaction with the powder surface must be tailored to meet the complex criteria in addition to the conventional requirements, such as jettability, and conductivity.

The thickness of each spray-deposited ceramic powder layer was 60μm, roughly one third of that for spray-dried granules. This can increase the resolution of the final component and minimize the "stair-steps" from the side surfaces of 3D-printed components. Another implication of the decreased layer thickness is the increase in build time. Decreasing the layer thickness by a factor of three does not, however, require one to increase the number of layers to be printed by a same factor. This is because the packing density of spray-deposited layers is nearly twice that of spray-dried granule method. Volume of the as printed greenbody from spray deposit method need to be only half that of spray-dried granule method to achieve same fired dimensions.

2.5 CONTROL OF BINDER AMOUNT

2.5.1 INTRODUCTION

Precise control of binder amount is required for fabricating specimens with compositional variation. The local composition of second phase is controlled by the fraction of the matter being deposited in the liquid vehicle, and the total deposition amount. One of the simplest ways to vary the composition within a component is to use several nozzles to print solutions of various concentrations. This approach is, however, not widely used for the same reason it is not necessary to print eight different inks to

print eight shades of gray with an ink jet printer. Instead, the printing parameters are used to achieve localized variations in composition. The following sections list and discuss each of these printing parameters in greater detail.

2.5.2 PRINTING PARAMETERS

The volume fraction of second phase matter that can be deposited through the nozzle depends on several printing parameters. Figure 2.21 shows a schematic of a printed single line and the printing parameters. The final volume of the line can be expressed as the following,

$$V_{line} = h_{layer} \times d_{line} \times l_{line} \times f_{packing} \qquad (2.1)$$

assuming the printed line goes to full density upon sintering, and the deposited second phase does not contribute any additional volume in the final components, (as is the case for organic binder and dopants) In the above equation, h_{layer} is the layer height, d_{line} is the spacing between each raster line, l_{line} is the length of the line segment, and $f_{packing}$ denotes the fractional packing density of the powderbed. The volume of second phase deposited can be calculated by using the following equation.

$$V_{2nd\_phase} = \frac{f_{droplets\_printed} \times Q \times l_{line} \times c}{V_{printhead}} \qquad (2.2)$$

$f_{droplets\_printed}$ represents the actual fraction of binder droplets that bypassed the catcher and landed on the powderbed. This concept is illustrated in Figure 2.22. The volumetric flow rate is denoted as Q while c represents concentration of the second phase within the fluid system. Finally, $V_{printhead}$, is the raster speed of the printhead. The volume fraction of the second phase material relative to the starting powder matrix is given by

$$f_{2nd\_phase} = \frac{V_{2nd\_phase}}{V_{line} + V_{2nd\_phase}} \qquad (2.3)$$

The above can be approximated as $\dfrac{V_{2nd\_phase}}{V_{line}}$ when the amount of second phase is small,

and by substituting the above equation, becomes

$$f_{2nd\_phase} = \frac{f_{droplets\_printed} \times Q \times l_{line} \times c}{V_{printhead} \times h_{layer} \times d_{line} \times l_{line} \times f_{packing}} \tag{2.4}$$

Each of the variables in the above equation can be manipulated to adjust the amount of matter deposition in 3DP specimens. Figure 2.23 and Figure 2.24, for example, illustrates the effects of variation in $V_{printhead}$ and d_{line}.

Practical limitations are attached to each of the above printing parameters. Continuous binder jet becomes unstable, for example, when the flow rate decreases much below 0.8 cc/min. Ballistic ejection is directly related to the binder jet speed and it is also undesirable to increase the flow rate of the binder much above 1.3 cc/min. The lower limit on printhead speed is also established by the ballistic ejection and loss of resolution while the upper limit is established by the physical capabilities of the printhead to accelerate. The placement of binder droplets should also be designed to preserve uniform binder distribution. One cannot rely on a large line spacing alone, for example, to achieve a uniform and low binder content. This may lead to stitching problems between each printed line. The lower limit on binder concentration is established by the resulting poor green strength in the final part. The upper limit is established by the ability to print highly concentrated suspensions. Combination of these parameters have to be chosen carefully to ensure high quality of 3DP components.

$V_{printhead}$

h_{layer}

l_{line}

d_{line}

Flow rate, Q

Adjusted flow rate,
$f_{droplets\_printed} \cdot Q$
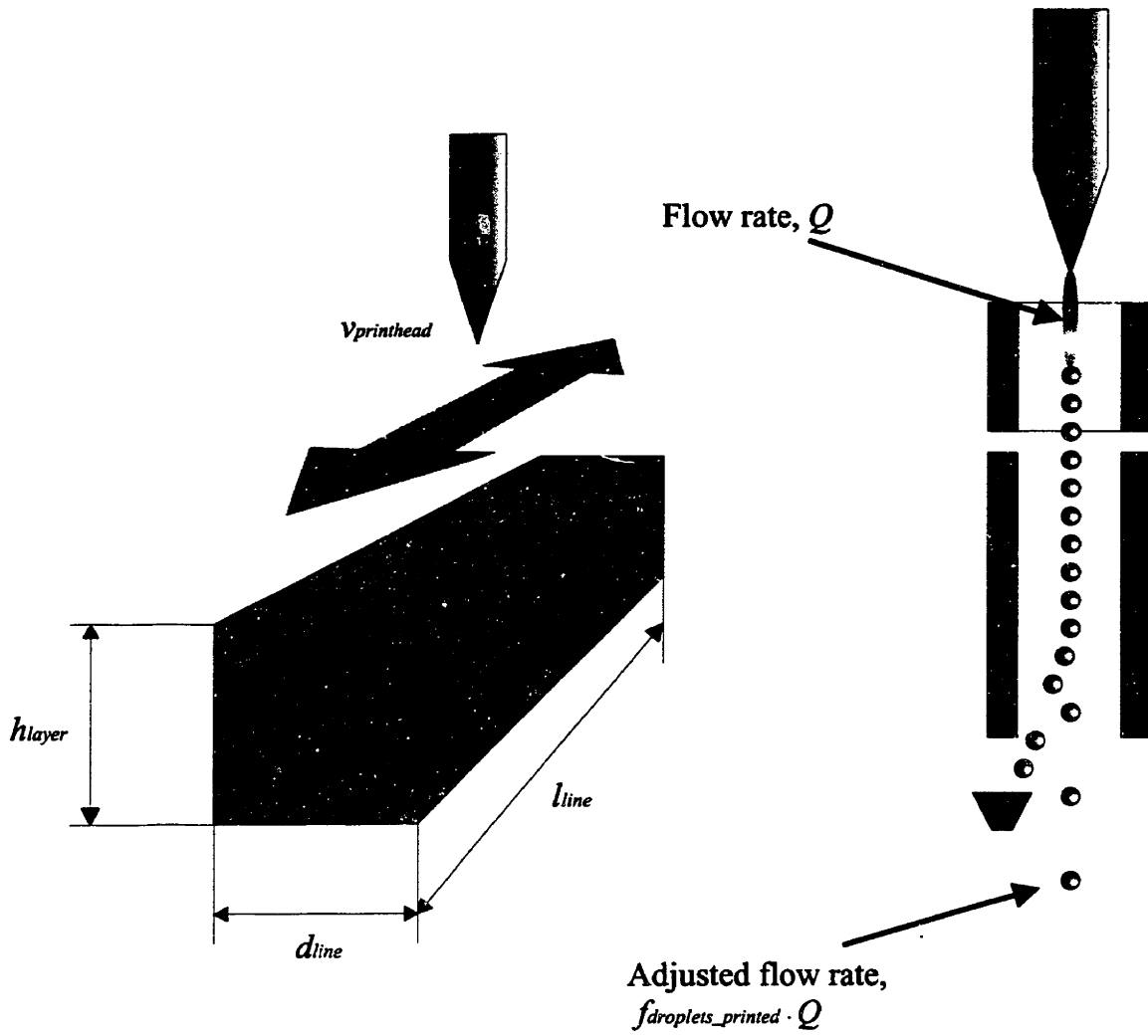
Figure 2.21: Schematic of printing parameters.

Regular Printing   Printing Every 3rd drop
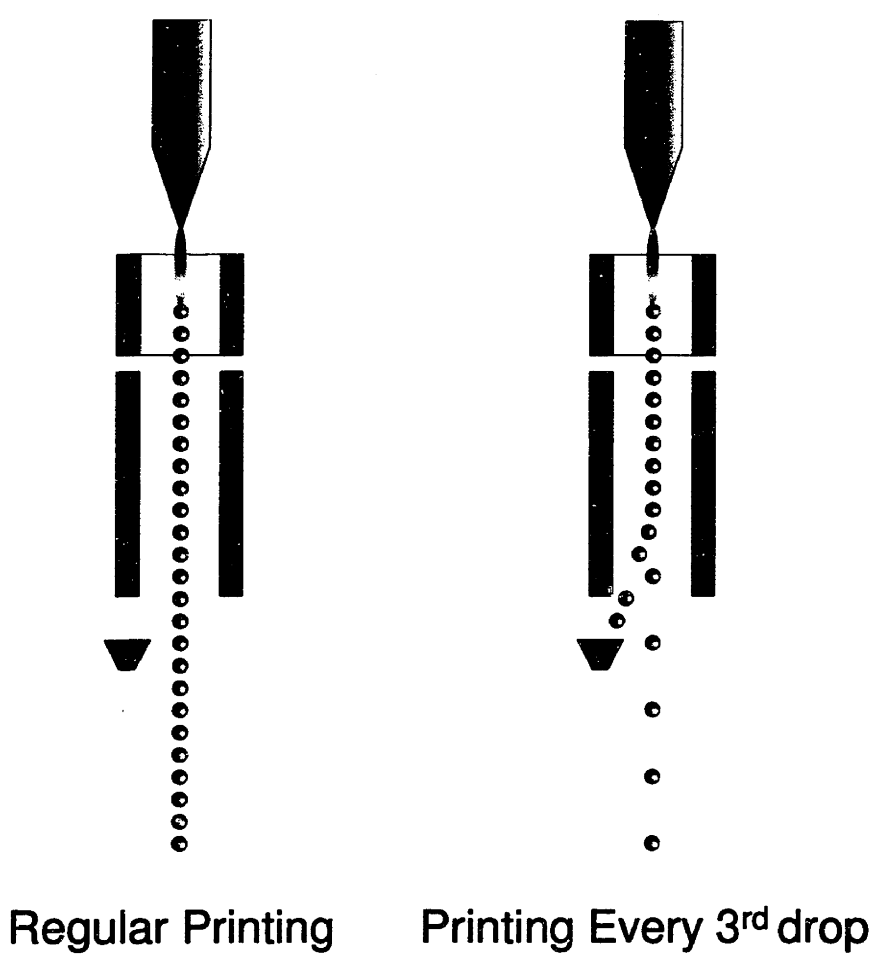
Figure 2.22: Schematic of selective catching mechanism.

Stationary   Regular Speed   High Speed
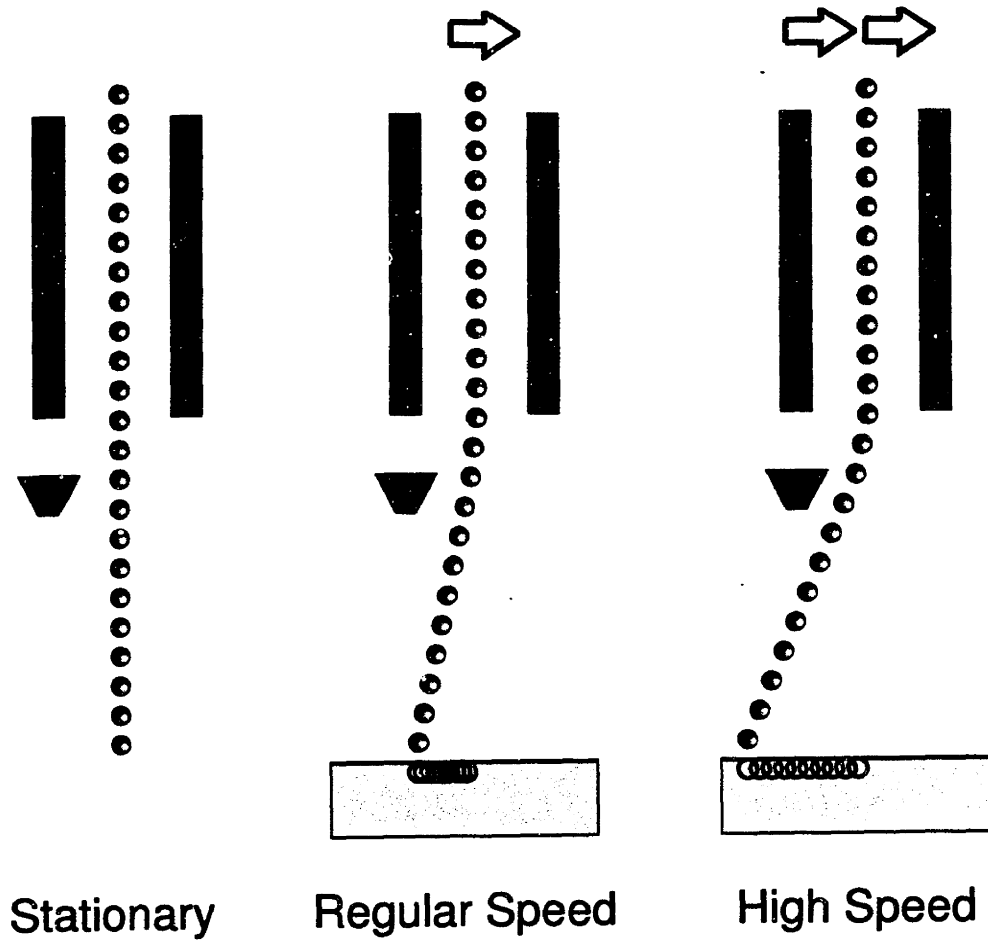
Figure 2.23: The effect of printhead velocity on the binder concentration within a 3D-printed specimen.

Regular Spacing   Small Spacing   Large Spacing
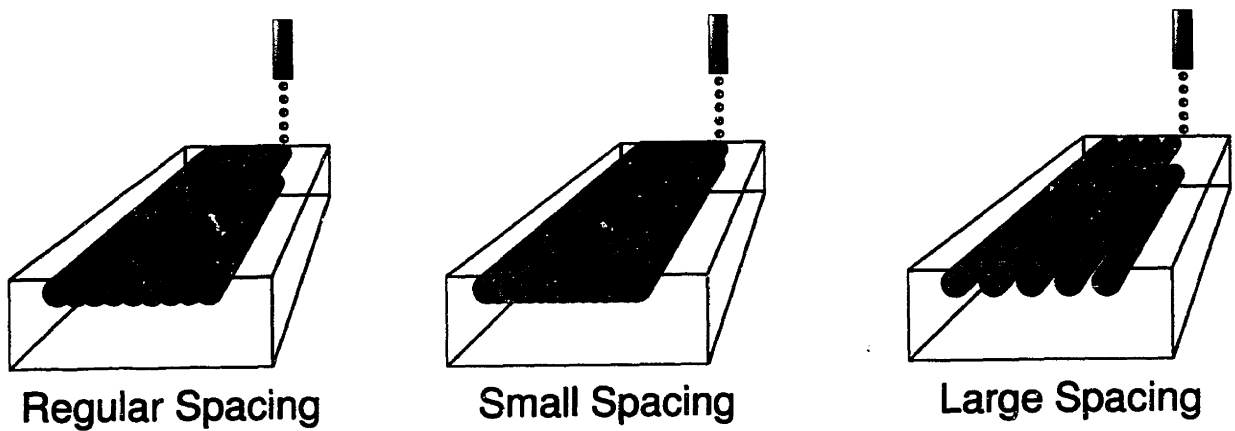
Figure 2.24: The effect of line spacing variations on the 3DP sample.

2.5.3 PRINT STYLES

The effect of binder-powder interaction and binder amount on the final microstructure has been discussed in the previous section. The microstructure and properties of 3D-printed greenbodies also depend on the print style.

The basic 3D-printing procedure involves rastering an ink-jet nozzle in a regular spacing. Lauder observed the formation of cylindrical building blocks upon printing [48]. Neighboring cylinders are then stitched to form a sheet and stacking of these sheets result in 3D object. Figure 2.25 shows a schematic of the stacked cylinders. The defects associated with the regular stacking of these cylinders are easily recognizable from cross sections of greenbodies as shown in Figure 2.26. The presence of these periodic defects are undesirable since not all of these defects can be healed during the isostatic pressing and sintering procedures. The set of instructions that controls the movement of nozzle assembly and the droplet placement in 3DP can be easily modified to change the fashion in which a 3D object is built.

Figure 2.27 is a schematic of the *staggered packing* sequence. Each line of binder is deposited strategically so that the cylindrical blocks pack much closer to each other. The thickness of each layer was also decreased to promote a better inter-layer stitching. Giritlioglu and Bang reported substantial increase in the green strength of 3D-printed ceramic components by using the staggered packing method [46,51]. The anisotropy in the modulus of rupture (MOR) in green samples was reduced even further by implementing a *checker style* printing method [51]. This technique breaks down lines into a series of small segments. The arrangement of the neighboring line segments are controlled to form a checker board-like configuration. Figure 2.28 illustrates the checker style printing scheme. The originally unprinted portions of the line segment are filled with binder on a second set of printhead passes prior to spreading a fresh layer of powder. These patterns are also arranged in three dimensions to reduce the anisotropy in the green strength of 3DP components. Print algorithms such as the ones described above had a significant impact on the microstructure of green ceramic components. However, Giritlioglu reported that the most of the anisotropy in properties are eliminated during the

subsequent densification process. Mechanical properties of dense alumina components constructed by different print styles showed no significant variance [46].

178 μm

170 μm
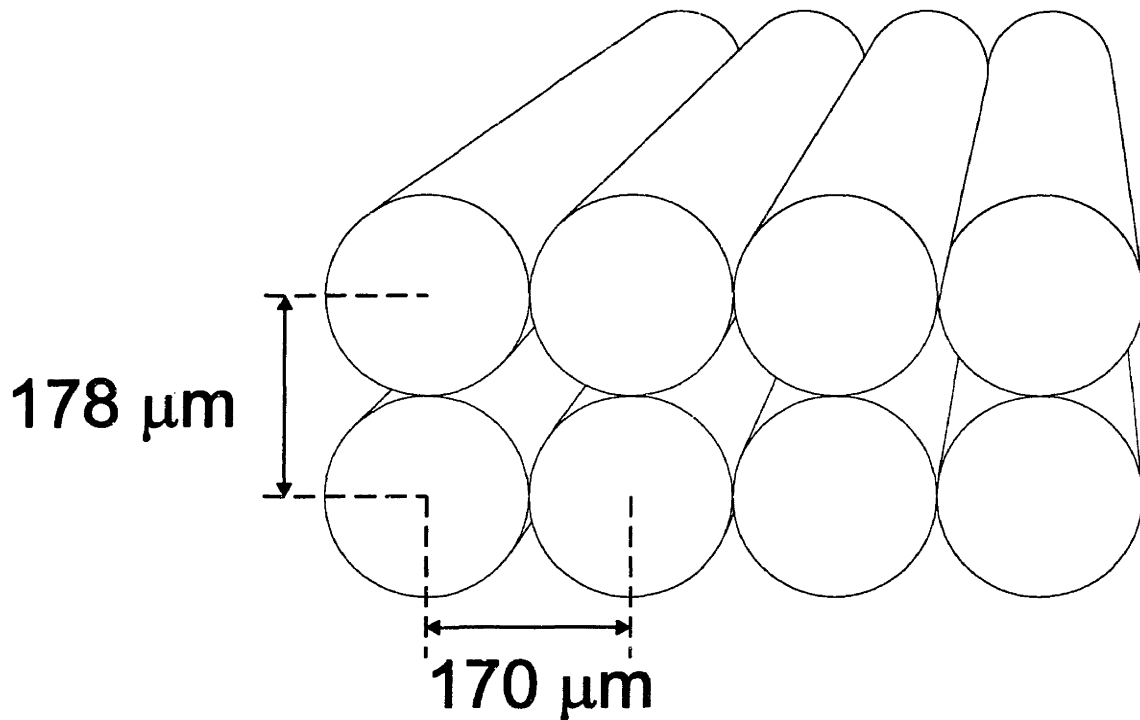
Figure 2.25: Stacking of printed lines in a linear raster pattern.

500μm

Z

Slow

Figure 2.26: Polished cross section of 3DP alumina specimen showing large pores between layers. Linear raster pattern was used to build the sample. (Giriltioglu [46])
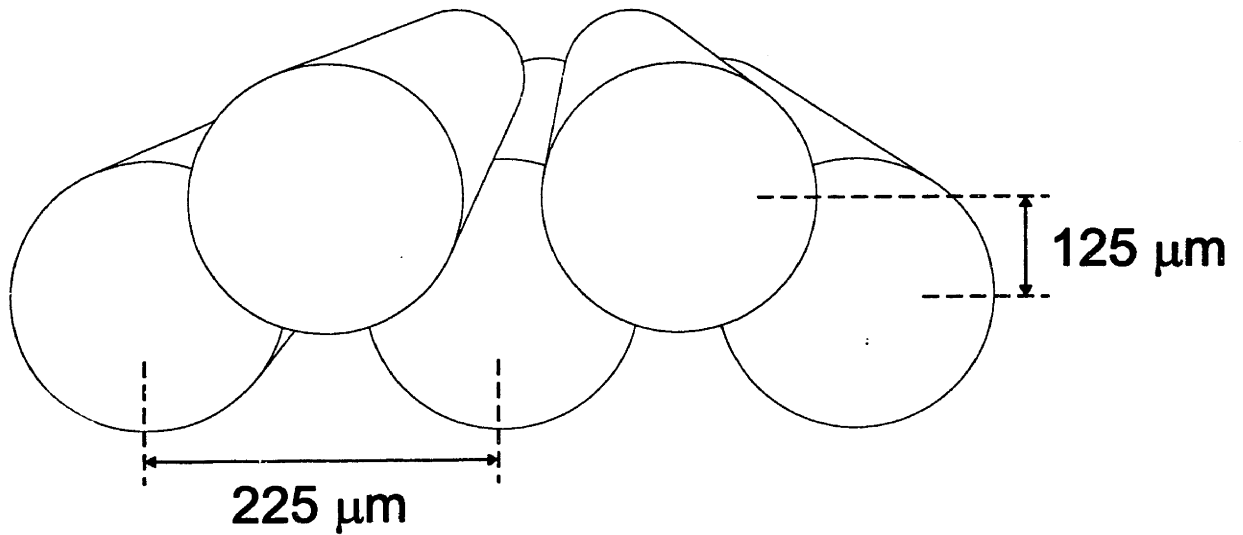
Figure 2.27: Schematic of staggered printing pattern for 3DP.

Figure 2.28:   Schematic of checker style printing method. A second pass of printhead
deposits binder in a complimentary pattern to the one shown above. These
patterns are stacked in three dimensions to form a true 3D-checker board type
printing pattern.

2.6 CONCLUSION

Three distinct methods to construct greenbodies for dense ceramic components have been examined. Specimens prepared by all three methods had nearly full density after firing. Distortion in the press-rolled samples was an indication of non-uniform powder packing in the green stage. Spray-dried granules, on the other hand, showed uniform packing and high final density. Flexural strength of fired and ground specimens from both methods were comparable to conventionally prepared alumina. Specimens from spray-dried method had higher strength at 400 MPa, while that of press-rolled specimen was 324 MPa. Alumina components from spray deposition technique showed high and uniform green density. Spray-deposited components can be directly fired to full density. The potential benefits of using spray deposition method are numerous. Elimination of an isostatic pressing step is an example. Multiple spray heads can be used to deposit powder layers that consist of several materials. Relatively slow build time and complex binder requirement, however, made it less desirable for use as a baseline process for building computer-derived microstructure in this study. Spray-dried granule method was chosen instead, for its simplicity and rapid build rate.

Figure 2.29: Sintered silicon nitride (SNN) pre-ignition chamber for diesel engine.

Several different materials have already been fabricated by spray-dried granule method. Giritlioglu used spray dried silicon nitride granules to build sintered silicon nitride (SNN) components [21]. These SNN specimens showed average flexural strength

of 570 MPa. Figure 2.29 shows a SNN pre-ignition chamber created by SD method. A feldspar/nepheline glass powder was also spray dried and used for printing by Nammour and Rynerson [21,39]. Spray dried mixtures of tungsten carbide and cobalt powders were also used to create components by Caradonna [52].

Process conditions for structural ceramics have an enormous impact on the performance of the component. 3DP is not an exception. The additive nature of the 3DP, however, makes it possible to monitor and control the microstructural development during the construction of greenbodies. These process variables can be integrated into the design process to provide wide range of microstructures and properties within a component. Countless possibilities arise when nozzles are used to deposit second phase material that will alter the characteristics of the matrix powder layer. The amount of the second phase can be controlled by the parameters mentioned in section 2.5 or the combinations thereof. The process parameters described in the current chapter were used to manipulate the microstructures in ZTA specimens with computer-derived microstructure as will be discussed in Chapters 3, 4, and 5.

3. Zirconia Toughened Alumina: First SCC Model System

3.1 BACKGROUND

The zirconia toughened alumina (ZTA) system was chosen as the first model composite system to demonstrate the computer-derived compositional variation by 3DP. ZTA consists of fine, uniformly dispersed zirconia particles in a matrix of alumina. Typical ZTA components require only 15 to 20% volume fraction of zirconia dispersed in alumina to attain optimum strength[31]. Fine particle size and narrow particle size distribution are also required. The mechanical properties of zirconia containing ceramics can be tailored by controlling the phase transformation characteristics of the zirconia particles [53]. Many factors influence the transformation behavior. Stabilizing the zirconia particles by introducing dopants such as Y_2O_3 and CeO_2 have been widely used to control the properties of ZTA. These characteristics make the ZTA system a perfect candidate for exploring the spatially controlled composition (SCC) capability of 3DP process.

3.1.1 TRANSFORMATION TOUGHENING

Zirconium oxide exhibits a phase change upon cooling from high temperature. The tetragonal high temperature form transforms to the monoclinic form at 1170°C, this reaction is described by the following equation:

$$ZrO_{2 \text{ tetragonal}} \Leftrightarrow ZrO_{2 \text{ monoclinic}} \text{ (1170°C)} \tag{3.1}$$
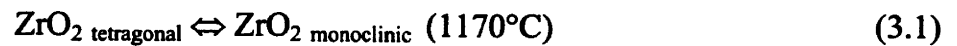
The transformation from tetragonal to monoclinic is the basis of the toughening mechanism in zirconia containing ceramics. Three to five percent increase in volume and shear accompany the tetragonal to monoclinic phase transformation of unconstrained ZrO_2 particles. Several factors determine the stability of the tetragonal zirconia (t-ZrO_2) particles. The thermodynamics of ZrO_2 can be explained by considering the free energy change associated with the transformation [31].

$$\Delta G_{total} = \Delta G_{chemical} + \Delta U_{strain} + \Delta U_{surface} \tag{3.2}$$

ΔG_{total} is the total free energy change from the transformation which must be a negative value for the t-ZrO_2 particles to undergo phase change to m-ZrO_2. $\Delta G_{chemical}$ is the chemical free energy term that decreases as the temperature decreases. Addition of stabilizers such as Y_2O_3, CaO, MgO, and CeO_2 increase the $\Delta G_{chemical}$, resulting in a decrease in the transformation temperature.

Figure 3.1 shows the phase diagram of ZrO_2-Y_2O_3 system which is widely used for different structural and electronic applications [54].
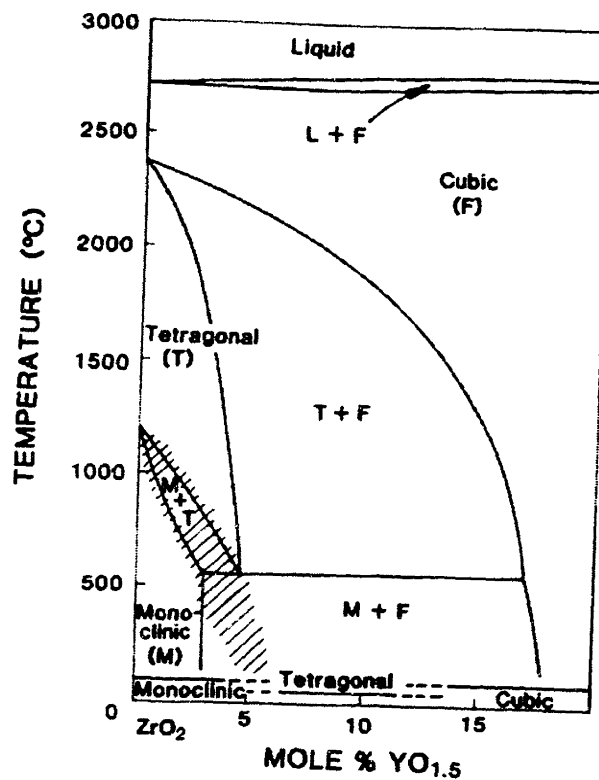
Figure 3.1: Yttria-Zirconia phase diagram. (Scott [54])

The surface energy of t-ZrO_2 is lower than that of m-ZrO_2 and $\Delta U_{surface}$ term has a positive value. This is the main cause for the particle size effect on the transformation behavior of ZrO_2. $\Delta U_{surface}$ term scales with the square of the particle size while $\Delta G_{chemical}$ term scales with the cube, causing finer particles to be more stable. Other evidence of the surface energy term's importance is the fact that particles with irregular shape are less stable than the equiaxed ZrO_2 particles [55]. Equiaxed particles have the lowest possible surface area per given volume. The contribution of, ΔU_{strain}, the strain

energy term is the increase in the stability of ZrO_2 particles constrained in a matrix. Zirconia toughened ceramic (ZTC) materials use this concept to enhance the toughness by embedding zirconia particles in a stiff matrix [31-33].

Tetragonal ZrO_2 phase is retained in the ZTC at room temperature only to undergo transformation when crack propagation releases the constraint and provide energy for the phase transformation [56,57]. The fracture energy required to propagate the crack tip increases due to this transformation. Volume expansion of the particles accompanies the reaction and puts a compressive stress near the transformation zone. The local stress at the crack tip is reduced since the compressive transformation zone forms around the crack. This clamping force impedes the cracks propagation under given far-field applied stress or even causes an arrest of a crack tip. Other toughening mechanisms of ZTC are microcracking and crack tip deflection. Stress-induced transformation of ZTC may form microcracks around the transformed particles. This microcrack zone around the propagating crack reduces the stress near the tip in the same fashion the compressive zone shields the crack tip. Crack tips are also known to be deflected in ZTC. Deflection of crack tips have two effects on the increase of fracture toughness [56]. Deflected crack tip may change the fracture mode from a simple Mode I to a mixed modes, in which case the tip is not under maximum tensile load. A consequence of crack tip deflection is the rough fracture surface. Friction from the opposing faces of rough crack also contributes to the enhanced fracture toughness. Figure 3.2 illustrates different toughening mechanisms for transformation toughened ceramics.

Grinding of ZTC also initiates the tetragonal to monoclinic transformation of ZrO_2 particles near the surface [58,59]. Volume expansion of the particles resulting from the phase change develops a compressive residual stress on the thin surface layer. Typical 320 grit diamond wheel grinding causes a transformation layer of ~15μm and compressive stress of around 150 MPa. [60] An increase in bend strength and contact damage resistance of the as-ground ZTA specimen over the annealed specimen is an evidence of the residual stress. This is analogous to the strengthening mechanism of tempered glass.

Transformation Zone Shielding   Microcrack Zone Shielding

Crack Deflection
Friction of Serrated Grains
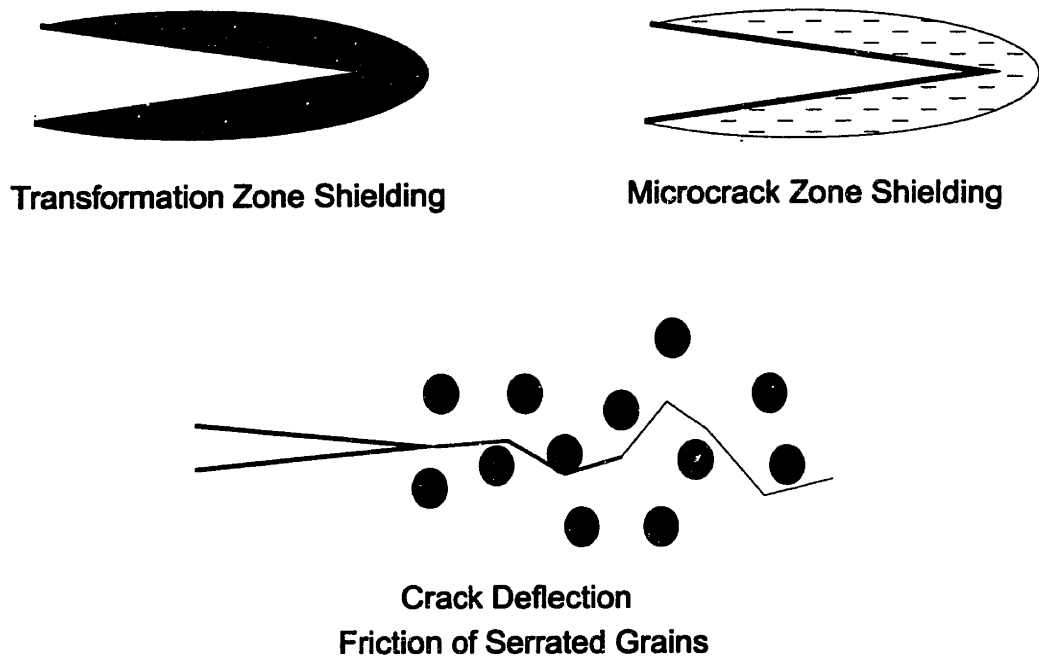
Figure 3.2: Different toughening mechanisms in ZTC.

Various techniques have been developed to fabricate ZTA components with thermally inert compressive surface [61-64]. Green reported that surrounding Y_2O_3-doped ZTA components with undoped ZrO_2 powder during annealing treatment was effective in introducing a compressive surface layer [61]. The diffusion of Y_2O_3 out of the components' surface to the surrounding powder destabilized the surface ZrO_2 particles and subsequent phase transformation allowed the development of compressive stress near the surface. The depletion of stabilizer is a diffusion process and the thickness of the depletion zone scales with the square root of time. Prolonged annealing times are required to introduce a surface layer of thickness around 30 μm [61].

Relationship between strength of a plate and a surface flaw is described by

$$K_c = \beta \sigma \sqrt{\pi a} \qquad (3.3)$$

where K_c is the fracture toughness, β is the geometric factor, σ is the strength at fracture and a is the crack length [65]. Strengths of ZTA specimens with varying surface flaw sizes are shown in Figure 3.3. K_c of 4 MPa$\sqrt{m}$ and $\beta = 1.1$ was used to calculate the strength. Flaw sizes of 50 μm to 200 μm which is typical from machined ceramic

surfaces dramatically reduce the fracture strength as shown in the figure. Surface compression layer must be thicker than these values to enhance the fracture strength. Green's heat treatment technique is not suitable to introduce such compression depth.
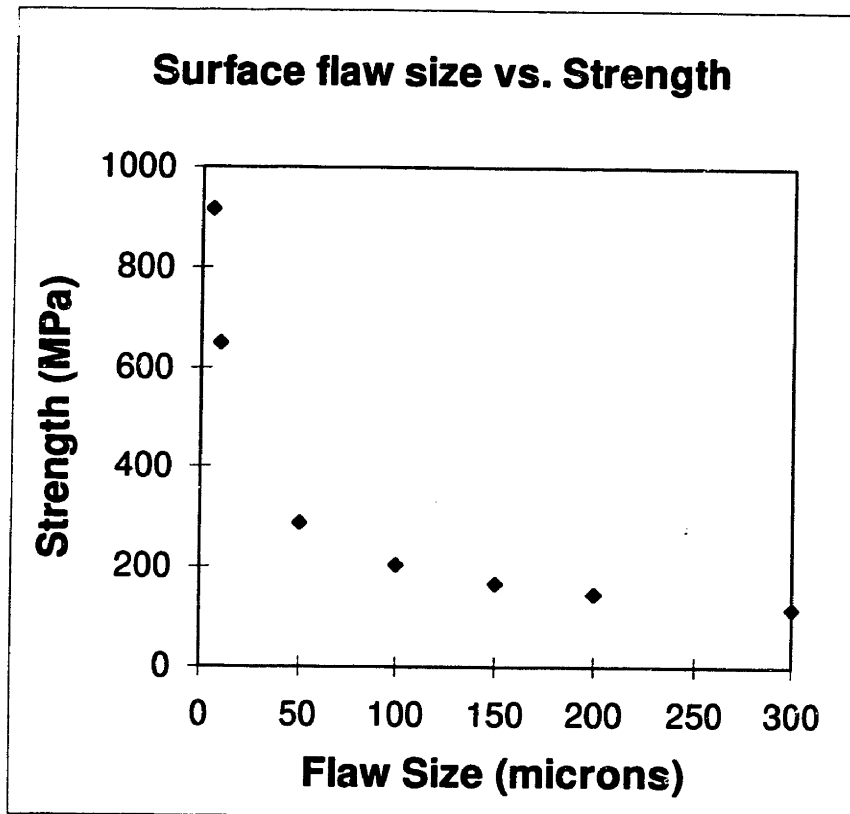
Figure 3.3: Surface flaw size vs. Strength in ZTA.

Virkar et al used dry pressing of different powder mixtures to prepare ZTA components with a substantially thicker surface compression layer [62]. Mixtures of undoped ZrO_2 and Al_2O_3 powders were placed in a dry pressing die, followed by a powder mixture that contained yttria stabilized zirconia and alumina. Another layer of undoped powder mixture was placed in die before compaction. Figure 3.4 is a schematic of the trilayer composite system prepared by dry pressing. A substantial increase in bend strength was observed due to the presence of compressive residual stress. Similar specimens were prepared by Cutler et al through casting slurries of different compositions. Two separate alumina-zirconia slurries were used to cast alternating layers of powder mixtures [62]. Electrophoretic deposition of different slurries were also used by Nicholson et al to build similar structures [64,66].

Cold Pressing of Trilayered Composite
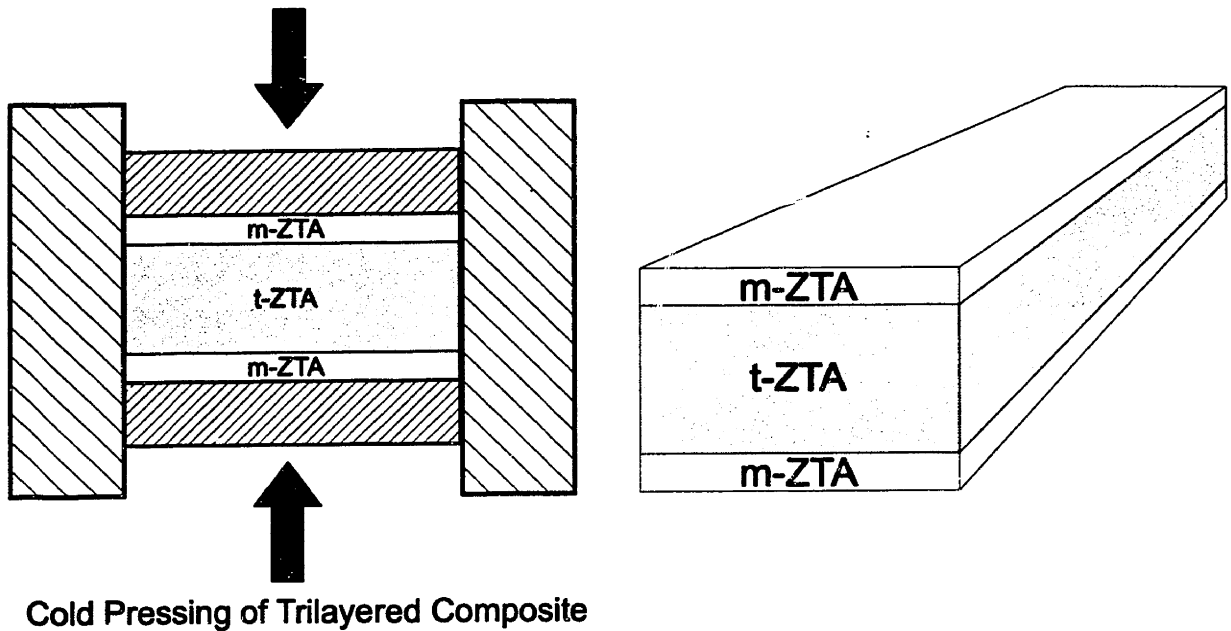
Figure 3.4: Schematic of a dry pressed three layer composite. (modified from Virkar et al. [62])

Although the layered pressing and casting methods eliminate the prolonged heat treatment step associated with Green's approach, it is difficult to manufacture complex shapes with compressive surface layer using such a method. Moreover, it becomes almost impossible to prepare complex shapes with a slight compositional variation by using these techniques. 3DP, on the other hand, is an ideal technique to control the compositional variation required to introduce complex residual stress profiles. The microstructure can be controlled independently of the specimen geometry. The following section discusses different strategies designed to fabricate ZTA components with tailored compositional profile by 3DP.

3.2 STRATEGIES FOR 3DP OF ZTA

Two different base strategies are available for building ZTA by 3DP. One method involves spreading of alumina and depositing zirconia slurry through nozzle. The components prepared by this technique may have localized variation in zirconia volume fraction. Both pure ZrO_2 and Y_2O_3-doped ZrO_2 particles can be used to prepare slurries that will be dispensed separately to control the residual stress. Electrostatically stabilized alumina slurries with up to 40% solids loading have been successfully printed by

Khanuja [40]. Solids loading in the zirconia slurries need to be only 12.5% in order to fabricate ZTA components with 15 vol% ZrO_2. This assumes the packing density of 40% in the alumina powder layers and typical printing parameters as shown in Table 3.1.

Table 3.1: Typical printing parameters

Printing Parameters	Typical Conditions
Printhead Speed	165 m/sec
Line Spacing	178 μm
Layer Spacing	178 μm
Flow Rate	1.2 cc/min
Packing Density	40% Theoretical

The second approach involves the use of 3DP to selectively deposit stabilizer for ZrO_2. Alumina and zirconia powders are pre-mixed to ensure a uniform distribution. A liquid vehicle carrying the stabilizer in a form of slurry or molten salt can be printed on only the selected regions to control the phase transformation characteristics of the ZTA component. The solids loading for Y_2O_3 slurry to achieve the final doping level of 2 mol% is only 0.56% in this technique. Using a salt solution of $Y(NO_3)_3$ reduces the difficulty in printing even further by completely eliminating the need to pass solid particles through a nozzle. Both of these methods have been investigated to prepare ZTA components and the results are reported in the following sections.

3.2.1 PRINTING SLURRIES

Undoped ZrO_2 (TZ-0, Tosoh Corporation, Tokyo, Japan) was used to prepare slurry with 5 vol% solids loading for printing. Nitric acid wad added to maintain the pH of the slurry at 3. The slurry was ballmilled with ZrO_2 grinding media for more than 24 hours to break the agglomerates. The filtration and nozzle setup used to deposit the zirconia slurry was similar to that prepared by Khanuja [40]. Two statistical capsule filters (Micron Separations Inc., Westboro, MA) of 5 μm mean pore size were used in series to trap agglomerates. 15 μm sintered stainless inline filter was placed very close to the ceramic nozzle to eliminate any flocs that may have formed after passing through the capsule filters. The slurry jet through the ceramic nozzle was stable for several hours.
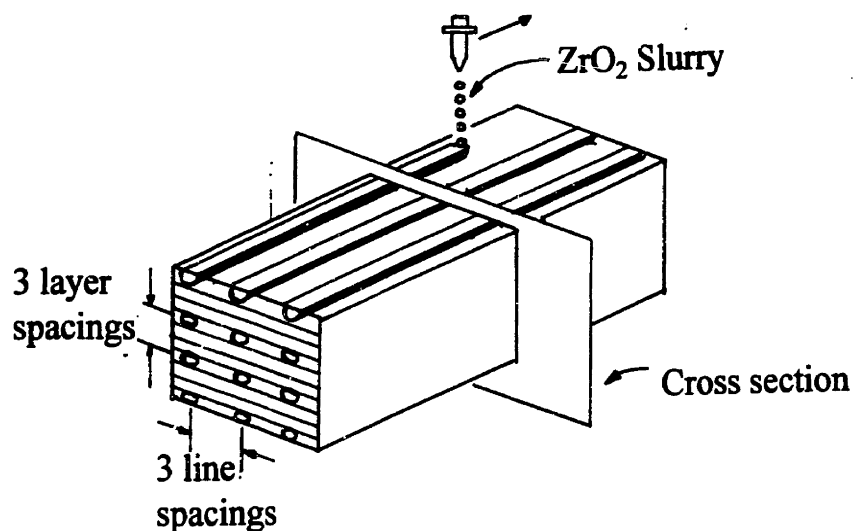
Figure 3.5: Schematic of 3D-printed ZrO_2 lines in a press-rolled alumina powder.

Fine alumina agglomerates were spread into 150 μm layers by using press-rolling sequence. Figure 3.5 shows the schematic of the series of lines printed with the ZrO_2 slurry. The sample was CIPed at 275 MPa and then fired at 1550°C for 4 hours. SEM micrograph of a polished cross section is shown in Figure 3.6. The micrograph was taken in backscatter mode and each bright feature represents a cross section of a line surrounded by alumina matrix. Figure 3.7 is a higher magnification photo of a printed region, also taken in backscatter mode. It is clear from Figure 3.7 that the zirconia particles deposited thorough nozzle do not distribute evenly within the alumina matrix. The zirconia particles start to slipcast on the surface of the alumina agglomerates. This is an undesirable behavior since an intimate mixing of alumina and zirconia is necessary to ensure an optimum toughness in ZTA system. The powderbed characteristics need to be tailored to allow an instant redistribution and mixing of printed particles in order for this method to work properly.
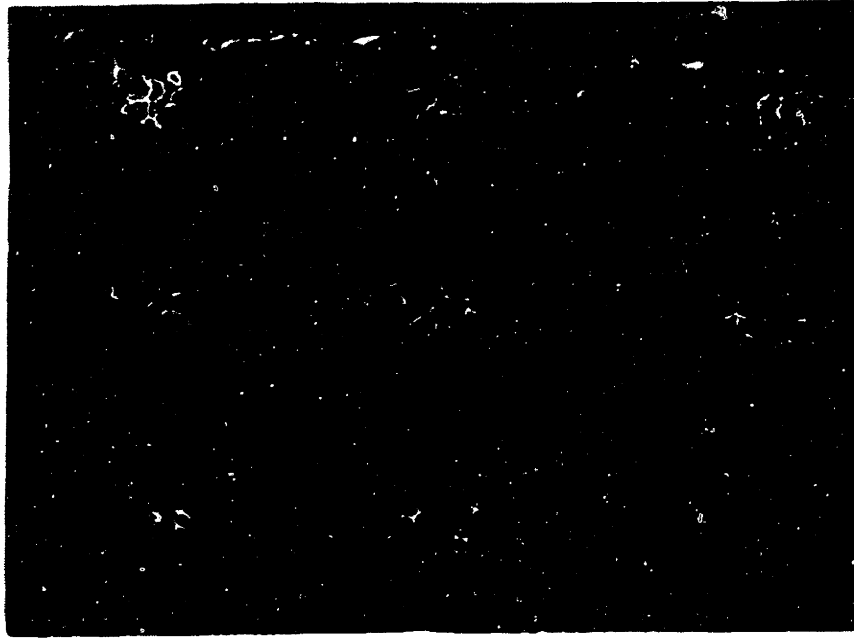
Figure 3.6:   Polished cross section of ZrO_2 lines printed on press-rolled alumina powderbed. Specimen was CIPed and fired prior to sectioning. Each bright feature is a printed line of ZrO_2.
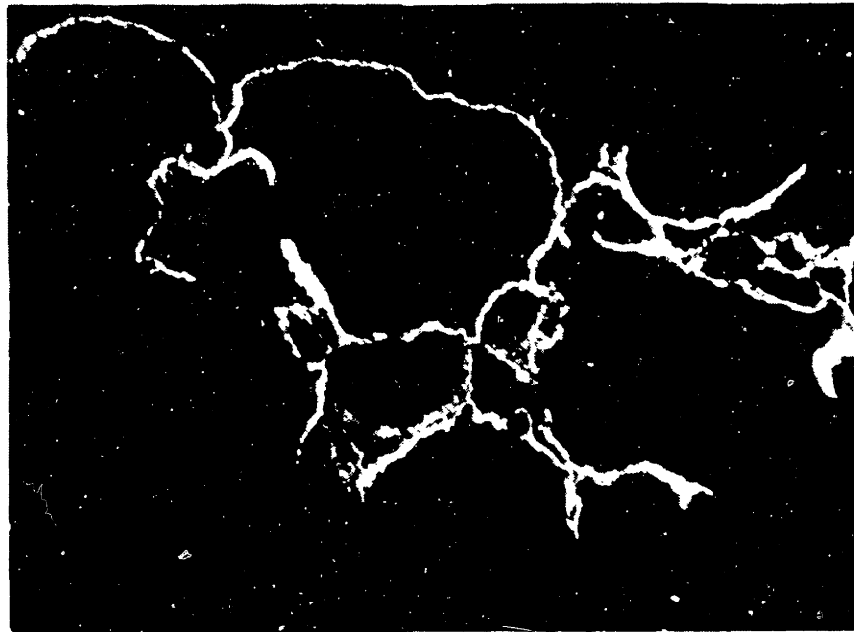
Figure 3.7:   Polished cross section of a 3D-printed ZrO_2 line on press-rolled Al_2O_3 powderbed. ZrO2 particles apparently slipcast on surfaces of Al_2O_3 agglomerates.

3.2.2 PRINTING SALT SOLUTIONS

Solutions containing the precursor for yttria were printed on a mixed powderbed to selectively dope ZrO_2. It was also necessary to deposit a polymeric binder, in addition to the salt solution, so as to provide structural integrity in the printed region. Two separate approaches were available to dispense both structural and chemical binder components to the ZTA powder layers. These methods are summarized in Table 3.2. The details of the process sequence is illustrated in Figure 3.8.

Table 3.2: Alternative methods to add yttrium nitrate salt to ZTA powder mixture.

Methods	Jet 1		Jet 2	
	Content	**Resulting Phase**	**Content**	**Resulting Phase**
Method 1-1	Yttrium Nitrate	t-ZTA	Acrysol	m-ZTA
Method 1-2	Acrysol	m-ZTA	Yttrium Nitrate	t-ZTA
Method 2	Rhoplex	m-ZTA	Yttrium Nitrate and Rhoplex	t-ZTA

Acrysol is deposited to hold the parts together while another nozzle is used to dispense aqueous solution of $Y(NO_3)_3$ in the first method shown in Figure 3.8 (a). The stabilized regions of the specimen must be printed with both jets, while it is only necessary to print the unstabilized region with Acrysol. An intermediate drying step is required to remove moisture from the powderbed before proceeding to print second time. This eliminates the binder bleeding phenomenon which is observed when excess moisture is applied to a powder layer. The salt solution was always printed first on a freshly spread powder layer in order to avoid any non-uniform distribution of the stabilizer within a printed region. This decision was based on the observation that excess Acrysol forms a layer of film on the top of a printed layer as described in section 2.2. Figure 3.8 (b) shows a reversed sequence that may lead to the segregation of the stabilizer.

(a)

Yttrium nitrate salt   Acrysol

(b)

Acrysol   Yttrium nitrate salt

(c)

Rhoplex   Yttrium nitrate
and Rhoplex
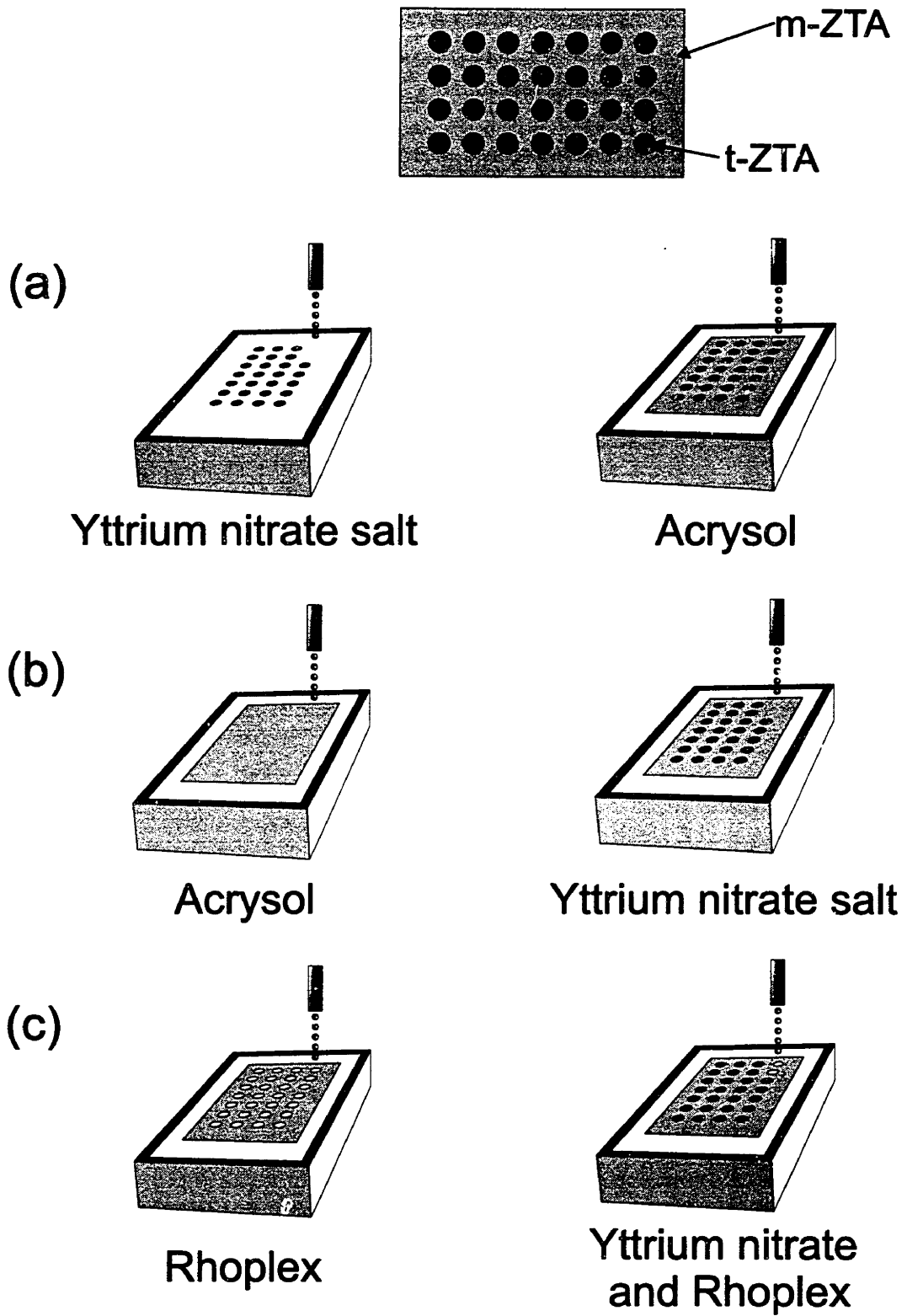
Figure 3.8: Alternative approaches to introduce yttrium nitrate salt into premixed powder
        of ZrO_2 and Al_2O_3.

The second method, described in Table 3.2, also uses two separate fluid systems to deposit binder and dopants. One nozzle was used to dispense a latex emulsion (Rhoplex HA-16, Rohm and Haas, Philadelphia, PA) which formed bridges between spray dried granules upon drying. The other nozzle was used to deposit a mixture of Rhoplex and the $Y(NO_3)_3$ salt solution. The addition of salt solution does not compromise the stability of latex emulsion in Rhoplex which is a sharp contrast to the Acrysol system. Mixing of the salt solution in Acrysol initiates an instant precipitation of the acrylic copolymer which makes it impossible to jet through nozzle. The advantage of printing a mixture of dopant and polymer is that an intermediate drying step can be eliminated. No regions within a component need to be printed twice. This concept is illustrated in Figure 3.8 (c).

3.3 MONOLITHIC ZTA PARTS

Selective doping methods described in section 4.2.2 were used to prepare different types of ZTA components. This section discusses results of the 3D-printed monolithic ZTA components, both tetragonal ZTA (t-ZTA) and monoclinic ZTA (m-ZTA). Properties of these samples were used to design and fabricate the ZTA components with tailored compositional variation. The results of the compositionally graded ZTA specimens will be discussed in Chapters 4 and 5.

3.3.1 POWDER PREPARATION

Spray drying of alumina and undoped zirconia was used to prepare a powder mixture with uniform distribution. Fine alumina (RC172-DBM) and zirconia (TZ-0) particles were used to prepare the co-dispersion for spray drying. Slurry preparation was carried out in two separate steps, designed to promote intimate powder mixing. In the first step, appropriate amount of powders for 85 vol% Al_2O_3 and 15 vol% ZrO_2 were measured and added to ethanol for mixing. The solids loading in the ethanol based slurry was kept very low at 10% to facilitate uniform mixing. The slurry was vibromilled (Sweco Inc., Florence, KY) for 4 hours prior to 24 hours of ballmilling. Ethanol was then allowed to evaporate completely, leaving a dried cake of alumina and zirconia mixture. These chunks easily redispersed in acidic water (pH=3) through subsequent vibromilling

and ballmilling. Polyacrylic acid (PAA, MW 90,000) was added to the water for the slurry, so as to provide strength to the spray dried granules. The amount of PAA was kept at 2 wt% respect to the dry weight of the powder mixture. Micrographs of spray-dried granules are shown in Figure 3.9. Spray-dried ZTA granules were sieved to eliminate both large agglomerates and fines. Granules with diameters between 38 μm and 53μm were used to spread uniformly packed layers. A counter-rolling spread sequence described in Chapter 2 was used in the layering process.
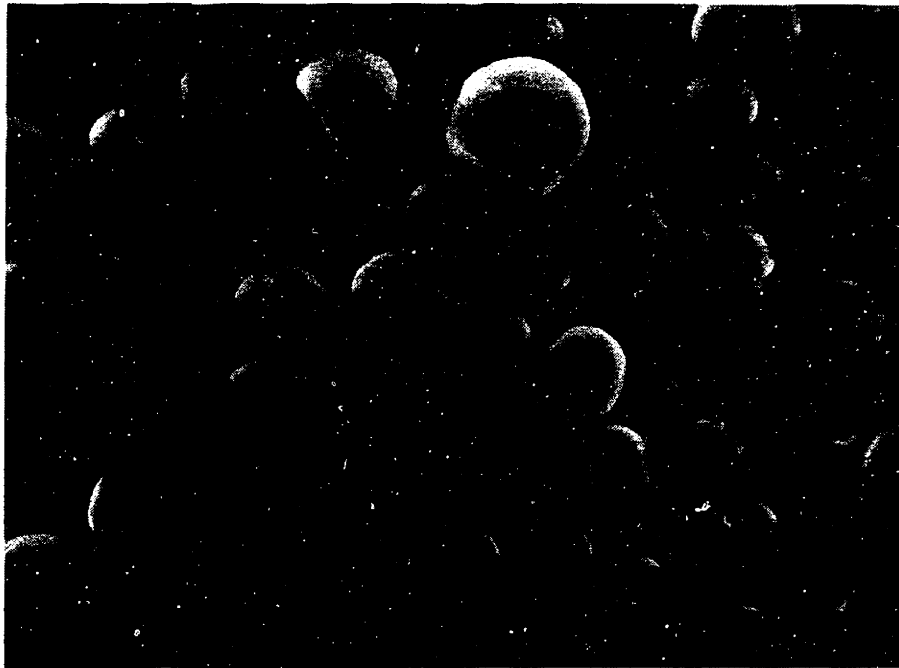
Figure 3.9: Spray-dried ZTA granules.

3.3.2 PRINTING AND POST PROCESSING

Monoclinic ZTA specimens were built by spreading the ZTA spray dried granules, described in the previous section, and then printing Acrysol WS-24 to bind the granules. It was not necessary to add yttrium nitrate salt to the binder system since the phase transformation of ZrO_2 particles was desired in the m-ZTA components. Green bars were isostatically pressed at 275 MPa in warm oil at 80°C to increase the green density after removing loose powder. The specimens were then fired at 450°C for 3 hours to remove binder. The specimens were fired at 1550°C for 2 hours for sintering.
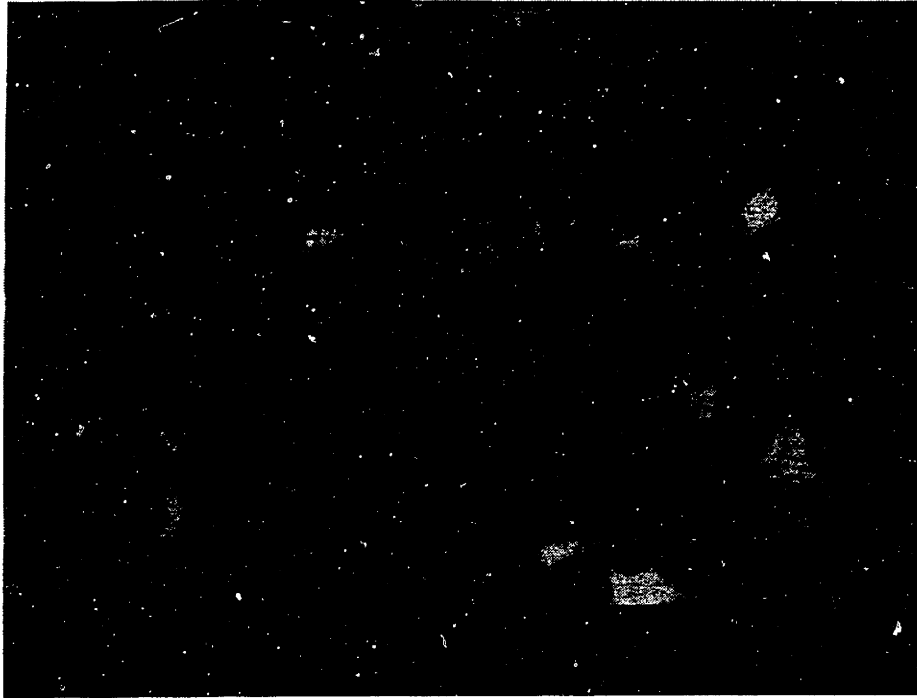
Figure 3.10: Polished cross section of an m-ZTA specimen. The sample was WIPed at 80°C, 275 MPa, and then fired at 1550°C for 3 hours. Average grain sizes of Al_2O_3 and ZrO_2 are 0.88 μm and 0.46 μm, respectively.
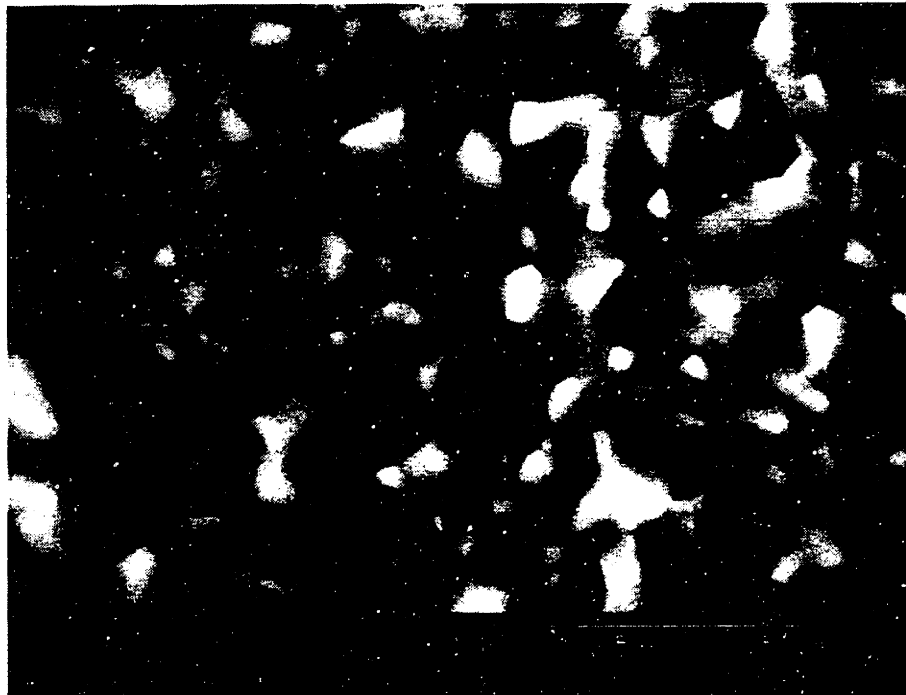
Figure 3.11: Polished cross section of a t-ZTA specimen. The sample was WIPed at 80°C, 275 MPa, and then fired at 1550°C for 3 hours. Average grain sizes of Al_2O_3 and ZrO_2 are 0.79 μm and 0.33 μm, respectively.

The tetragonal ZTA (t-ZTA) bars were prepared by using identical processing steps with the exception of the binder system used. A mixture of aqueous yttrium nitrate salt solution (Aldrich Chemical Company, Milwaukee, WI) and Rhoplex HA-16 was printed. The binder in this case had a dual purpose: binding spray dried granules to form the green body, and to provide yttrium doping of the zirconia particles within the granules. Only one nozzle was required to build monolithic t-ZTA components with this strategy. The yttrium nitrate salt concentration was adjusted so that the mole fraction of yttria in the final parts would be 3% respect to the zirconia content. The isostatic pressing and firing conditions were kept identical to those of the monoclinic bars.

3.3.3 MICROSTRUCTURE

Figures 3.10 and 3.11 show the SEM micrograph taken from the polished cross sections of 3D-printed m-ZTA and t-ZTA specimens, respectively. These specimens were thermally etched at 1400°C in air for 3 hours to reveal grain boundaries. The distribution of ZrO_2 grains in Al_2O_3 matrix was found to be very uniform. This is evidence that the pre-mixing process was very effective. No significant difference was observed between the microstructures of m-ZTA and t-ZTA. The average grain sizes of Al_2O_3 and ZrO_2 in these samples were measured from SEM micrographs by line intercept method and the results are listed in Table 3.3

Table 3.3: Average sizes of Al_2O_3 and ZrO_2 grains resulting from different sintering conditions.

Samples	Grain size (μm)		Pullouts
	Alumina	Zirconia	
m-ZTA, 1550°C, 3 hrs	0.88	0.46	Very Little
m-ZTA, 1600°C, 3 hrs	1.22	0.57	Some
m-ZTA, 1550°C, 6 hrs	1.12	0.61	Extensive
t-ZTA, 1550°C, 3 hrs	0.79	0.33	No
t-ZTA, 1600°C, 3 hrs	1.05	0.56	No
t-ZTA, 1550°C, 6 hrs	0.97	0.45	No
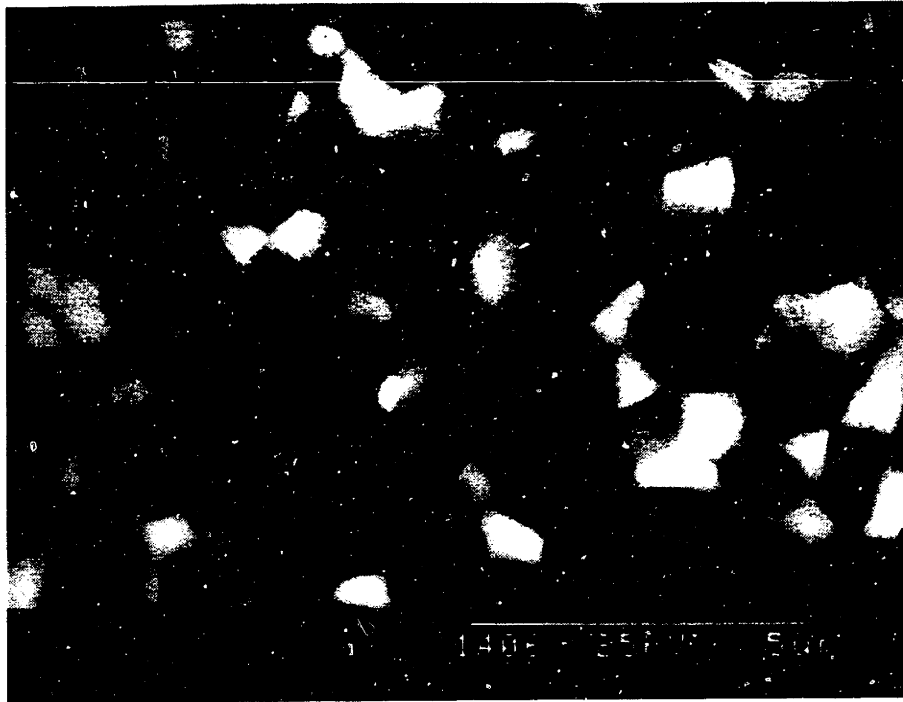
Figure 3.12: Polished cross section of an m-ZTA specimen. The sample was WIPed at 80°C, 275 MPa, and then fired at 1600°C for 3 hours. Average grain sizes of Al_2O_3 and ZrO_2 are 1.22 µm and 0.57 µm, respectively.
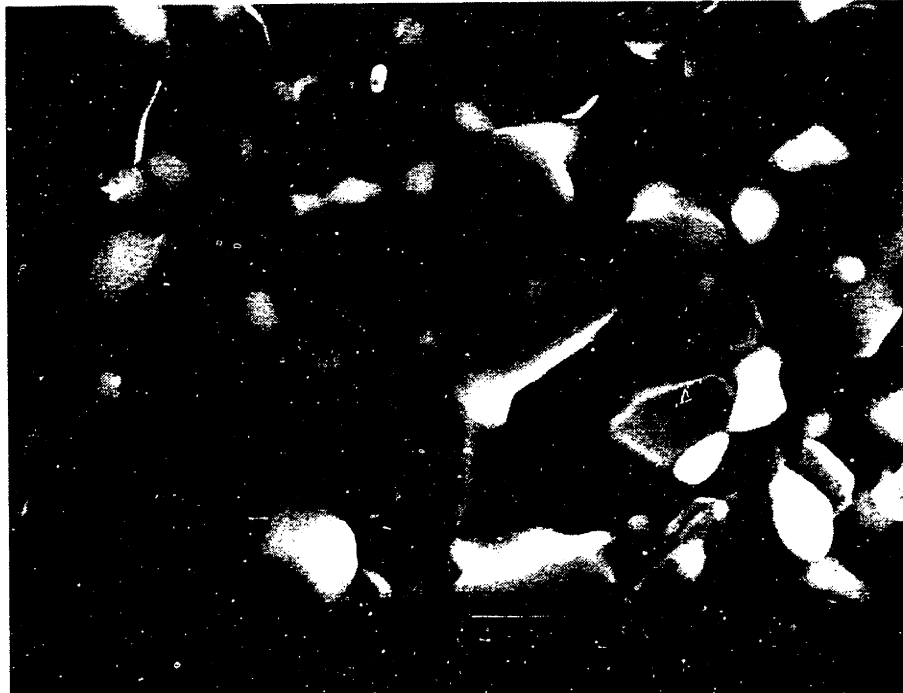
Figure 3.13: Polished cross section of an m-ZTA specimen. The sample was WIPed at 80°C, 275 MPa, and then fired at 1550°C for 6 hours. Average grain sizes of Al_2O_3 and ZrO_2 are 1.12 µm and 0.61 µm, respectively.

Grain growth was observed when the specimens were sintered at higher temperatures and/or for longer duration. Figures 3.12 and 3.13 were taken from m-ZTA components that were sintered at 1600°C for 3 hours and 1550°C for 6 hours, respectively. Grain sizes of Al_2O_3 and ZrO_2 increased for both cases compared to that of the specimen fired at 1550°C for 3 hours. The average size of ZrO_2 grains in these m-ZTA samples were 0.57 μm and 0.61 μm, respectively. Pullouts were observed during grinding and polishing from the surfaces of m-ZTA specimens with large grain size. Tetragonal ZTA samples with large grain sizes, however, did not exhibit any pullouts. These observations can be explained by considering the phase stability of the ZrO_2 grains in the two samples. The t → m transformation of large ZrO_2 grains are more energetically favorable than that of smaller grains as discussed in section 3.1.1. The volume expansion associated with the phase transformation of larger ZrO_2 grains induce microcracking in the surrounding matrix. As a result, surfaces of the m-ZTA components with larger grain size are more susceptible to microcracking and pullouts during grinding. The chemical stability of the Y_2O_3 doped ZrO_2 grains prevent the phase change and no volume expansion or microcracking is observed. This is consistent with the observations by Green et al. Green reported that an extensive microcracking and pullouts were observed with the growth of m-ZrO_2 grain size. These should be avoided to retain the residual compressive stress resulting from the ZrO_2 volume expansion. Pullouts can relieve the stress which will negate the effort to introduce surface compression. Heat treatment conditions need to be chosen to control excessive grain growth of ZrO_2 in m-ZTA components. Heuer reported that for a ZTA with 15 vol% ZrO_2 and 85 vol% Al_2O_3, the critical grain size for transformation was ~ 0.6μm [55]. This is consistent with the observation from 3D-printed m-ZTA specimen and sintering schedule for subsequent samples were optimized in order to keep the average ZrO_2 grain size at ~ 0.6 μm.

3.3.4 X-RAY DIFFRACTION

X-ray diffraction (XRD) patterns from surfaces of ZTA samples were collected to estimate the proportions of monoclinic and tetragonal ZrO_2 phases. Cu$K\alpha$ radiation (λ=0.1542 nm) was used to generate diffraction patterns (RU300, Rigaku Industries,

Japan). Sample surfaces were ground with 320 grit diamond wheel and then polished with 9 μm diamond paste. Some samples were annealed at 1400°C for 16 hours in air prior to obtaining the XRD patterns. Two sets of XRD patterns, one from as-polished surface and the other from annealed surface, were taken from both m-ZTA and t-ZTA specimens. An XRD pattern from an as-ground, *not polished*, t-ZTA specimen was also collected to determine the effect of polishing on the relative fraction of phases present at the surface.

The volume fractions of the monoclinic and tetragonal zirconia particles were determined by using the intensity ratio of the monoclinic (111) and ($\bar{1}$11), and tetragonal (111) peaks, as described by Toraya et. al.[67]

$$V_m = \frac{PX_m}{1+(P-1)X_m} \tag{3.4}$$

$$X_m = \frac{I_m(\bar{1}11)+I_m(111)}{I_m(\bar{1}11)+I_m(111)+I_t(111)} \tag{3.5}$$

where X_m is the integrated intensity ratio and $I_m(hkl)$ and $I_t(hkl)$ represent the integrated intensity from hkl peak of the m-ZrO$_2$ and t-ZrO$_2$, respectively. P is a calculated ratio of intensities in the zirconia polymorphs which Toraya reported to be a constant term, 1.311 ± 0.004. It is important to use V_m, not X_m, to calculate the volume fraction of monoclinic ZrO$_2$ because X_m underestimates the m-ZrO$_2$ by as much as 7.3%. This is a consequence of an assumption that intensity of tetragonal (111) is equal to the sum of the intensities of monoclinic (111) and ($\bar{1}$11). Garvie and Nicholson pointed out that this is not strictly true and the nonlinearity must be compensated [68]. V_m takes into account the difference in the intensity between two phases with the constant term P. Volume fractions of m-ZrO$_2$ were calculated by using equation (3.4) throughout this thesis.

The diffraction patterns taken from m-ZTA components are shown in Figure 3.14. The m-ZTA parts contained 86 vol% monoclinic phase in the as-polished state and 79 vol% after annealing. This indicates the presence of very fine zirconia particles which retain the metastable tetragonal phase even in the absence of any stabilizing agent. The

slight decrease in the fraction of m-ZrO$_2$ during annealing can be attributed to the reversion of the grinding induced m-ZrO$_2$ particles. This was possible because the polishing procedure did not completely remove the surface transformation zone. The t-ZTA parts which were printed with a co-dispersion containing yttrium nitrate salt showed 25 vol% monoclinic phase in the as-ground state. The diffraction pattern from this specimen is shown in Figure 3.15. Polishing removes some of the transformation zone as evidenced by 9 vol% monoclinic phase in the as-polished t-ZTA specimen. The XRD pattern for the annealed t-ZTA specimen shows no apparent monoclinic peak, suggesting almost complete stabilization of the tetragonal phase. The presence of 25 vol% monoclinic phase in the as-ground specimen is also an evidence of the grinding-induced phase transformation near the surface.
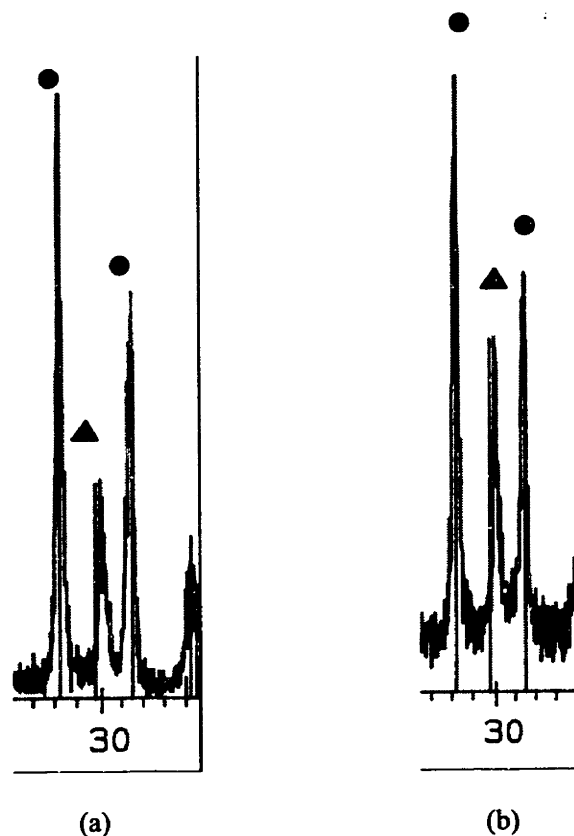
Figure 3.14: XRD patterns taken from m-ZTA specimens. (a) is taken from an as-ground surface. (b) is taken from an annealed surface. (● denote m(111) and m($\bar{1}$11) peaks and ▲ denote t(111) peaks)
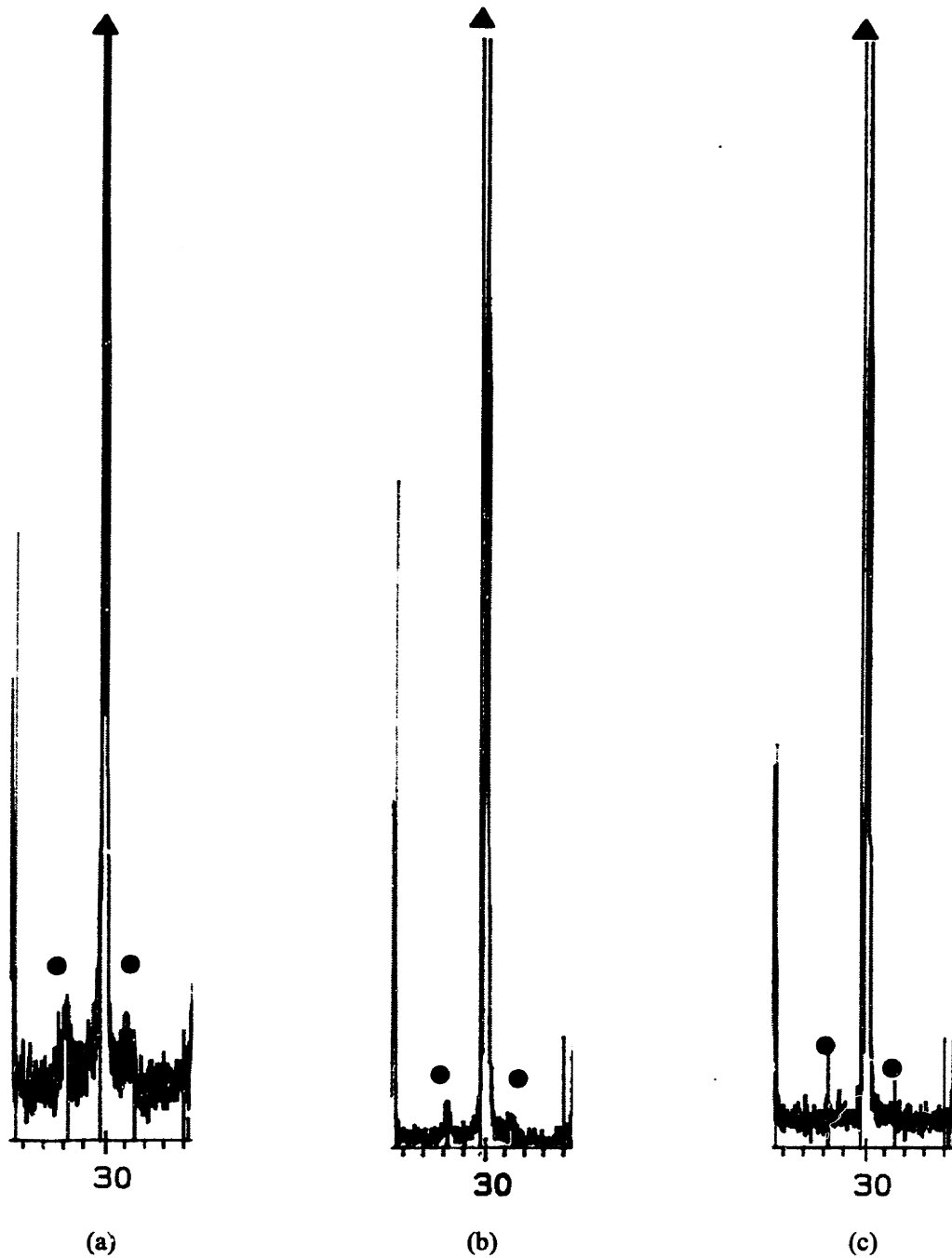
Figure 3.15: XRD patterns taken from t-ZTA specimens. (a) is taken from an as-ground surface. (b) is taken from an as-polished surface. (c) is taken from an annealed surface. (● denote m(111) and m(Ī11) peaks and ▲ denote t(111) peaks)

3.3.5 MECHANICAL PROPERTIES

Procedures

Four point bending tests were conducted on the monolithic ZTA bars. The size and shape of the specimens and the testing procedures were in strict compliance with the ASTM standard C1161-90. The conditions used for bending test are summarized in Figure 3.16. Some of the bend specimens were annealed at 1400°C for 16 hours prior to testing in order to isolate the effect of surface grinding.
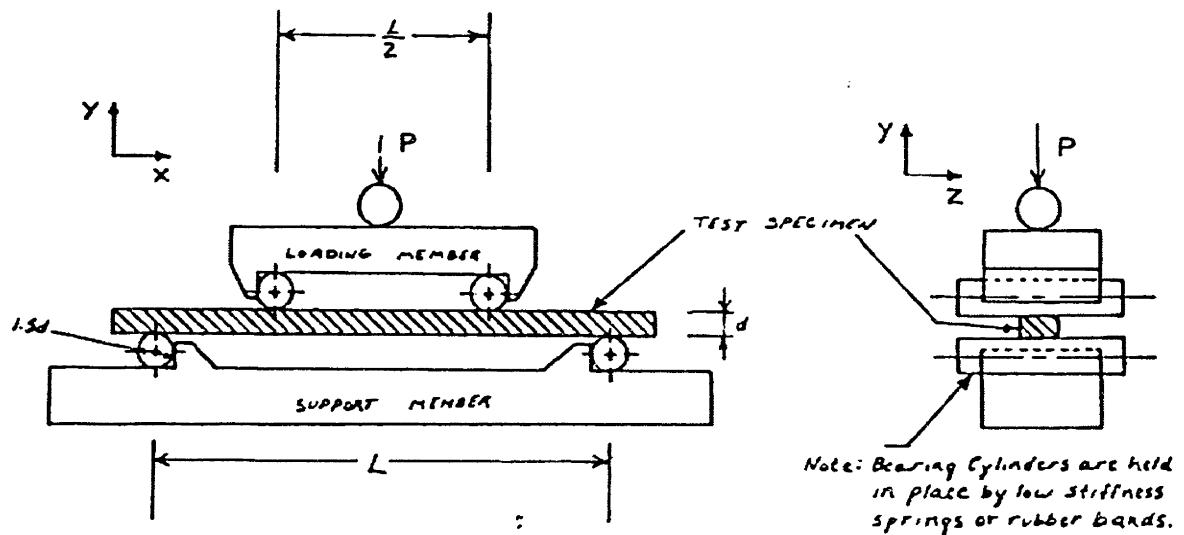
Figure 3.16: Schematic of four point flexural strength test procedure. (ASTM C 1161)

An approximate measure of the fracture toughness of 3DP monolithic ZTA was also obtained by the indentation technique of Anstis et al.[69] with an applied load of 9.8 N. In this technique, sizes of the cracks emanating from the corners of Vickers indents are used to estimate the toughness.

$$K_c = \S_V^R \sqrt{\frac{E}{H}} \left(\frac{P}{C_o^{3/2}}\right)$$
(3.6)

$\S_V^R$ is a material independent constant for Vickers-produced radial cracks and Antis et al reported the value to be 0.016 ± 0.004. E is the elastic modulus of the material and H is the Vickers hardness. P represents the indentation load and C_o is the crack size.

Both 3D-printed m-ZTA and t-ZTA fired specimens were polished to 1 μm finish. Specimens were thermally etched at 1400°C for 3 hours to reveal grain boundaries. Thin film of gold was deposited on the surface prior to indentation to facilitate crack tip observation in the SEM. Indentation tests were also conducted on dry pressed and slip cast ZTA samples to benchmark fracture toughness of 3D-printed ZTA to that of conventionally prepared specimens.

Results and Discussion

The average flexural strengths for the as-ground m-ZTA and t-ZTA bars were 475 MPa and 451 MPa, respectively. Annealed specimens showed strengths of 447 MPa and 427 MPa for the m-ZTA and t-ZTA, respectively. The reduction in strength upon annealing can be attributed to the transformation of the monoclinic zirconia particles back to the tetragonal phase, which relieves the grinding-induced compressive residual stress near the surface.
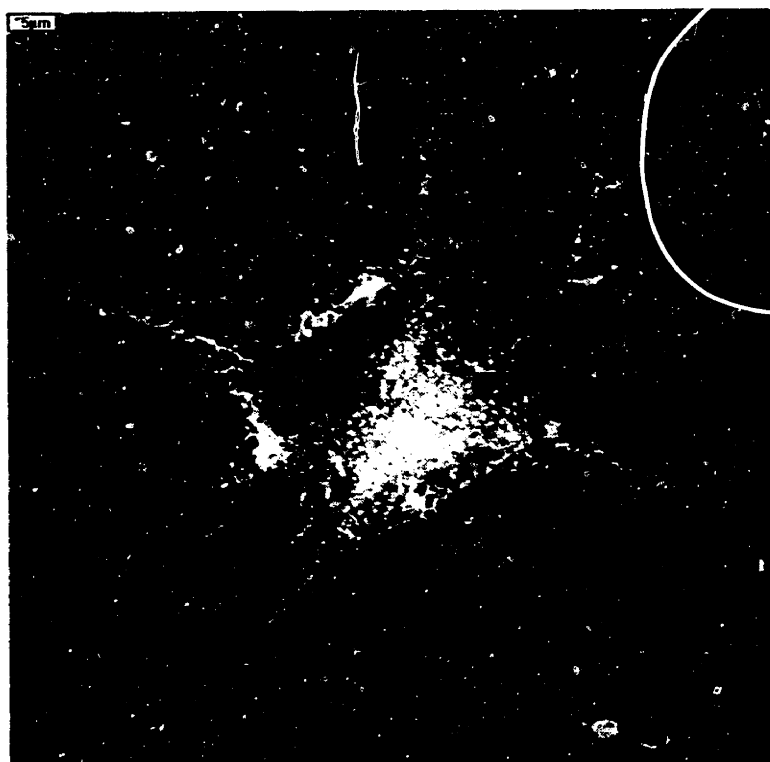
Figure 3.17: Typical Vickers indentation mark on an m-ZTA specimen.
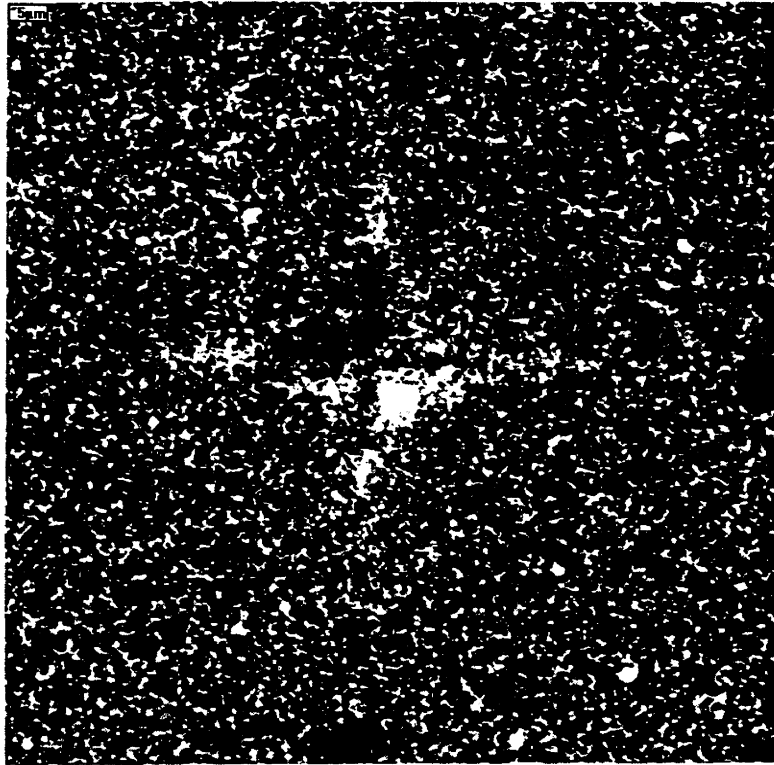
Figure 3.18: Typical Vickers indentation mark on a t-ZTA specimen.
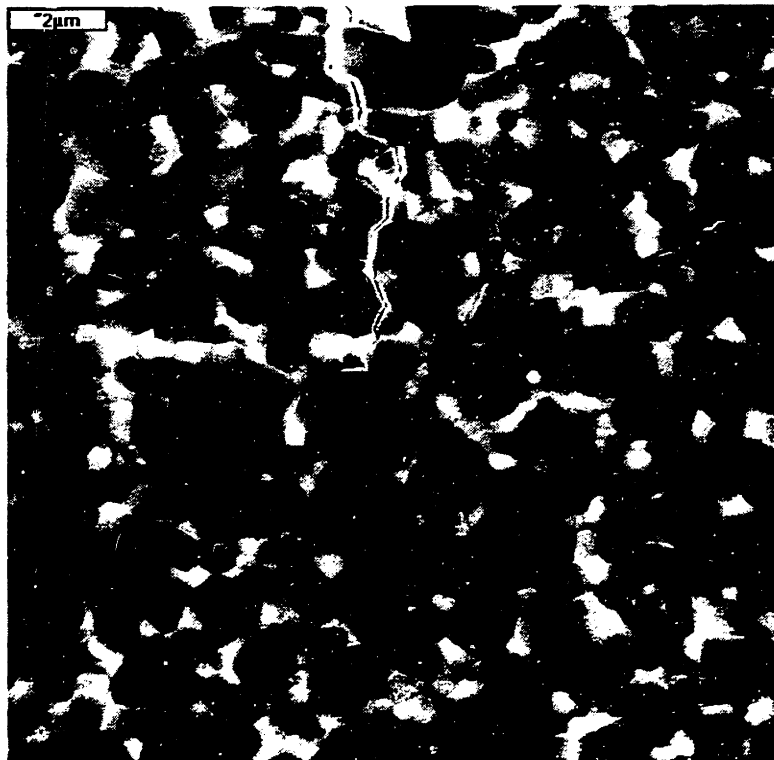
Figure 3.19: High magnification SEM micrograph of an indent crack tip.

Figures 3.17 and 3.18 show typical indentation made on the ZTA components. Crack sizes were measured by observing the crack tips with SEM at 5000X magnification. Figure 3.19 is a high magnification SEM taken from one of the crack tips. Indentation fracture toughness of t-ZTA and m-ZTA were 3.92 and 2.87 MPa$\sqrt{m}$, respectively. The toughness of 3D-printed monolithic ZTA samples are relatively lower than the toughness for ZTA reported in literature, which ranges between 5 and 8 MPa$\sqrt{m}$ for t-ZTA when measured by other techniques such as double cantilever beam (DCB) method [31-34]. Some of these discrepancies can be attributed to the slow crack growth after the removal of the indentation load, as observed by Anstis et al.[69]

Another source the underestimation of toughness is the load dependency of indentation toughness measurements. A series of Vickers indentations with varying loads were made on a ZTA specimen to investigate the load dependency. Figure 3.20 shows the indentation load versus Vickers hardness plot. Also shown in Figure 3.21 is the log(load) vs. Log(K_c) plot which clearly shows the increasing trend in K_c with increasing indent load. Toughness values of 4.25 to 5.0 MPa$\sqrt{m}$ can be extrapolated from the plot for indentation loads 500 N and 1000 N which is typically reported in literature. The load used in this study, 9.8 N, was limited by the capability of the micro-indenter used.

Table 3.4 compares the indentation results between 3D-printed and dry pressed ZTA specimens. It is evident from these data that the properties of the 3DP ZTA components were comparable to conventionally prepared samples.

Table 3.4: Comparison of indentation toughness measurements from 3D-printed and dry pressed ZTA components.

Build Method	Sintering Schedule	Sample Type	Kc (MPa$\sqrt{m}$)
3DP	1550°C, 3 hrs	t-ZTA	3.92
3DP	1550°C, 3 hrs	m-ZTA	2.87
Dry Pressing	1550°C, 3 hrs	m-ZTA	2.58
Dry Pressing	1600°C, 3 hrs	m-ZTA	4.19
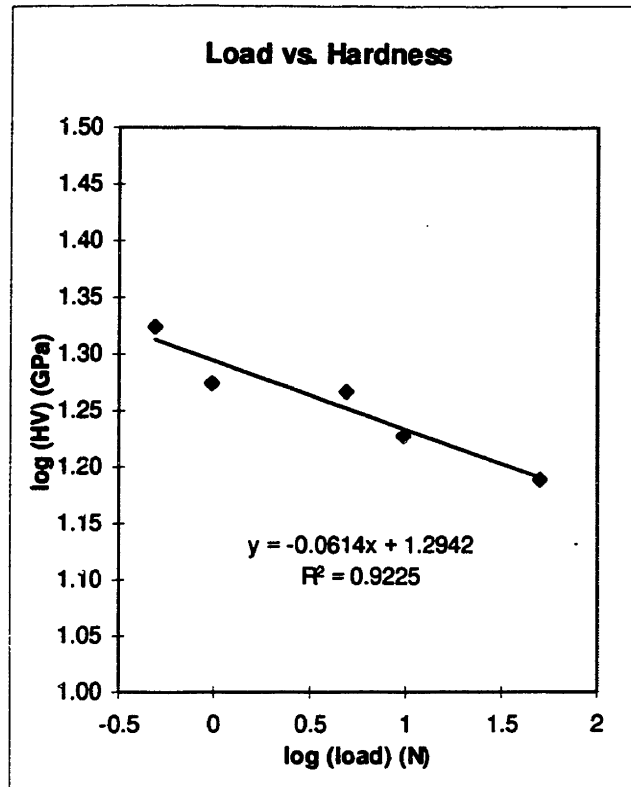
Figure 3.20: log(Load) vs. log(Hardness) plot.
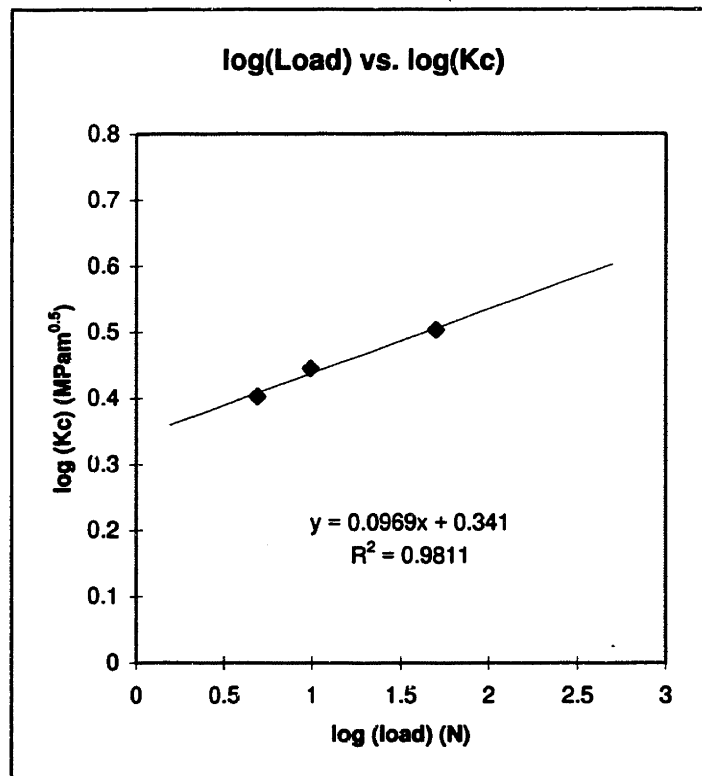
Figure 3.21: log(Load) vs. log(Kc) plot.

3.3.6 DILATOMETRY

Thermal expansion characteristics of the monolithic ZTA bars were measured with a dilatometer (Netzsch, Germany). The heating rate of the furnace was controlled at 1°C per minute. Changes in dimension during the thermal excursion were recorded. Figure 3.22 shows thermal expansion behavior of 3D-printed Al_2O_3, t-ZTA and m-ZTA, and the estimated values of the thermal expansion coefficients are also shown. Experimentally measured values of thermal expansion coefficients are $\alpha_{Al_2O_3}$ = 8.8 × 10^{-6} /°C, $\alpha_{m\text{-}ZTA}$ = 8.4 × 10^{-6} /°C and $\alpha_{t\text{-}ZTA}$ = 9.2 × 10^{-6} /°C. The typical CTE for conventionally prepared ZTA specimens are $\alpha_{m\text{-}ZTA}$ = 8.4 × 10^{-6} /°C and $\alpha_{t\text{-}ZTA}$ = 9.0 × 10^{-6} /°C which is in excellent agreement with those of 3D-printed ZTA specimens. [31] The abrupt change of m-ZTA thermal expansion characteristics in the vicinity of 1000 °C is caused by the phase transformation of ZrO_2 in ZTA. Claussen and Ruhle also reported similar transformation temperatures for ZTA specimens with 15 vol%, 0.6 μm ZrO_2 dispersed in alumina. [34] The phase transformation strain estimated from this change is ε_{tr} = 1.75 × 10^{-3}. It should be noted that the volume expansion of unconstrained ZrO_2 upon phase transformation has been reported to be in the range of 3-5 %.[70] The phase transformation strain calculated from the reported volume expansion would then be in the range of 1.8 ~ 3.0 × 10^{-3} for 18 vol% of ZrO_2 in ZTA. However, the alumina matrix surrounding the zirconia grains imposes a constraint on phase transformation [71], thus causing the volume expansion to be less than this value. The experimentally estimated thermal data was used for the predictions of the thermomechanical responses in 3D printed ZTA multilayer systems in this study.

Thermal expansion of ZTA samples
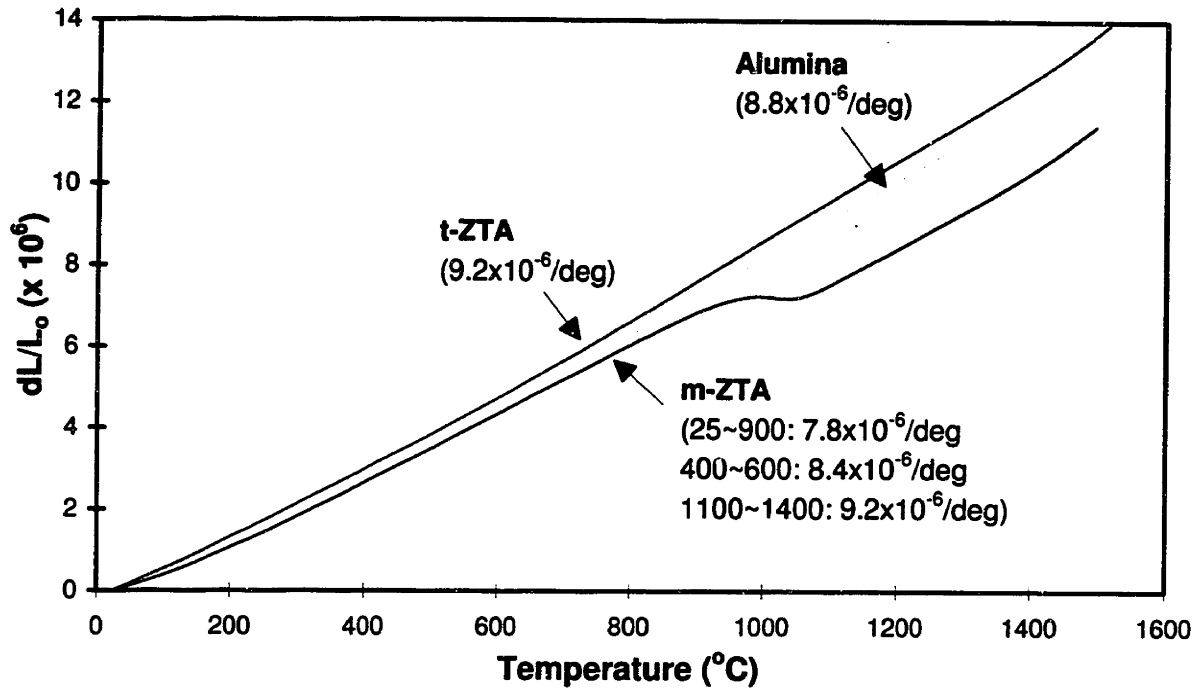
Figure 3.22: Thermal expansion of the monolithic ZTA specimens.

3.4 CONCLUSIONS

The XRD study showed the effectiveness of 3DP in doping ZTA, thereby controlling the phase stability of the ZrO_2 granules. The thermal expansion characteristics of the 3DP-derived m-ZTA and t-ZTA components showed excellent agreement with the properties of conventionally prepared specimens. These demonstrate that one can control the phase distribution of the ZTA components by selectively depositing stabilizer through the 3DP nozzle. The thermal characteristics of the 3D-printed monolithic ZTA parts were used to design the properties of the ZTA components with internal Y_2O_3 gradient. Chapters 4 and 5 discusses the details of the design and fabrication study.

4. ZTA with Y_2O_3 Gradients

Monolithic ZTA specimens were successfully prepared by 3DP, as discussed in Chapter 3. ZTA components that have internal gradients of Y_2O_3 concentration were built by 3DP to investigate the effectiveness of 3DP in controlling microstructure within a component. Different amounts of $Y(NO_3)_3$ salt solution was deposited within a specimen to cause the compositional variation. These selectively doped 3DP samples can be categorized by the nature of the compositional variation. Results on the ZTA samples with sharp compositional gradient are reported in section 4.1. ZTA specimens with gradual change in Y_2O_3 concentration are described in section 4.2. Section 4.3 reports the application of 3DP to introduce surface compression on ZTA specimens.

4.1 SHARP Y_2O_3 GRADIENT

4.1.1 SAMPLE PREPARATION

Figure 4.1 shows a schematic of a ZTA bar that contains abrupt transitions from m-ZTA to t-ZTA and vice versa. The outer walls and end caps were printed with a mixture of Rhoplex HA-16 and yttrium nitrate salt solution. The core region of the bar was left unprinted, and did not contain any binder. The structural integrity of the green body was not affected, however, since the loose powder from the core had no way of escaping from the part. The final part consisted of two distinct regions: a yttrium-depleted core, and yttrium walls which completely encapsulated the interior core. These bars were isostatically pressed and then fired for 3 hours at 1600 °C for densification.

4.1.2 MICROPROBE

Microprobe analysis was conducted across the width of a cross section to map out the yttria concentration within the part. Figure 4.2 shows microprobe measurement of Y_2O_3 concentration across the polished cross section of a ZTA specimen with sharp interfaces. The location of sharp interfaces between the yttrium-rich and yttrium-depleted regions coincided precisely with the boundary between the printed and unprinted regions.

The results from the microprobe analysis provide direct evidence of 3DP's capability to exercise spatial compositional control.
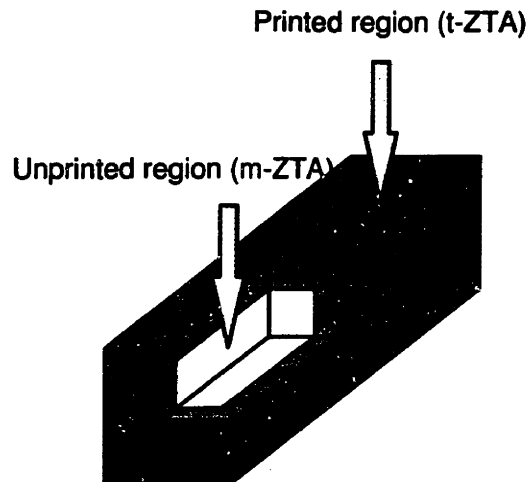
Figure 4.1: Schematic of a ZTA bar with abrupt interfaces
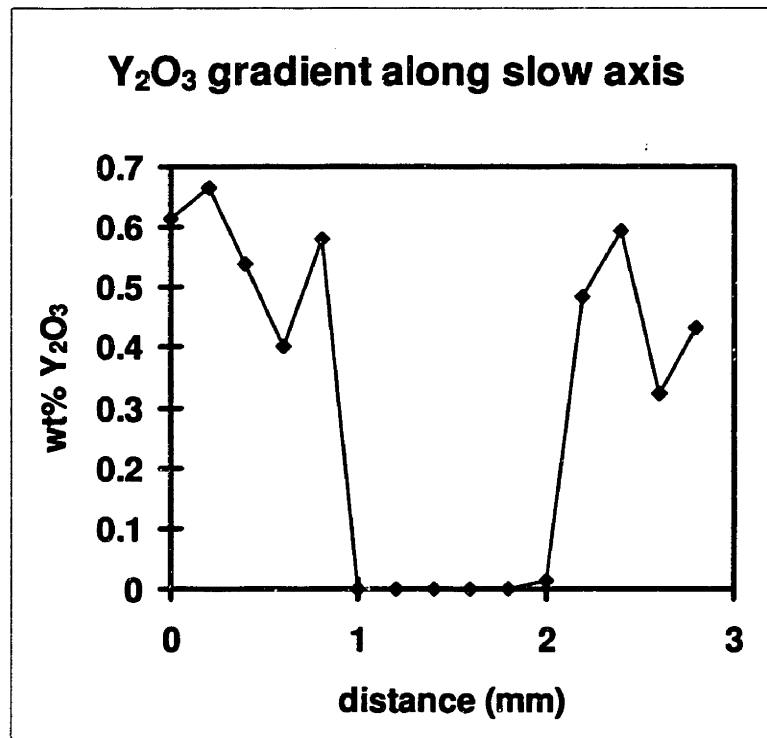
Figure 4.2: Y_2O_3 concentration along the width of a ZTA component

4.1.3 X-RAY DIFFRACTION

X-ray diffraction (XRD) patterns were obtained from slices of these samples as illustrated in Figure 4.3. Surfaces of these slices were polished prior to obtaining diffraction patterns. Proportions of $m-ZrO_2$ and $t-ZrO_2$ were calculated by taking the ratio of the areas under major peaks corresponding to each phase, as described earlier in Chapter 3.[67] Results of XRD studies on this specimen also confirm the effectiveness of the compositional variation in controlling the phase gradient of the zirconia. Figure 4.4 shows a series of diffraction patterns from these slices. Slices 1 and 5, taken from the yttrium-rich portion of the specimen, show one major peak that corresponds to tetragonal (111). Slices 2, 3, and 4, by contrast, show the emergence of two other peaks that indicate the presence of monoclinic zirconia. Relative volume fractions of the two phases were calculated using the diffraction patterns. Figure 4.5 shows that the calculated fraction of monoclinic zirconia phase is in good agreement with the expected amount.
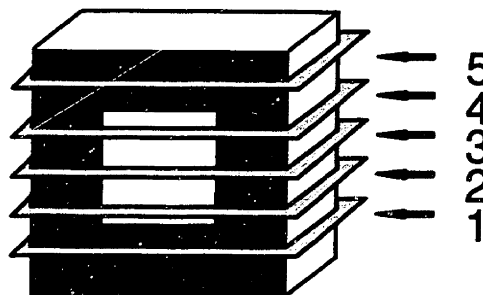
Figure 4.3: Schematic of the sliced samples for X-ray diffraction
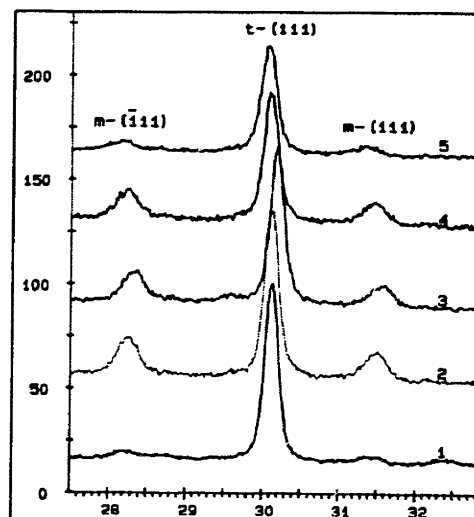
Figure 4.4: X-ray diffraction patterns from slices of the ZTA sample.
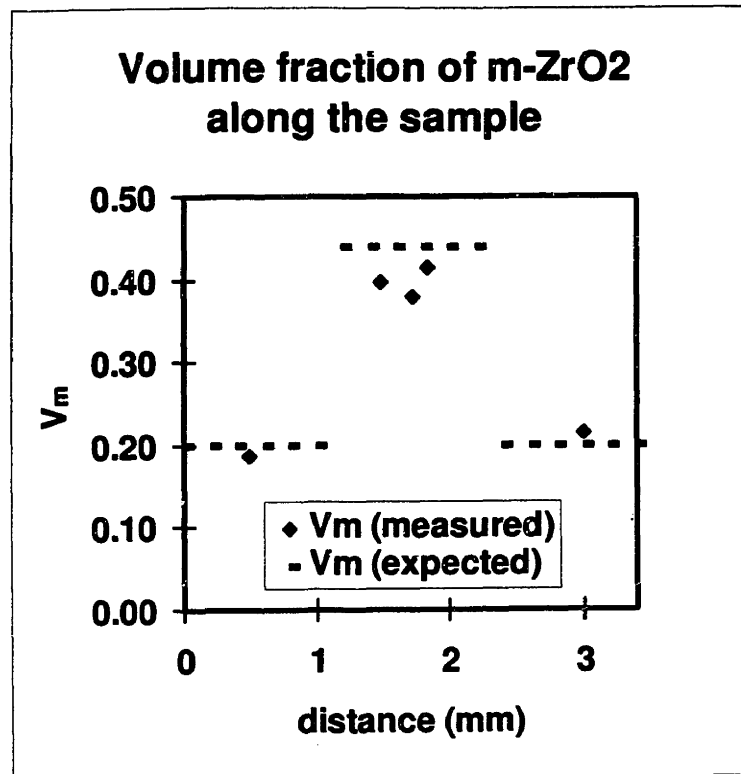
Figure 4.5: Relative proportion of m-ZTA from X-ray diffraction patterns.
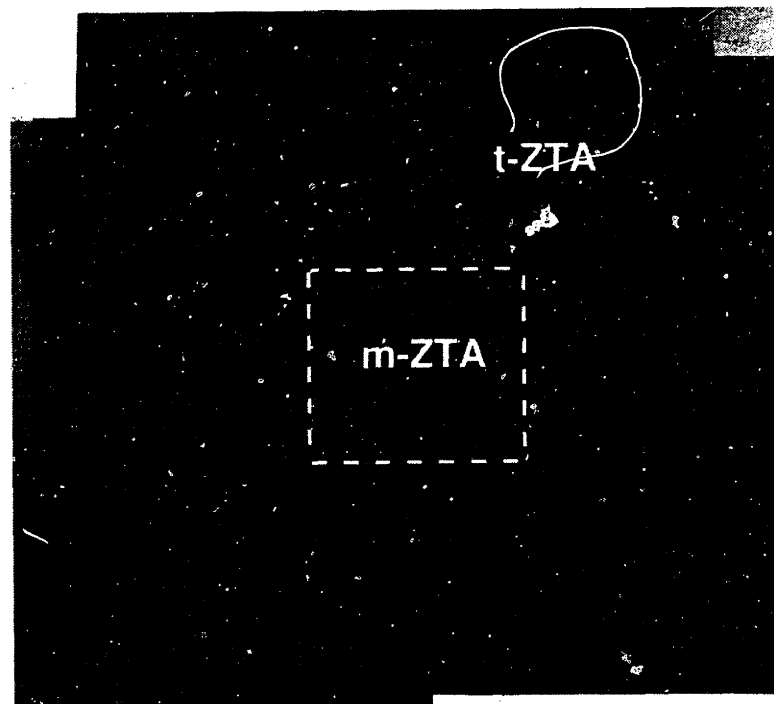
Figure 4.6: Optical micrograph of a ZTA sample with abrupt interfaces

4.1.4 MICROSTRUCTURE

An examination of the microstructure also points to the presence of sharp interfaces while the microprobe and XRD results give us direct evidence of compositional control through 3DP. These samples were designed to develop tensile stress in the outer surface and compressive stress in the core. A polished cross section of this sample in Figure 4.6 reveals cracks propagating through the sample at different directions. A lateral crack initiates and propagates along where a sharp interface between m-ZTA and t-ZTA exists. Another crack initiated from the bottom surface is arrested in the middle of the sample where compressive residual stresses are present. These observations clearly indicate that the 3DP method can be used to effectively control compositions within components, and that components with tailored residual stress profiles can be designed and built by 3DP.

4.2 ZTA WITH FUNCTIONALLY GRADED STRUCTURE

4.2.1 BACKGROUND

Functionally graded materials (FGM) comprise multilayers within which the composition, microstructure and/or properties vary spatially.[28,72-74] Examples of FGM include graded layers for ceramic-metal joints, thermal-barrier coatings for high temperature applications, wear-resistant coatings, and structural components with engineered pores for weight reduction. Microstructure and localized property control is crucial in the performance of FGM components. The FGM concept is used to customize materials to meet complex performance criteria rather than being confined by the selection of available materials and their inherent characteristics.

Compositionally graded layers of ZTA were prepared by 3DP in this study. The relative fraction of monoclinic and tetragonal ZrO_2 was varied through the thickness of a multilayer plate. Analytical solutions for residual stress and curvature development in a transformation toughened ceramic multilayers were developed by Cho and Suresh [29]. These solutions were used to predict the curvature development in ZTA multilayers with asymmetric structure. Residual stress profile for multilayer structures, both symmetric

and asymmetric, may be designed by changing the composition and geometry of the multilayer specimens. The following sections discuss the development of the analytical solution and the experimental results from the 3D-printed ZTA multilayers.
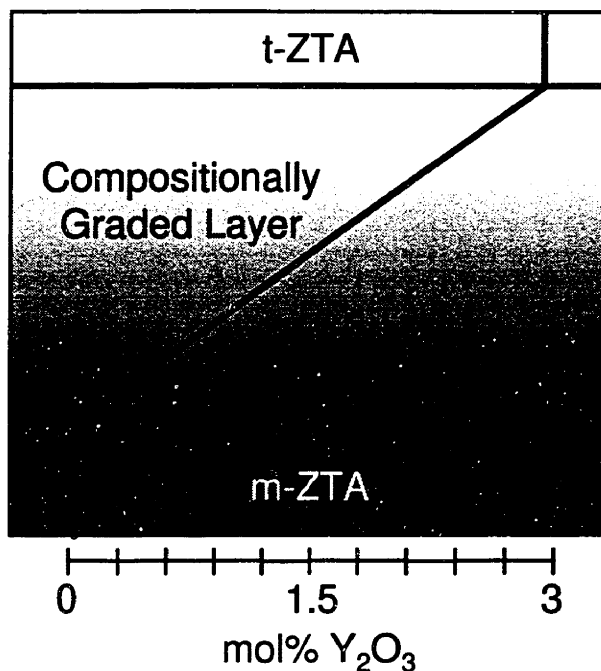
Figure 4.7: Schematic of the ZTA multilayer plate.

4.2.2 SAMPLE FABRICATION

Two nozzles were used to build ZTA parts with a gradient in yttria. One nozzle was dedicated to printing the acrylic dispersion while the other was used to deposit the yttrium nitrate salt solution. The printhead assembly was designed to accommodate frequent exchange between the two. The amount of yttria in each of the layers was controlled by adjusting numerous print parameters. These parameters include printhead speed, line spacing, and the number of yttrium salt deposition passes per layer. Other parameters, such as binder concentration and layer thickness, can also be used to change the yttria content at specific layers. The latter parameters were, however, kept constant to simplify the printing operation. Thin ZTA plates (14 sub-layers, each 150 μm thick in the green stage) with a gradual compositional change across an interlayer zone (comprising 9 sub-layers), from fully monoclinic phase on one surface (containing 3 sub-layers) to a fully tetragonal phase on the other (containing 2 sub-layers), were created by depositing different amounts of yttrium nitrate salt on each layer. Combinations of print parameters

were used to control the doping level of the salt as discussed in section 2.5. Details of the parameters used for each layer is summarized in Table 4.1. Figure 4.7 shows the designed gradient of the phases through the thickness of the plate. The plates were then WIPed at 275 MPa in 80°C oil, and fired at 1550°C for 3 hours to achieve densification. The dimensions of the sintered plate were 22.5 × 22.5 × 0.85 mm.

Table 4.1: Print parameters used to build compositionally graded ZTA plate.

Composition (% m-ZTA)	Printhead speed (m/sec)	Line spacing (μm)	Number of depositions per layer
0	1.05	150	2
10	1.20	150	2
20	1.35	150	2
30	1.50	150	2
40	1.50	175	2
50	1.05	150	1
60	1.35	150	1
70	1.50	175	1
80	1.50	250	1
90	1.50	200	1
100	1.50	150	1

*Flow rate was kept at 1.2 cc/min, salt concentration was kept at 0.115 M.

4.2.3 MICROSTRUCTURE

Lamination defects that resulted from excess binder film formation between each printed layers were observed in the early stages of this study [20,27]. An additional isostatic pressing step *after* binder burnout has proven to heal any laminar defects stemming from excess binder. Figure 4.8 shows a typical microstructure of the ZTA multilayer system fabricated using 3DP method. The zirconia grains are quite uniformly dispersed in alumina. Stereographic analyses on micrographs revealed that the area fraction of ZrO$_2$ is about 18% [75]. The average grain size of Al$_2$O$_3$ matrix and average particle size of dispersed ZrO$_2$ were measured to be about 1 μm and 0.5 μm, respectively. Pullouts were

observed when polishing specimens that were sintered at a higher temperature (1600 °C). Pullouts were predominantly populated near the m-ZTA side, which is consistent with the observation of Green [76] that microcracks around large monoclinic ZrO_2 grains cause pullouts. Similar problems were observed when specimens were held at 1550°C for a prolonged period, thereby confirming the relationship between grain size and the extent of microcracking.
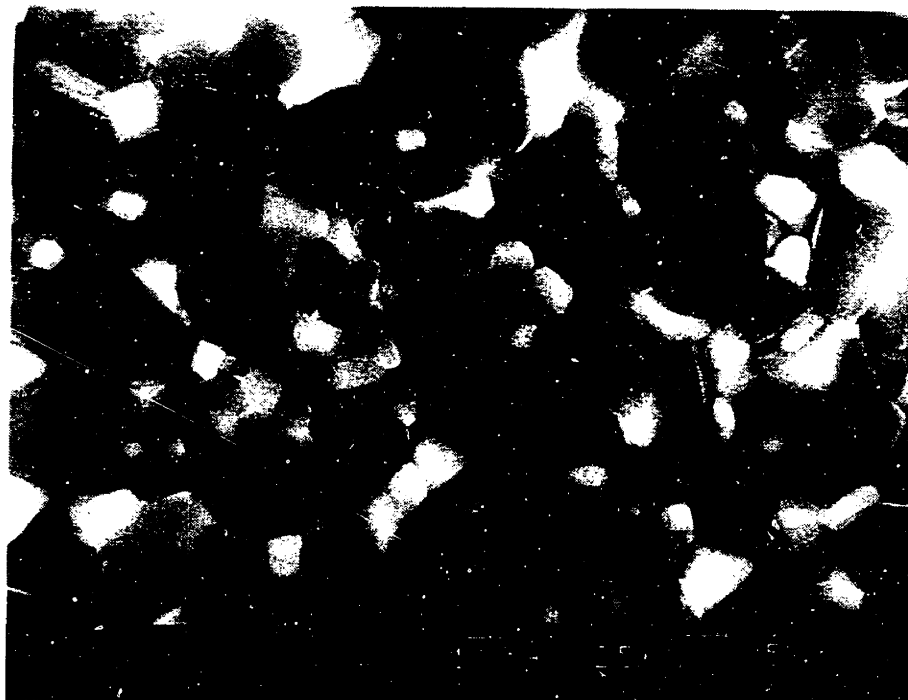
Figure 4.8: SEM micrograph from polished cross section of a graded multilayer.

4.2.4 X-RAY DIFFRACTION

An XRD pattern from the surface of the densified specimen was collected, and then approximately 100 μm of material beneath the surface was ground and polished to reveal the next layer which had a different amount of yttria. Repeated grinding and X-ray diffraction revealed the effectiveness of the printing parameters in obtaining the desired gradient in tetragonal and monoclinic phases. The volume of constituent phases of the 3D-printed ZTA graded layers were characterized using the XRD method. Figure 4.9 shows diffraction patterns taken from various locations through the thickness of the plate. The intensity of the peaks corresponding to tetragonal ZrO_2 increases gradually from one end to the other of the sample, while the intensity of the monoclinic peaks decreases correspondingly. Figure 4.10 shows the fraction of monoclinic phase versus position. A

linear variation of monoclinic ZrO$_2$ along the thickness illustrates successful fabrication of the compositionally-graded ZTA multilayer employing the 3DP technique. Deviation from linearity near the m-ZTA surface may be explained by the presence of very fine ZrO$_2$ particles that are not large enough to transform [31]. On the other hand, there are some monoclinic zirconia particles at the tetragonal end most likely due to the grinding-induced transformation.

2 Theta
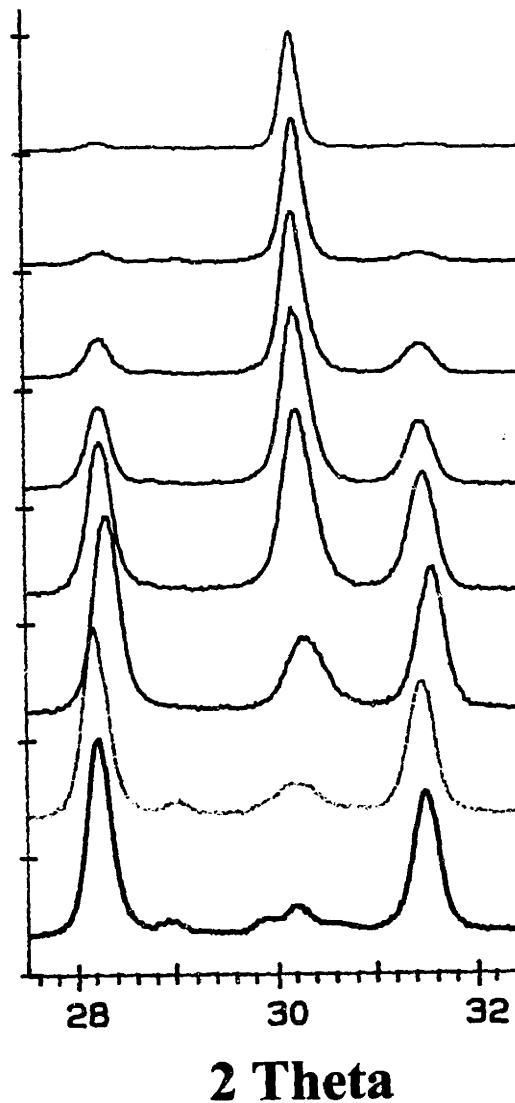
Figure 4.9: X-ray diffraction pattern taken from various locations in thickness of a multilayer plate

**Volume fraction of m-ZrO₂ as
a function of position**
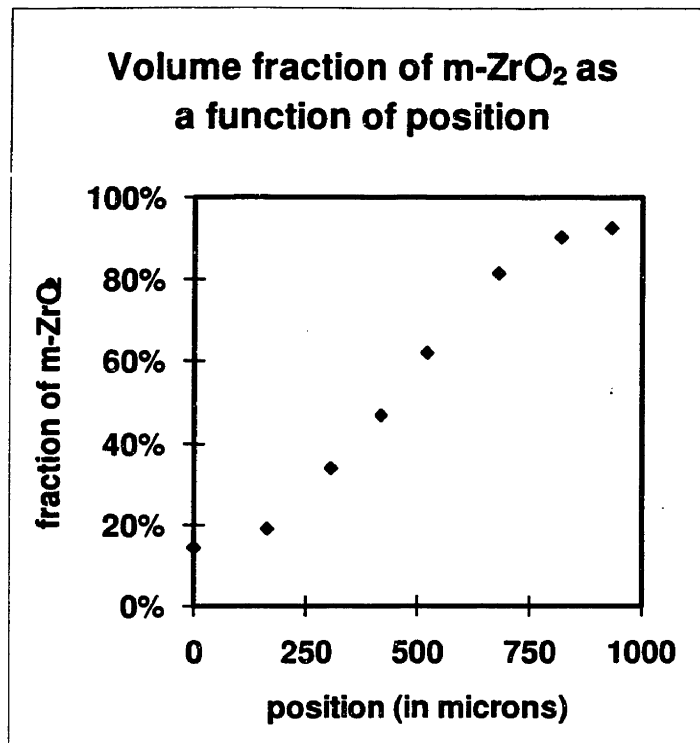
Figure 4.10: Calculated proportion of monoclinic zirconia content through the thickness.

4.2.5 CURVATURE DEVELOPMENT AND STRESS ANALYSIS

Thermal deformation of the curvature evolution of ZTA multilayer plate was measured with a laser-based digital measurement device (Point Range Sensor, CyberOptics, Fremont, CA). The Point Range Sensor generates a point of laser light and projects the point onto the surface to be measured. The scattered light from the surface is collected on a digital sensor. The location of the laser spot on the sensor is used to determine the height changes in the surface. The internal stress distribution developed within the compositionally graded ZTA multilayers during thermal excursions was calculated using the analytical model proposed by Cho and Suresh. [29]

4.2.6 ANALYTICAL SOLUTION FOR STRESS AND CURVATURE

Thin multilayer plates developed a curvature upon cooling from the sintering temperature, as expected. The measured curvature from laser range finder was 6.4/m. Incompatibilities arise from two major sources: the mismatch in thermal expansion coefficients and the difference in ZrO₂ phase transformation strain between layers, since the 3D-printed ZTA system comprises multilayers. Thermomechanical strains develop in

103

the ZTA multilayer system during thermal excursions, as pointed out by Cho and Suresh[29]. All of the zirconia grains in the ZTA multilayer plate should be in tetragonal phase at the sintering temperature, regardless of the compositional variation. Portions of the multilayer plate transform into monoclinic phase as the specimen is cooled down from the sintering temperature. The transformation strain and thermal coefficient mismatch start to develop curvature and strain through the thickness of the plate during the cool down step. Figure 4.11 illustrates the evolution of the constituent layers, m-ZTA, GL, and t-ZTA, upon cooling from the sintering temperature.
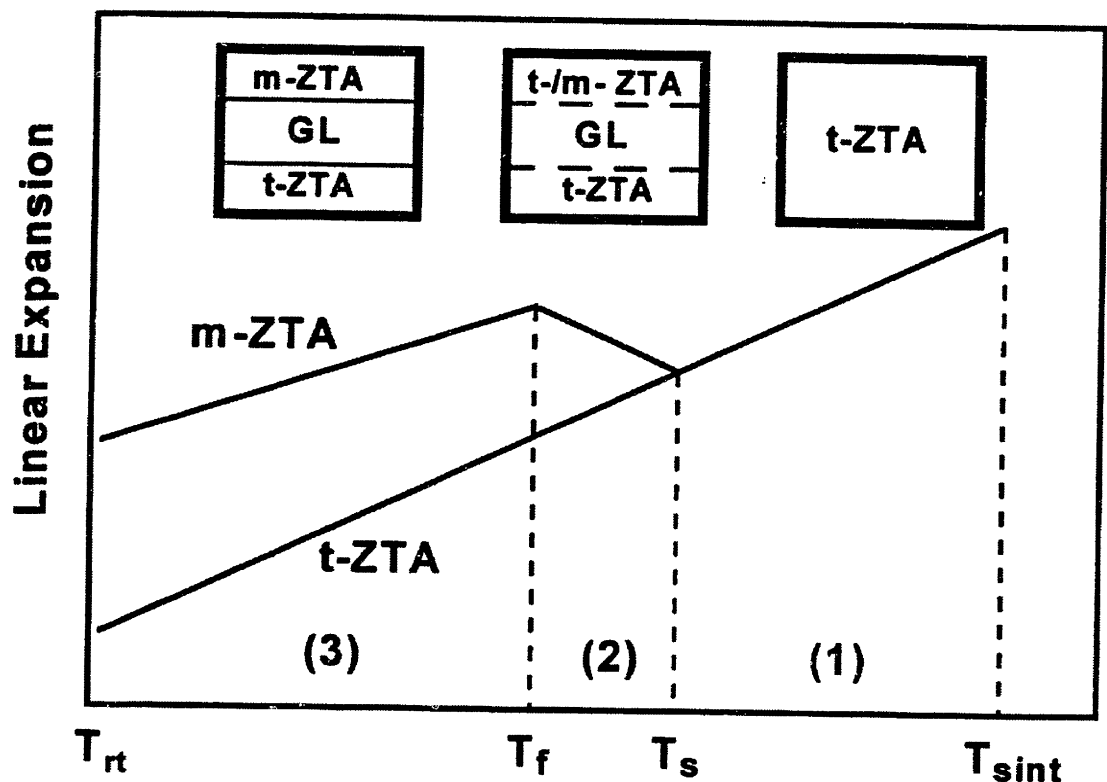
Figure 4.11: Schematic diagram of the linear expansion of the ZTA developing a multilayer structure during cooling from the sintering temperature.

The classical plate theory for small deformation was used to analyze the stress and curvature development in the ZTA multilayers [77]. The in-plane normal strains, ε (= $\varepsilon_{xx} = \varepsilon_{yy}$), are given by

$$\varepsilon(z) = \varepsilon_0 + \kappa z \qquad (4.1)$$

where ε_0 is the normal strain at $z = 0$ and κ is the curvature of the plate. The stress distribution within the sample, $\sigma(z)$ $(= \sigma_{xx}(z) = \sigma_{yy}(z))$ is

$$\sigma(z) = E^*[\varepsilon_0 + \kappa z - \alpha(z)\Delta T + \varepsilon_{tr}(z)] \qquad (4.2)$$

where $E^* = E/(1- \nu)$, and α, ΔT, ν, and ε_{tr} are the thermal expansion coefficient, the temperature change, the Poisson's ratio, and the phase transformation strain, respectively. Invoking the force and momentum balance at static equilibrium,

$$\int_z \sigma(z)dz = 0, \qquad \int_z z\,\sigma(z)dz = 0 \qquad (4.3)$$

Equations (4.1)~(4.3) can be combined to obtain the solutions for ε_0 and κ. Stress distribution through the thickness of the multilayer structure can be calculated with (4.2) once ε_0 and κ are calculated. Detailed derivation for the solution can be found in Cho and Suresh's work [29]. The results for curvature and stress at room temperature are:

$$\kappa = A\frac{g_2}{H} \qquad (4.4)$$

$$\sigma(z) = E^*AG \qquad (4.5)$$

where incompatibility term A is given by

$$A = \varepsilon_{tr} + (\alpha_{m\text{-}ZTA} - \alpha_{t\text{-}ZTA})\Delta T. \qquad (4.6)$$

H is the total thickness of ZTA multilayer plate and h's are the thicknesses of the t-ZTA, m-ZTA and graded layers (GL) as shown in Figure 4.12.
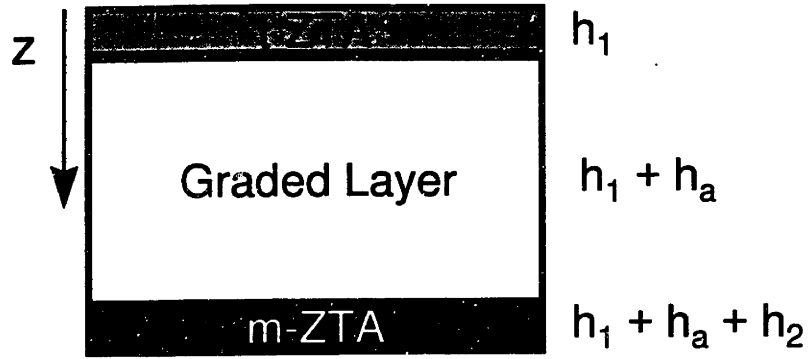
Figure 4.12: Schematic of an asymmetric ZTA multilayers.

The geometrical functions in each layer are defined by

$$G = g_1 + g_2 \frac{z}{H} \qquad\qquad \text{(t-ZTA)} \qquad (4.7)$$

$$G = g_1 + (g_2 - \rho_{GL}^{-1})\frac{z}{H} + \rho_{GL}^{-1} \rho_{t\text{-ZTA}} \qquad\qquad \text{(GL)} \qquad (4.8)$$

$$G = g_1 + g_2\frac{z}{H} - 1 \qquad\qquad \text{(m-ZTA)} \qquad (4.9)$$

where

$$g_1 = \rho_{m\text{-ZTA}}^2 - 2\,\rho_{t\text{-ZTA}}\,\rho_{m\text{-ZTA}} - \rho_{t\text{-ZTA}}\,\rho_{GL} \qquad\qquad (4.10)$$

$$g_2 = \rho_{GL}^2 + 6\,\rho_{t\text{-ZTA}}\,\rho_{m\text{-ZTA}} + 3\,\rho_{t\text{-ZTA}}\,\rho_{GL} + 3\,\rho_{m\text{-ZTA}}\,\rho_{GL} \qquad\qquad (4.11)$$

$$H = h_{t\text{-ZTA}} + h_{m\text{-ZTA}} + h_{GL} \qquad\qquad (4.12)$$

$$\rho_{\text{t-ZTA}} = \frac{h_{t-ZTA}}{H}, \quad \rho_{\text{m-ZTA}} = \frac{h_{m-ZTA}}{H}, \quad \rho_{\text{GL}} = \frac{h_{FGM}}{H} \qquad (4.13)$$

No evolution of curvature and internal stress within the ZTA multilayer plate is expected above the phase transformation starting temperature (stress-free state), since the entire ZTA plate should be homogeneous t-ZTA.

X-ray and neutron diffraction methods are commonly used to measure residual stress fields. Both measurements are, however, confined to the near surface region only. One of the purposes of present study on compositionally graded ZTA multilayers is in the analysis of thermomechanical response during processing and service conditions, and, thus, provide information for optimizing ZTA multilayer structural design. The variation of thermal stresses generated by the mismatch in thermal expansion coefficients and by the phase transformation strain, along the thickness of compositionally multilayer materials, causes the multilayer plates to develop curvature and non-uniform internal residual stress distribution during thermal excursions. Consequently, one possible way of predicting internal stresses within compositionally graded systems involves accurate experimental measurements of curvature changes during thermal loading and the inference of the magnitude of the internal residual stress field from the measured curvature change.

Curvature development in the ZTA multilayer plate was predicted by using experimentally determined values of thermal expansion coefficients and phase transformation strain from the 3D-printed monolithic ZTA components: α_{m-ZTA} = 8.4 × 10^{-6} /°C, α_{t-ZTA} = 9.2 × 10^{-6} /°C, and ε_{tr} = 1.75 × 10^{-3}. The ZTA multilayer is composed of two t-ZTA, three m-ZTA, and nine middle sub-layers in which a linear gradation occur (i.e. a total of 14 sub-layers). The thickness ratios of t-ZTA, m-ZTA and GL are given by $\rho_{\text{t-ZTA}}$ = 0.15, $\rho_{\text{m-ZTA}}$ = 0.20 and ρ_{GL} = 0.65. The total thickness of the ZTA multilayer plate was measured as 0.85 mm. Using the equations (4.4) and (4.6)-(4.13), the curvature was calculated as 3.81 m^{-1}. Figure 4.13 shows the comparison of the measured and calculated curvatures developed in the ZTA multilayer plate upon cooling from the

sintering temperature.* A zirconia volume expansion of 3-5 % upon transformation can be assumed when the constraint effect in Al_2O_3 matrix is not taken into account. The expected curvatures are in the range of 3.9-5.7 m^{-1}, as shown in Figure 4.13 as shaded area. The measured and calculated curvatures are in reasonably good agreement.

Curvature Development in ZTA Multilayers
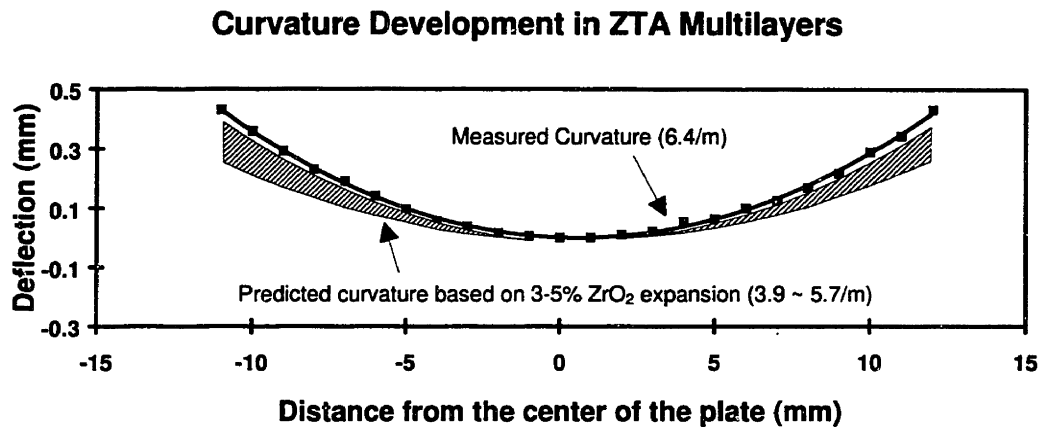
Figure 4.13: Calculated and measured curvatures in multilayer plates

The internal stress distribution within the ZTA multilayer was calculated using equations (4.5)-(4.13). The Young's modulus (E) and Poisson's ratio (ν) used in the calculations are 300 GPa and 0.25, respectively, and the thickness ratios are, ($\rho_{t\text{-ZTA}}$, $\rho_{m\text{-}ZTA}$, ρ_{GL}) = (0.15, 0.20, 0.65). Again, the experimentally measured values of thermal expansion coefficients and phase transformation strain were used for the calculation of internal stresses. Figure 4.14 illustrates the predicted stress distribution within ZTA multilayers. The distribution of internal stresses varies linearly with thickness within each of the three constituent layers. The curvature evolution in the three layer zone ZTA

---

* Note that the existence of discrete sub-layers, rather than a smooth variation in composition, in the graded region causes jumps in stresses at the sub-layer interfaces. This fluctuation in stress decreases with increasing numbers of sub-layers. The difference in curvature evolution, however, between the discrete sub-layer case and the smooth graded interlayer case is known to be insignificant.[78]

plate allows stress relaxation and, thus, the resultant linear variations of the internal stresses were developed within the m-ZTA and t-ZTA layers.

Stress, σ(z) (MPa)
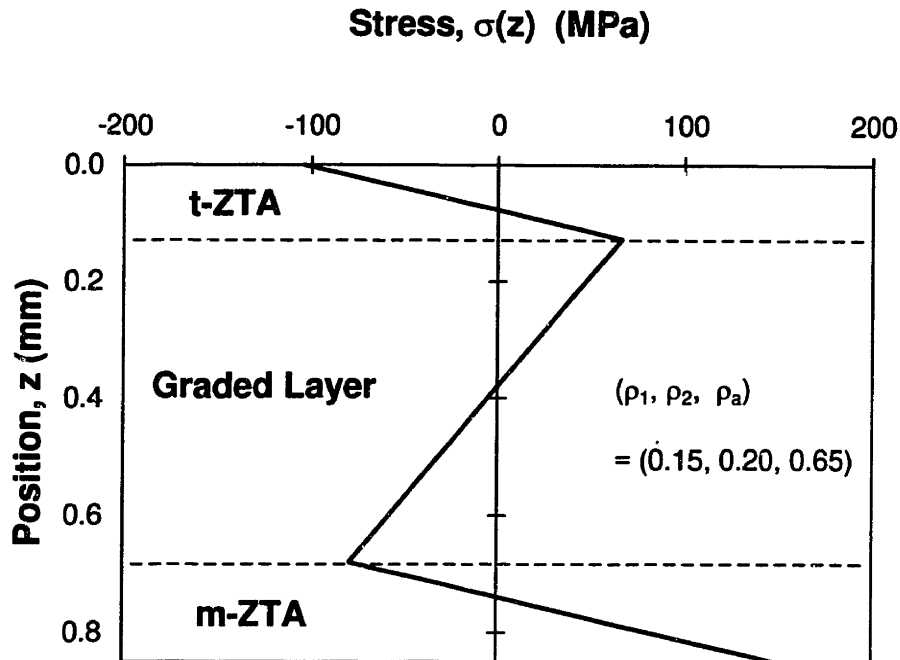
Figure 4.14: Calculated stress distribution within the multilayers at room temperature

It is interesting to note that surface cracks can be initiated on the m-ZTA surface due to the tensile surface stress. The first set of 3D-printed ZTA plates exhibited microcracks on the monoclinic surface and extensive pullout occurred upon grinding and polishing, as shown on Figure 4.15. *No microcracks were evident around the t-ZTA portion of the plate.* It is important to recognize that the outer surface of the m-ZTA layer is *not* under compression. This is a consequence of the alteration in stress distribution with relaxation mechanisms such as curvature evolution. Figure 4.16 is taken from the surface of a monolithic m-ZTA specimen with the same sintering schedule as the ZTA multilayer shown in Figure 4.15. The extent of microcracking and pullouts is significantly less in the monolithic specimen. This also suggests that the extensive pullouts on the m-ZTA portion of the multilayer structure is, indeed, accentuated by the presence of the residual tensile stress.
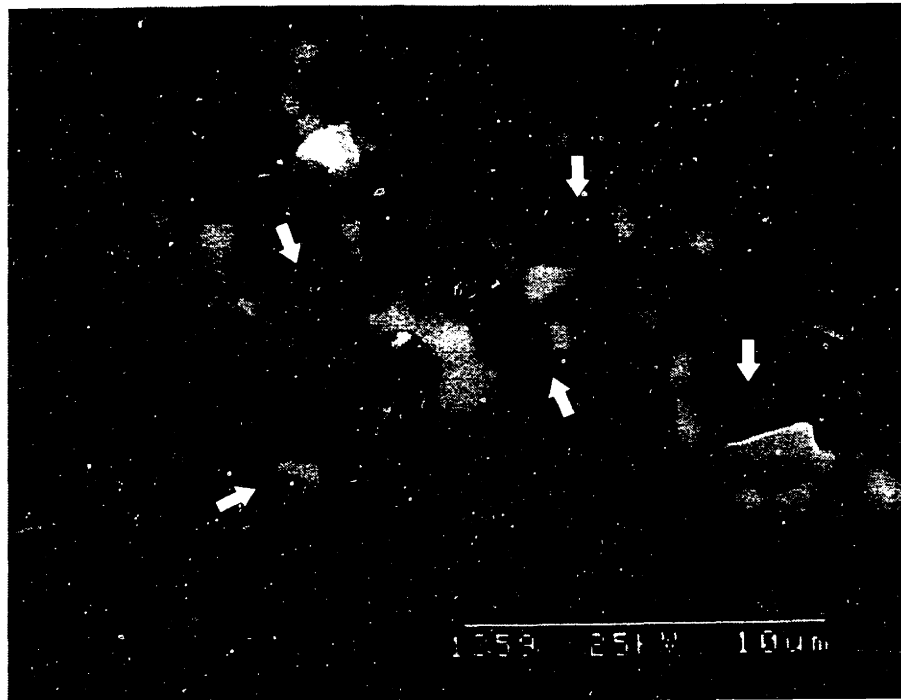
Figure 4.15: Microstructure of a ZTA multilayer plate near monoclinic side
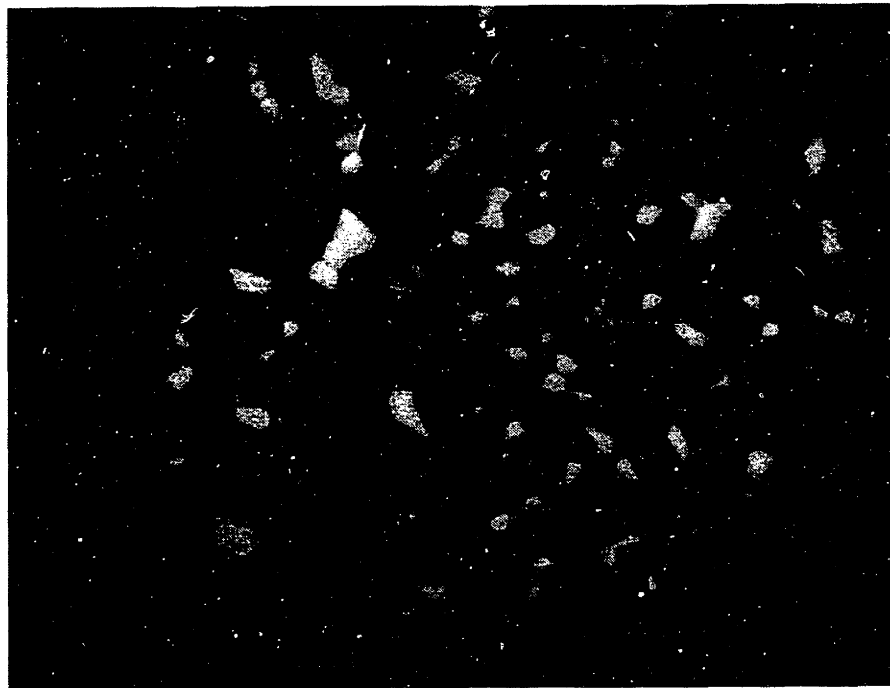
Figure 4.16: Microstructure of a monolithic m-ZTA specimen. The extent of pullouts is much less than that of the multilayers.

4.2.7 EFFECTS OF LAYER THICKNESS AND COMPOSITION

Two aspects of ZTA multilayer structure were examined in an attempt to illustrate the evolution of internal stresses and to discuss the effects of the ZTA: (i) composition and (ii) the thickness of the zones. First, the symmetric five-zone structure is considered, as illustrated in Figure 4.17. This multilayer consists of two compositionally graded layer zones (GL) sandwiched between the middle t-ZTA zone and the two m-ZTA outer layer zones. It is not always necessary to have the surface layer to be fully monoclinic while it is desirable to have a high monoclinic zirconia content in the outer zones to achieve high compressive stresses on the surface. The outer zones can be designed to be a mixture of m-ZTA and t-ZTA, and the magnitude of tensile stresses in the core can be reduced at the expense of the reduction in compressive stresses at the surface. The geometrical aspect is considered next with various combinations of the thickness ratios of zones, ($\rho_{t\text{-ZTA}}$, $\rho_{m\text{-ZTA}}$, ρ_{GL}). Only one half of the symmetric five zone system needs to be considered.
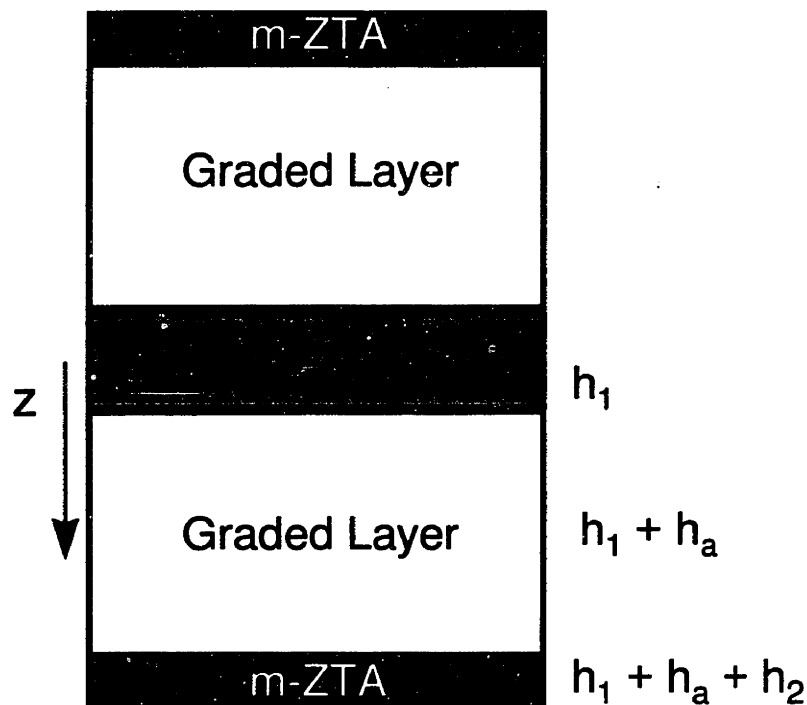
Figure 4.17: Schematic of a symmetric five zone structure comprising t-ZTA, m-ZTA, and Graded Layer zones.

Distribution of the internal stresses within the symmetric five-layer ZTA can be evaluated using the equations (4.2) and (4.10) with different geometrical functions given by

$$G^s = g_1^s \qquad \text{(t-ZTA)} \qquad (4.11)$$

$$G^s = g_1^s - \rho_{GL}^{-1} \frac{z}{H} + \rho_{GL}^{-1} \rho_{t\text{-ZTA}} \qquad \text{(GL)} \qquad (4.12)$$

$$G^s = g_1^s - 1 \qquad \text{(m-ZTA or m-ZTA/t-ZTA)} \qquad (4.13)$$

and

$$g_1^s = \rho_{m\text{-ZTA}} + \frac{1}{2} \rho_{GL} \qquad (4.14)$$

The phase transformation strain ε_{tr} in equation (4.3) is replaced by $f_{m\text{-ZTA}}\varepsilon_{tr}$, where $f_{m\text{-ZTA}}$ is the volume fraction of monoclinic ZrO_2 in outer m-ZTA/t-ZTA layers. The superscript 's' denotes that the structure is symmetric. A biaxial stress state is considered in the following internal stress analyses.

First, the internal stress distributions are predicted with different compositions of the characteristic zones in ZTA systems. Two different compositions of outer ZTA zones(m-ZTA/t-ZTA) are considered, i.e., outer zones containing fully monoclinic ZrO_2 phase (m-ZTA) and outer zones containing mixture of 50 % monoclinic and 50 % tetragonal ZrO_2 phases (m-ZTA + t-ZTA). The compositions of GL zones are assumed to vary linearly between those of middle t-ZTA and outer m-ZTA/t-ZTA zones accordingly. Figure 4.16 illustrates the predicted internal stress distribution of the symmetric five-zone ZTA systems with different compositions of the constituent zones. Thickness ratios of the zones are ($\rho_{t\text{-ZTA}}$, $\rho_{m\text{-ZTA/t-ZTA}}$, ρ_{GL}) = (0.1, 0.1, 0.8). The internal stresses within these

two zones can be adjusted by changing the compositions for the same thickness ratio of t-ZTA and m-ZTA/t-ZTA zones. For example, if the composition of outer zones is changed from ZTA containing full monoclinic ZrO$_2$ to ZTA containing half monoclinic and half tetragonal ZrO$_2$ phases, the magnitude of internal stresses within both of middle t-ZTA zone and outer m-ZTA/t-ZTA zones can be reduced as shown in Figure 4.18. The volume fraction of m-ZTA ($f_{m\text{-}ZTA}$) is reduced with less amount of ZrO$_2$ phase transformation in the later case and the internal stresses are reduced within ZTA multilayers as can be seen in this figure. Possible failure due to high internal stresses at particular locations can be avoided by adjustment of the internal stress distributions within ZTA multilayers.
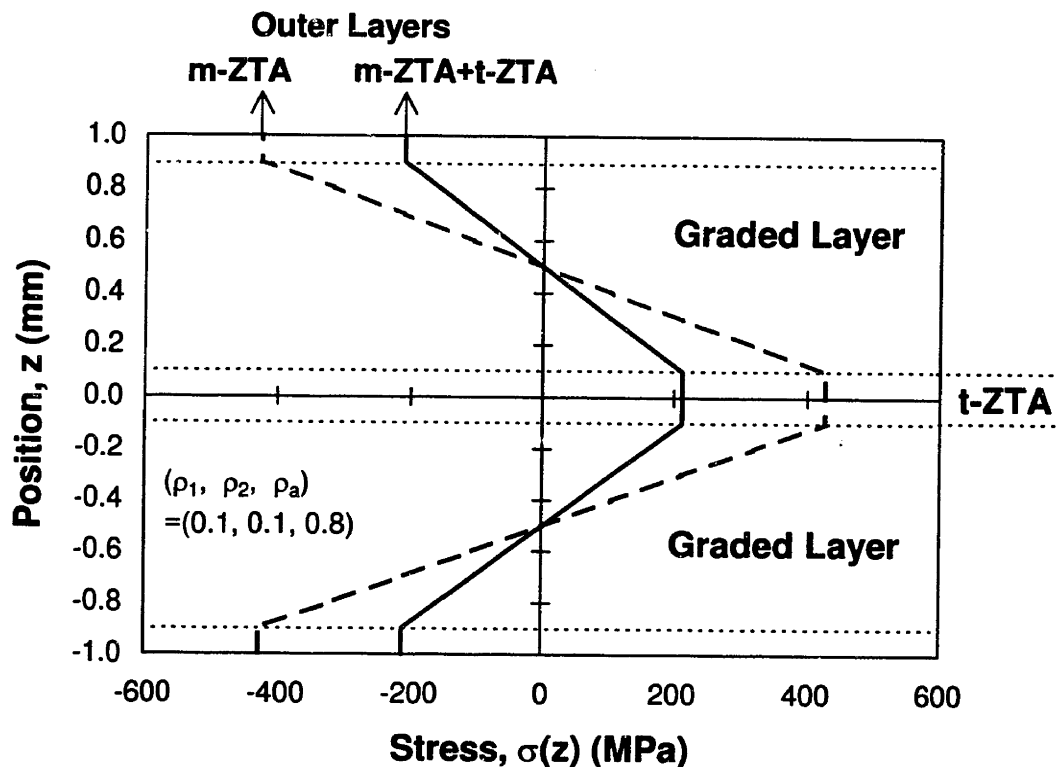
Figure 4.18: Internal stress distribution within symmetric five-zone ZTA plates with different proportions of monoclinic zirconia in outer zones.

The thickness ratios of the characteristic zones can also be varied to achieve desired residual stress profile. Figure 4.19 shows the predicted distributions of internal stresses of symmetric five-zone ZTA systems for different geometries of the constituent zones. The constituent compositions of the ZTA system considered are t-ZTA in the

middle zone, 50% m-ZTA + 50% t-ZTA in outer zones, and two graded zones serving as interfaces. Two different thickness ratios of the zones are considered: i.e., (ρ_{t-ZTA}, $\rho_{m-ZTA/t-ZTA}$, ρ_{GL}) equal to (0.1, 0.1, 0.8) and (0.05, 0.35, 0.60). The tensile internal stress within middle t-ZTA zone can be reduced and the higher surface compressive stress in outer zone can be obtained by reducing the thickness of the outer surface zones, as shown in Figure 4.19. Other parameters such as the gradient profile in FGM layers, for example, can also be used to adjust internal stress distribution in ZTA multilayers [78]. The distribution of internal stresses within asymmetric ZTA multilayers analyzed in Figure 4.13 also can be adjusted by the same methods as it is discussed for symmetric five-zone ZTA systems. The internal stress distribution can be adjusted by changing geometries (ρ's) and by varying controlling the amount of the monoclinic ZrO$_2$ volume fraction, thereby changing the effective phase transformation strain (ε_{tr}).
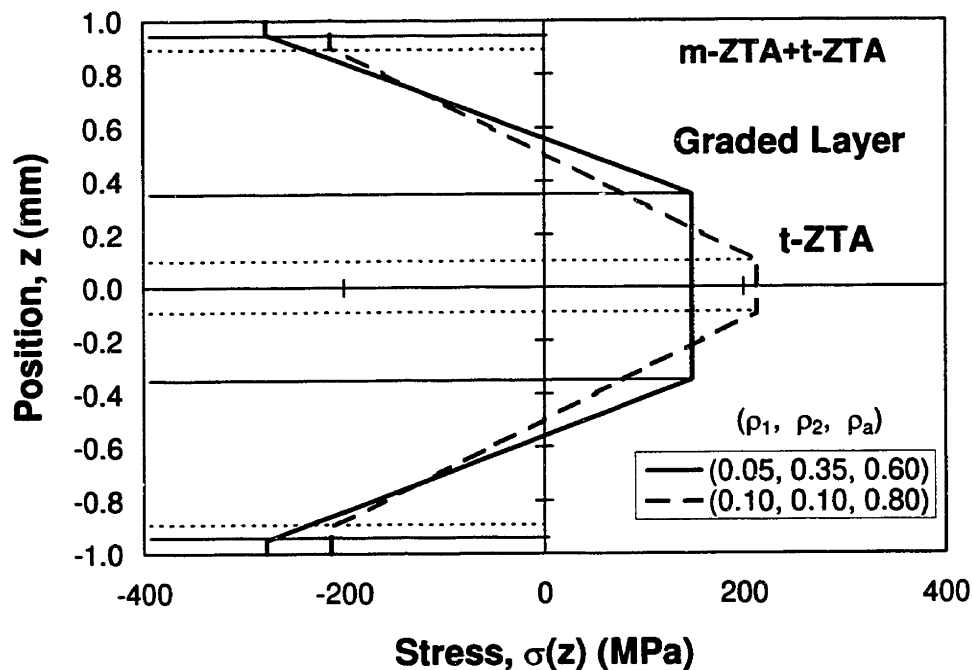
Figure 4.19: Internal stress distribution within symmetric five-zone ZTA plate with different geometrical combinations

4.3 ZTA WITH SURFACE COMPRESSION

4.3.1 PROPERTY DESIGN

Various surface modification techniques have been developed to introduce compressive surface layers to enhance flexural strength and contact damage resistance in zirconia-containing ceramics [58,61-64]. Virkar et al. prepared trilayered composite structure by dry pressing, as described in Chapter 3 [62]. Virkar et al. used simple force balance equations to calculate the residual stress within a trilayered composite. Analytical solutions developed by Cho and Suresh can also be used to calculate the stress distribution in a trilayered structure [29]. The stress solution for a symmetric five layer structure in equation (4.5) reduces to that of a trilayered composite by substituting zeroes for the thickness of the graded layers in equation (4.13). The residual stress profile can be designed by manipulating the thickness ratio of the m-ZTA and t-ZTA zones just as described in section 4.2.7.

4.3.2 EXPERIMENTAL PROCEDURE

Sample Preparation

The first set of trilayered (m-ZTA/t-ZTA/m-ZTA) structure was prepared by printing 15 vol% Acrysol and $Y(NO_3)_3$ solution into spray-dried ZTA granules. Counter-rotation technique was used to spread powder layers. This condition corresponds to the first method described in Figure 3.8 and Table 3.2. Eight jets, four allocated to each liquid, were used simultaneously to construct this set of specimens. Yttrium nitrate salt solution was deposited on the first pass of the printing cycle, followed by an intermediate drying step. Acrysol was then deposited to define the shape of the specimens. The thickness of each zone comprising the structure, m-ZTA, t-ZTA, and m-ZTA were 400 µm, 1600 µm, and 400 µm, respectively.

Four sets of ZTA bars were also constructed by 3DP. Figure 4.20 illustrates the different types of ZTA specimens. These specimens shall be referred to as t-ZTA, 3L1, 3L2, and 5L from this point on. The thicknesses of constituent layers are summarized in Table 4.1. The binder combination used to build these sets of bars was 5 vol% Rhoplex

and Y(NO₃)₃ mixed in 5 vol% Rhoplex. This approach corresponds to the third method illustrated in Figure 3.8.

t-ZTA	3L1	3L2	5L
No Residual	σ_{com} = -528 MPa	σ_{com} = -594 MPa	σ_{com} = -528 MPa
Stresses	σ_{ten} = 264 MPa	σ_{ten} = 198 MPa	σ_{ten} = 264 MPa
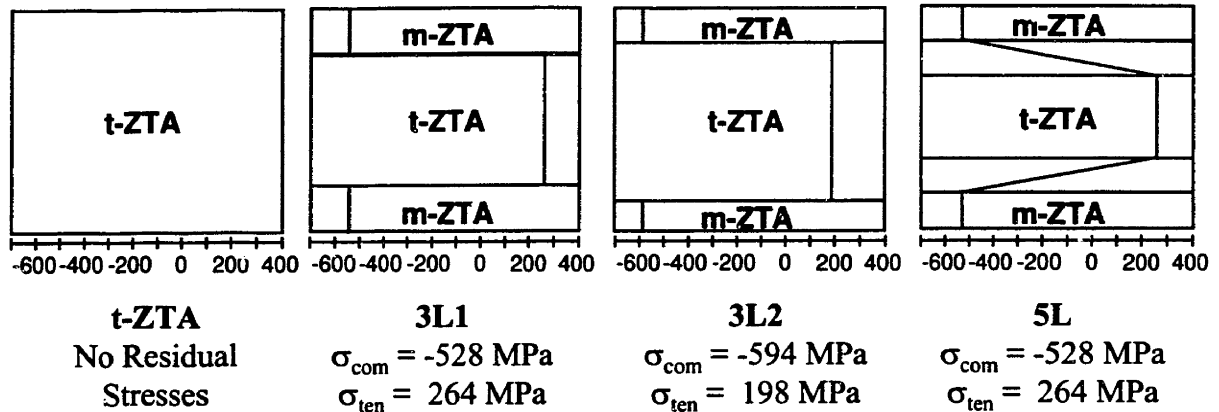
Figure 4.20: Different types of ZTA specimens prepared by 3DP.

Table 4.2: Thickness of each layer in the ZTA multilayer structures.

Layer Type	t-ZTA	3L1	3L2	5L
m-ZTA	NA	400μm	300μm	200μm
Graded Layer	NA	NA	NA	400μm
t-ZTA	2400μm	1600μm	1800μm	1200μm
Graded Layer	NA	NA	NA	400μm
m-ZTA	NA	400μm	300μm	200μm

Isostatic Pressing, Binder Removal, and Sintering

Two different post-processing schemes were used to prepare the 3D-printed ZTA multilayers for sintering. The first method involves WIP at 275 MPa in 80°C oil, followed by binder removal at 450°C for 3 hours. These samples were subsequently fired at 1600°C for 3 hours for densification. The second method involved double stage isostatic pressing. The specimen was CIPed at a low pressure, 137.5 MPa, and then heated to 450°C to remove the binder. The CIPed and debound specimen was then CIPed again at 275 MPa, followed by sintering at 1600°C for 3 hours. This method was designed to eliminate the binder-powder interaction-related defects.

Mechanical Properties

Four point bending tests were conducted on the ZTA specimens constructed by printing Rhoplex/Rhoplex-with-yttrium-nitrate solution. These specimens were *not* ground to the ASTM specification to preserve the compositional gradient. As-fired samples were subjected to bend test in this set of experiments. Several monolithic t-ZTA bars were, however, ground to the standard dimensions and tested. This was feasible because there was no internal compositional gradient in the t-ZTA samples. Vickers indentation was made on a tensile side of the ground specimens to calculate the fracture toughness by using Chantikul et al.'s method [79]. The indentation load used was 9.8 N, which is the highest available load for the microindenter used for this study.

4.3.3 RESULTS AND DISCUSSION

Printing of ZTA components, two different methods

The first set of 3L1 specimens was printed with Acrysol and yttrium nitrate salt solution. Instant flocculation was observed when Acrysol was mixed with yttrium salt solution. This incompatibility led to some practical difficulties in printing. The printhead assembly, for example, had to be constantly cleaned to prevent build up of Acrysol precipitation.

Figure 4.21: Polished cross section of a 3L1 ZTA component. This specimen was WIPed at 275MPa in 80°C, heated to 450°C for 3 hours, then fired at 1600°C for 3 hours.

Microstructure of the WIPed and fired specimens showed defects that may have been caused by the interaction between two binder systems. Figure 4.21 is a polished cross section showing the linear printing defects. The orientation of the fast axis is perpendicular to the plane of the micrograph. Low density regions are surrounded by well-polished, dense regions. The average number of transition between dense to porous regions across the thickness of the sample is around 20. There were total of 24 printed layers in this specimen. These suggest that top portion of each layer was porous while the bottom half had higher density, or vice versa. It is conceivable that the yttrium nitrate solution distributes evenly into a freshly spread powder layer. Acrysol may start to precipitate rapidly on top of the layer without getting a chance to penetrate down to the bottom of the layer when it is printed into a powder layer that already contains yttrium salt.

Stress, σ(z) (MPa)

(a)   (b)
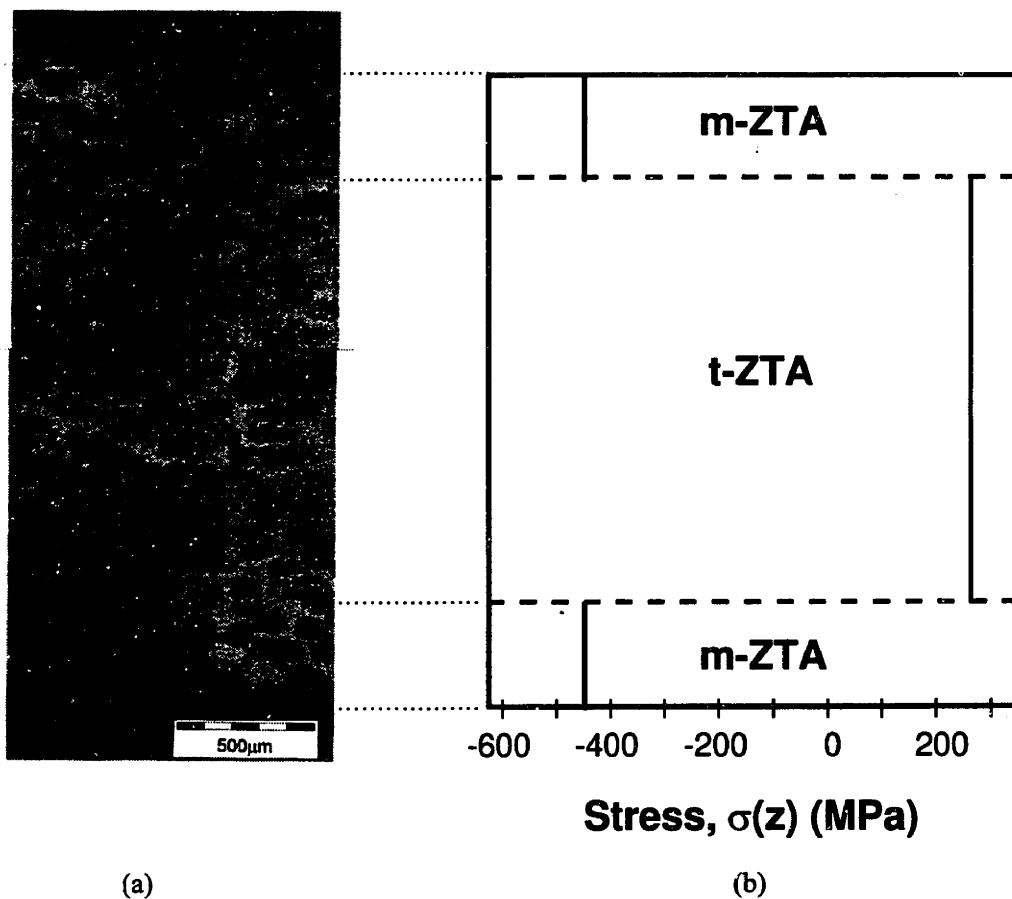
Figure 4.22: (a) Cross section of a trilayered ZTA part showing propagation of crack initiated from the t-ZTA region. (b) Schematic of the trilayered ZTA and the calculated internal residual stress profile.

Internal cracks initiated from the above mentioned defects due to the high internal stress within symmetric multilayer ZTA system as can be seen in Figure 4.22. Internal stress within the t-ZTA portion reaches 264 MPa in this ZTA system, which causes the rapid propagation of a crack within this layer. Not surprisingly, however, the tip of the crack is arrested near the m-ZTA interface. This observation confirms the presence of compressive stress in the m-ZTA layers. Examples of crack propagation along the interfaces originated from t-ZTA layers due to jump of internal stress at the interfaces were also observed in Figure 4.6. Such cracking can be mitigated by introducing FGM interlayers. Figures 4.23 and 4.24 are taken near the surfaces of ZTA multilayers which had *tensile* residual stresses. The specimen with an abrupt interface between t-ZTA and m-ZTA had a prominent crack emanating from the t-ZTA surface region. The crack, however, branched into two due to the presence of sharp stress gradient as shown in Figure 4.21. The specimen with a graded interlayer, in contrast, exhibited a propagation of a crack in a straight path before coming to a stop, as shown in Figure 4.22. These observations are explained by the residual stress profile placed by 3DP.
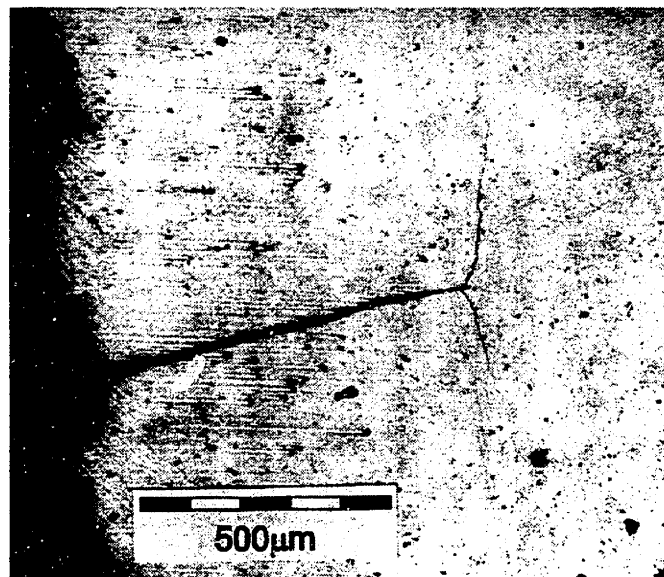
Figure 4.23: Crack deflection observed in a ZTA with abrupt interface.
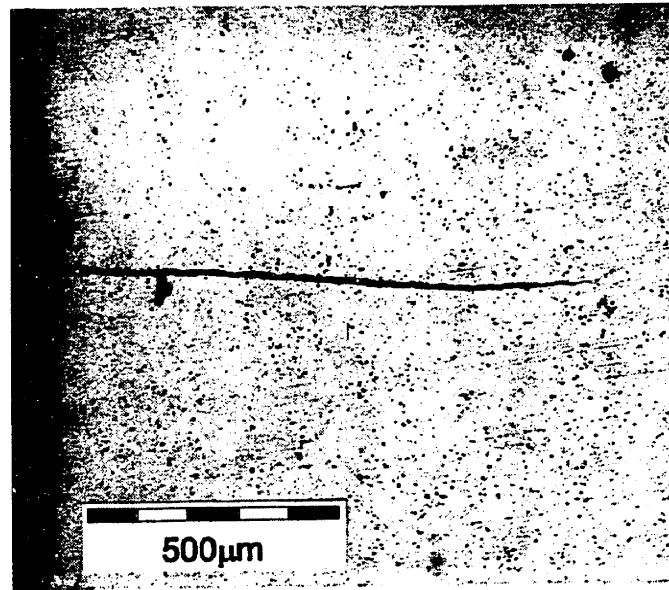
Figure 4.24: Crack propagation observed in a ZTA specimen with gradual change in composition.
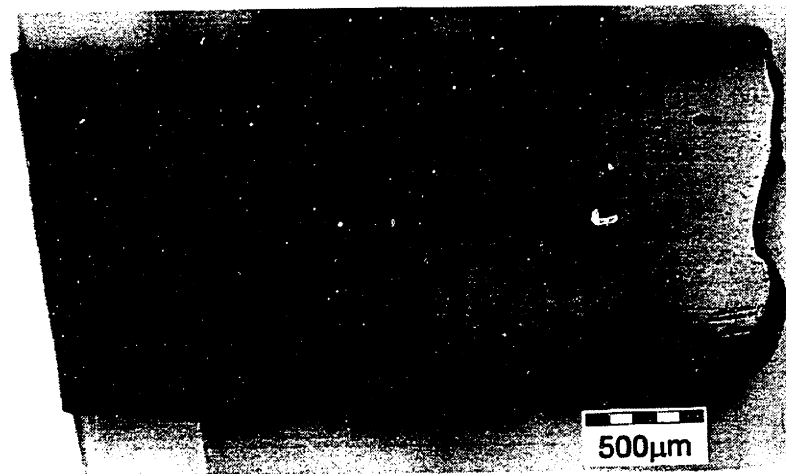
Figure 4.25: Polished cross section of 3L1 ZTA specimen. The specimen was prepared by "double CIP" method to eliminate printing defects.

The defects introduced by the binder incompatibility in the Acrysol/yttrium salt specimens were, however, eliminated by modifying the post process sequence. Shown in Figure 4.25 is a cross section of a 3L1 specimen from the same batch as the specimen for Figure 4.21. The only difference in preparation of the two samples is that sample for Figure 4.25 had binder removal *before* isostatic pressing. Absence of segregated polymer in pre-debound samples allowed superior packing of granules during isopressing step. The green strength required to withstand handling after binder removal was provided by an intermediate isopressing prior to burnout. Pressure used for pre-compaction stage was

137.5 MPa, one half that of the final compaction. This double-compaction procedure was successfully used to prepare fully dense ZTA specimens.

Mechanical Properties

Results of the four point bend tests for multilayer ZTA components are summarized in Figure 4.26. These specimens were prepared by printing Rhoplex/Rhoplex-with-yttrium-nitrate binder combinations. The average strength of t-ZTA from an as-fired specimen was 340 MPa while properly ground samples showed an average of 670 MPa. This dramatic decrease in flexural strength can be attributed to the surface flaws in the as-fired specimens which act as the crack initiation sites upon loading. 3L1, 3L2 and 5L specimens had 423 MPa, 410 MPa, and 441 MPa, respectively.
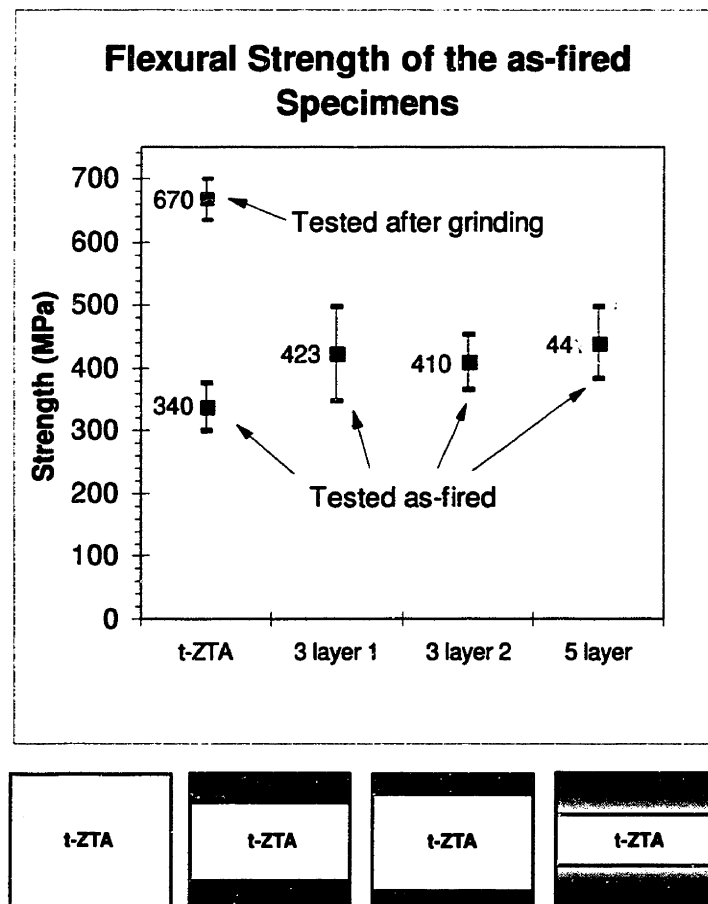
Figure 4.26: Flexural strength of various ZTA multilayers.

They are all substantially higher than that of the monolithic t-ZTA specimens. This increase in strength suggests the presence of compressive residual stress at the tensile surfaces of 3D-printed multilayer composites. Calculations suggest that the flexural strength should increase by the magnitude of the compressive stress present at the surfaces. This implies that the specimen with the thinnest m-ZTA surface layer must have the highest strength. The experimental results from the 3D-printed multilayer structures, however, do not show significant difference between the strength of 3L1, 3L2, and 5L specimens. This is attributed to the presence of large defects on the surfaces of these as-fired bend test specimens. These bend strength values are also lower than typically reported values for ZTA specimens. Surface roughness in the test samples, however, should be the main cause of lower values, as evidenced by the high strength from properly ground 3DP t-ZTA specimen. Strength of 670 MPa for t-ZTA with 15 vol% ZrO$_2$ is comparable to that of conventionally prepared samples which range from 500 MPa to 800 MPa.

Strength of the pre-indented bend test specimens was 375 MPa. Chantikul et al. derived the relationship between fracture toughness, hardness, and indentation load as

$$K_c = \eta_v^R (\frac{E}{H})^{1/8} (\sigma P^{1/3})^{3/4} \tag{4.15}$$

where $\eta_v^R = 0.59 \pm 0.12$, E is the Young's modulus, H is the Vickers hardness, σ is the fracture strength [79]. P is the load used to indent the specimen. K_c of the 3D-printed t-ZTA specimen was calculated to be 4 MPa$\sqrt{m}$ by taking $E = 300$ GPa, $H = 17.3$ GPa, and $P = 9.8$ N. This fracture toughness is in good agreement with the values reported by other investigators.

4.4 CONCLUSIONS

ZTA components with designed compositional gradient were constructed by selectively depositing yttrium nitrate salt solution. X-ray diffraction studies demonstrated the effectiveness of the computer-derived microstructure control. Curvature development

in the graded ZTA multilayers were accurately predicted by an analytical solution developed by Cho and Suresh. The local variation in phases developed residual stress in the 3D-printed ZTA components. Microstructural examination revealed that the crack propagation characteristics in these samples can be customized by manipulating the compositional profile. Flexural strength of the ZTA specimens were also significantly enhanced by placing surface compression layers via 3DP.

5. Computer-Derived Microstructures for Tailored Properties

5.1 INTRODUCTION

Results from the previous chapter demonstrated that local composition and property of ZTA components can be controlled through selective doping by 3DP. The residual stress development in ZTA components caused the cracks to initiate and propagate in a predicted manner. The analytical solution developed for graded ZTA layers were also used to predict the residual stress profile within a sample and the thermomechanical response of thin multilayer ZTA plates. This analytical tool was used to design ZTA components with graded surface layer.

A case study of notched ZTA compression test specimen is presented in this chapter. This is an example of computer-derived microstructure to control mechanical properties. Monoclinic ZTA was strategically placed to slow down both the crack initiation and propagation in the fatigue specimen. Localized compositional variation can also be utilized to control various other properties such as permeability and piezoelectricity. Later half of this chapter presents examples of applications where computer-derived control of composition can make an impact.

5.2 NOTCHED ZTA COMPRESSION BLOCK

ZTA multilayer structures from section 4.3 demonstrated 3DP's ability to tailor the surface characteristics of ZTA components to enhance flexural strength. Crack propagation behavior of the specimens were also altered by the controlled stabilization of zirconia particles. This section presents yet another example of a 3DP-derived ZTA specimen with controlled microstructure and mechanical properties. This marks the first time that a component's geometry and microstructure was designed by computer and manufactured directly by a computer aided process.

124

5.2.1 PROPERTY DESIGN

Figure 5.1 shows the shape and dimensions of the notched compression block. The specimen was designed to be tested under compression to study the crack initiation and propagation. The stress distribution under compressive loading was calculated through a finite element analysis (FEA). A PC based FEA tool called PDEase (SPDE Inc., CA) was used to perform calculations. The actual PDEase codes used for calculations can be found in the Appendix.
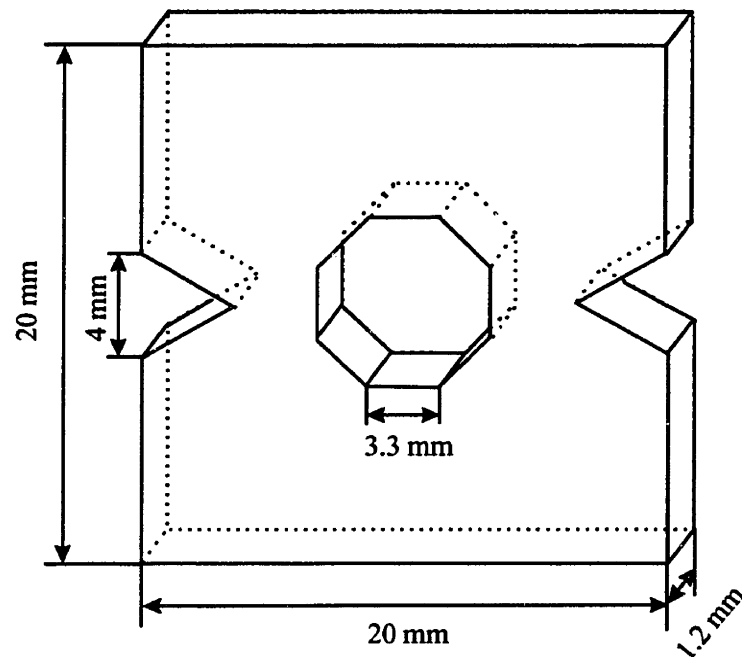
Figure 5.1: Shape and dimensions of the notched compression specimen.

Two different sets of boundary conditions were used to calculate the stress development in the compression specimens. A constant loading case was considered in one case and a constant displacement was considered in the other. The profile of σ_x for a constant loading of 1KN is shown in Figure 5.2. The maximum compressive stress is found at the tip of the notch as expected. Tensile stress is the highest in the middle of the octagonal opening. σ_y for the constant loading case is shown in Figure 5.3.
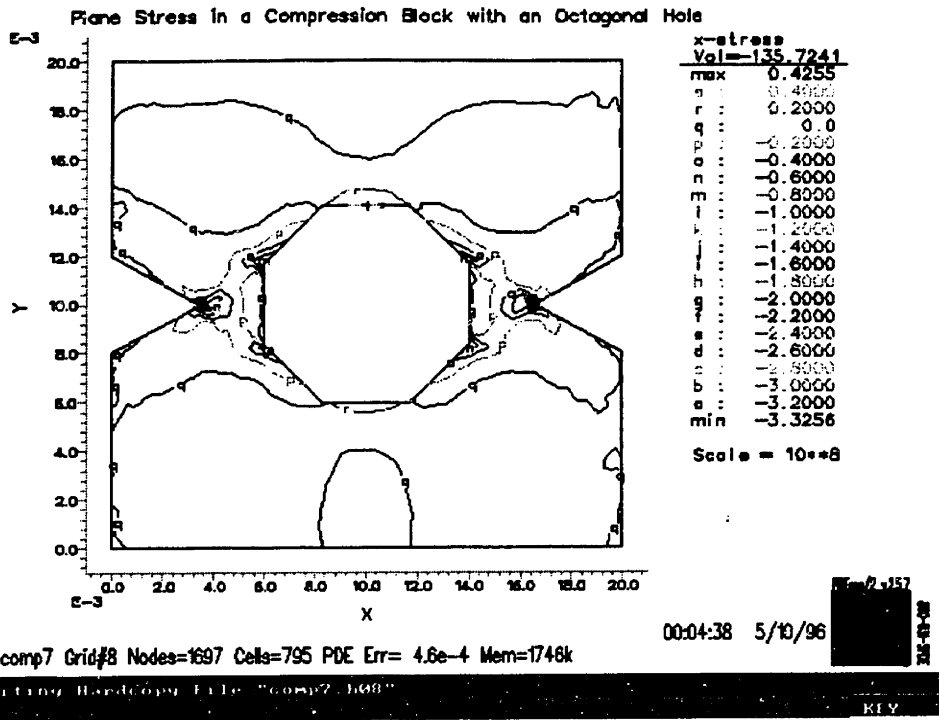
Figure 5.2: x-stress upon loading 1KN.
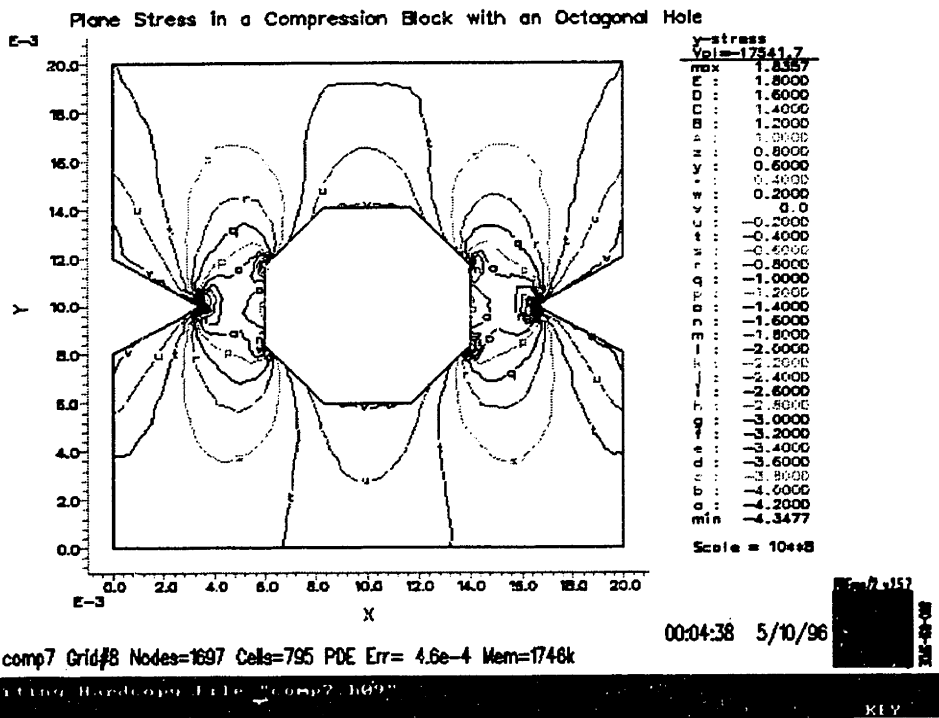
Figure 5.3: y-stress upon loading 1KN.
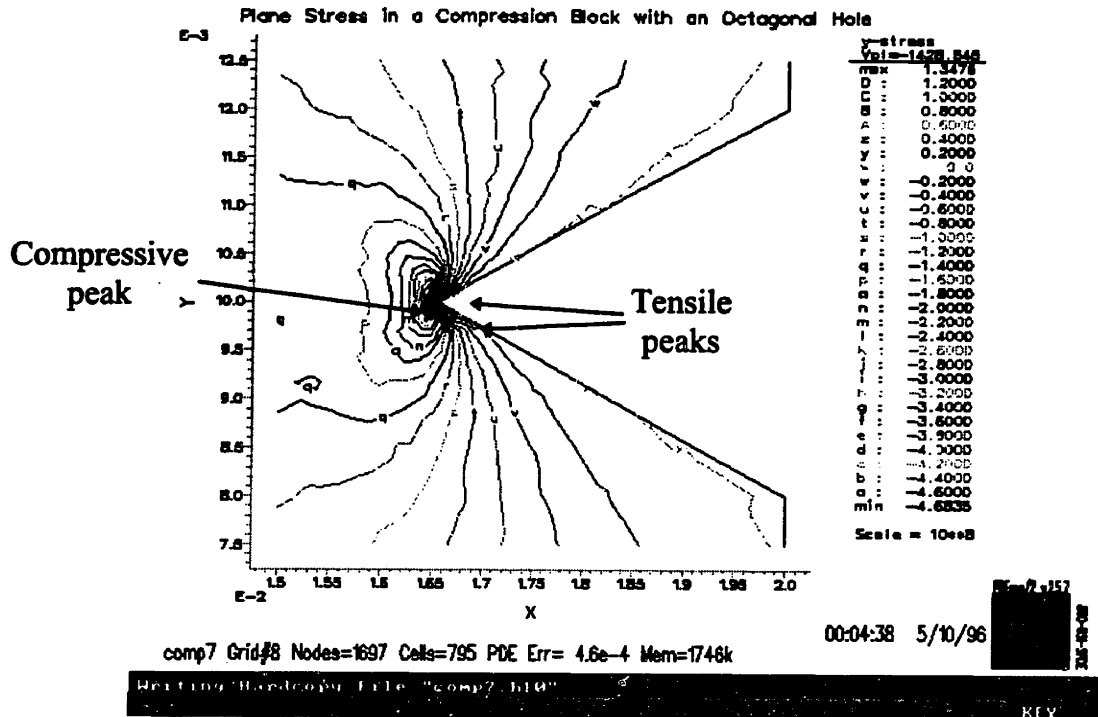
Figure 5.4: y-stress at the notch upon loading 1KN.
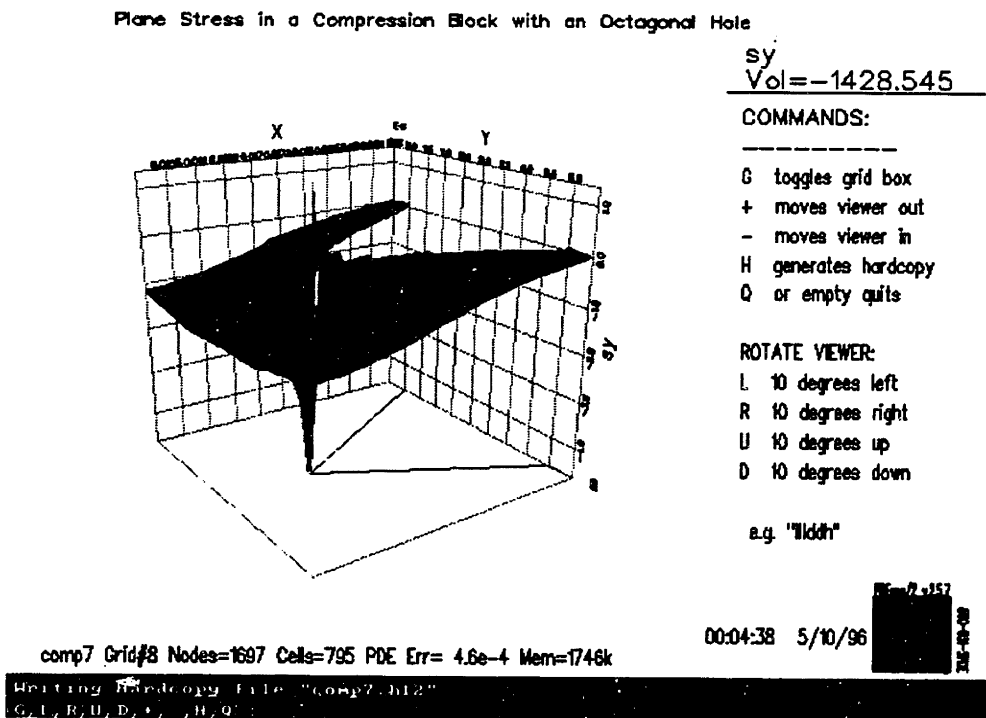
Figure 5.5: y-stress at the notch upon loading 1KN.

A detailed examination of σ_y near the notch tips revealed interesting stress distribution as illustrated in Figures 5.4 and 5.5. The highest compressive stress is concentrated at the notch tip as expected. Regions of high tensile stress are, however, found right around the tip of the notch as shown in Figure 5.5. The magnitude of the tensile stress was roughly one third of the maximum compressive stress in the specimen. Typical compressive strength of a ceramic component is an order of magnitude higher than its tensile strength [80]. This component was, as a consequence, predicted to initiate a crack near the notch tip due to a tensile stress upon compressive loading.

Figures 5.6 and 5.7 show the stress distribution in the notched specimen with a constant displacement as the boundary condition. The location and magnitude of the maximum tensile and compressive stresses did not change significantly from the constant load case. Maximum tensile stress was exerted near the notch tip, and again, the magnitude of the tensile stress was roughly one third that of compressive stress. Calculated maximum stresses in this specimen at various loads and displacements are shown in Table 5.1.

Table 5.1: Calculated stress maxima in Notched ZTA specimens.

Constant Load						Constant Displacement					
Load	Disp.	σ_x (MPa)		σ_y (MPa)		Load	Disp.	σ_x (MPa)		σ_y (MPa)	
(KN)	(μm)	comp.	tensile.	comp.	tensile.	(KN)	(μm)	comp.	tensile.	comp.	tensile.
0	0	0	0	0	0	0	0	0	0	0	0
1	4.8	316	40	413	175	1	4.8	336	19	408	151
1.5	7.25	474	51	620	262	1.5	7.25	508	29	617	243
2	9.75	832	80	826	349	2	9.75	883	39	829	327
5	24	1580	202	2066	874	5	24	1681	96	2042	804
7	33.6	2212	280	2891	1225	7	33.6	2354	133	2858	1126
10	48	3160	400	4130	1750	10	48	3363	192	4083	1508
12.5	60	3950	500	5163	2188	12.5	60	4204	240	5104	2010
15	72	4740	600	6195	2625	15	72	5044	288	6125	2412
17	81.6	5372	680	7021	2975	17	81.6	5717	326	6941	2734
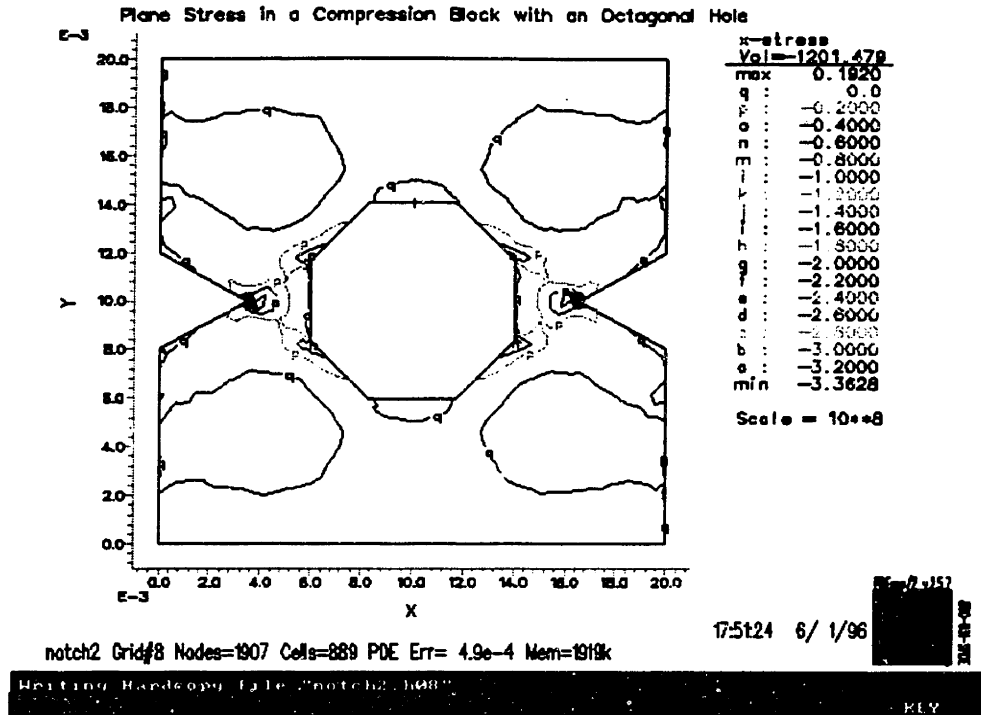
Figure 5.6: x-stresses calculated based on a constant displacement model.
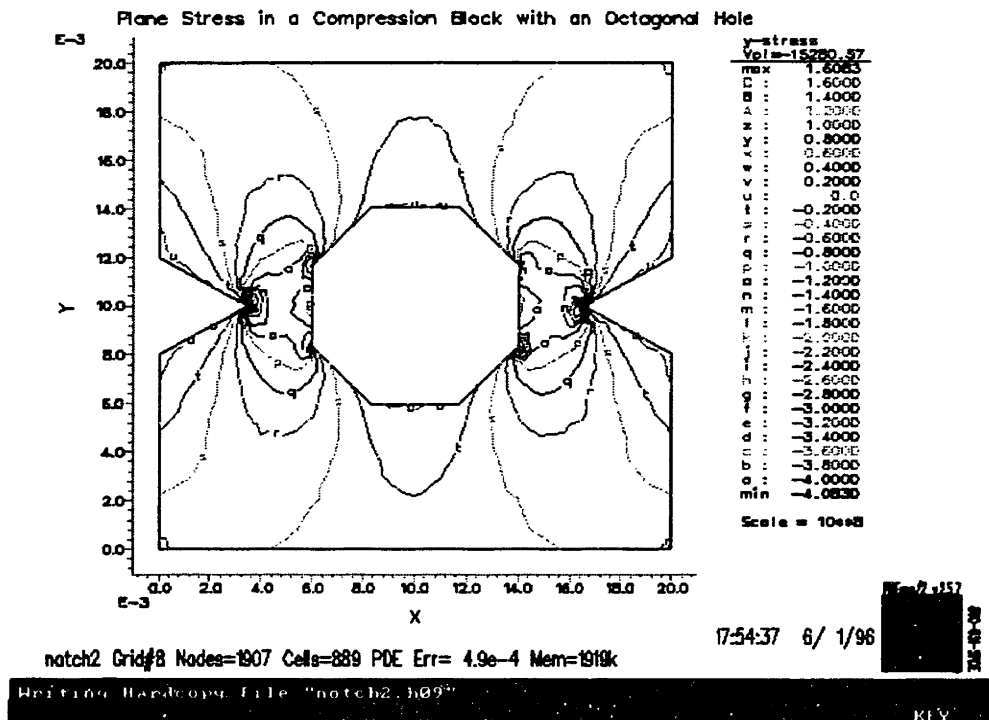
Figure 5.7: y-stresses calculated based on a constant displacement model.
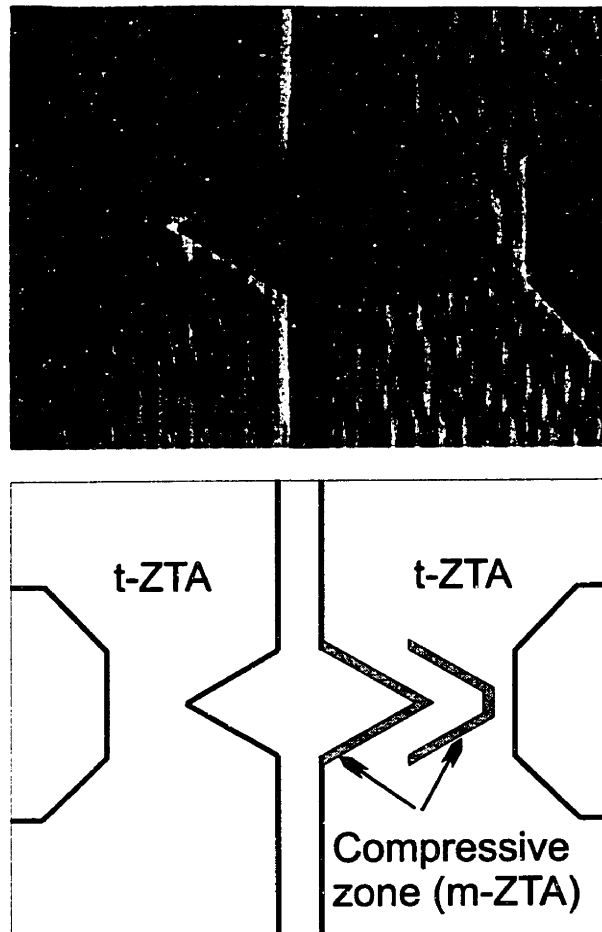
Compressive zone designed to
offset tensile stress when
component is loaded axially

Figure 5.8: Compressive zone designed to offset tensile stress when component is loaded axially.

A notched compression block with an identical geometry and slight variation in composition from the above was designed to impede the crack initiation and propagation under compressive loading. Figure 5.8 shows the schematic of the specimen near the notch tip. A band of m-ZTA zone was placed on the notch tip to introduce a residual compressive zone. Another band of m-ZTA was placed near the notch in order to either impede or deflect the cracks emanating from the notch tip. This is analogous to the crack tip deflection observed from the ZTA multilayer structures.

5.2.2 EXPERIMENTAL PROCEDURE

Sample Preparation

The notched blocks were prepared by printing Rhoplex/Rhoplex with yttrium nitrate binder combination. Spray-dried ZTA granules were spread by counter-rotation method. 3D-printed greenbodies were CIPed at 137.5 MPa prior to binder removal. The deboud sample was CIPed again at 275 MPa, followed by sintering at 1600°C for 3 hours.

Both faces of the notched block were ground and polished to facilitate *in situ* notch tip observation during compression test. Precision grinding was performed on the loading faces to ensure the specimen was loaded in a uniform fashion and to prevent premature buckling of the samples upon compression [81].

Compression Tests

Both the monotonic and cyclic compressive loading conditions were used to test the 3D-printed ZTA blocks. Monotonic loading was carried out in an incremental fashion. The sample surfaces near the notch tips were observed with a telescope and recorded on a video cassette. Cyclic compression was carried at a frequency of 1 Hz. The R ratio between the maximum and minimum compressive loads was kept at 10 at all times. The maximum compressive loads for cyclic loading were also slowly increased. 500 cycles of compression were performed before increasing the load. Optical microscope was used to examine the notch tips periodically to find fine details of the crack initiation and propagation.

5.2.3 RESULTS AND DISCUSSION

Different modes of failure were observed from the compression tests of notched ZTA blocks. Number of samples failed at very low loads, under 2KN, which corresponds to a maximum tensile stress of only 330 MPa near the notch tip. The cracks were very fine and followed straight path. All of the specimens that failed in this mode had pre-existing cracks prior to the compression test.

8 KN

13 KN

17.5 KN
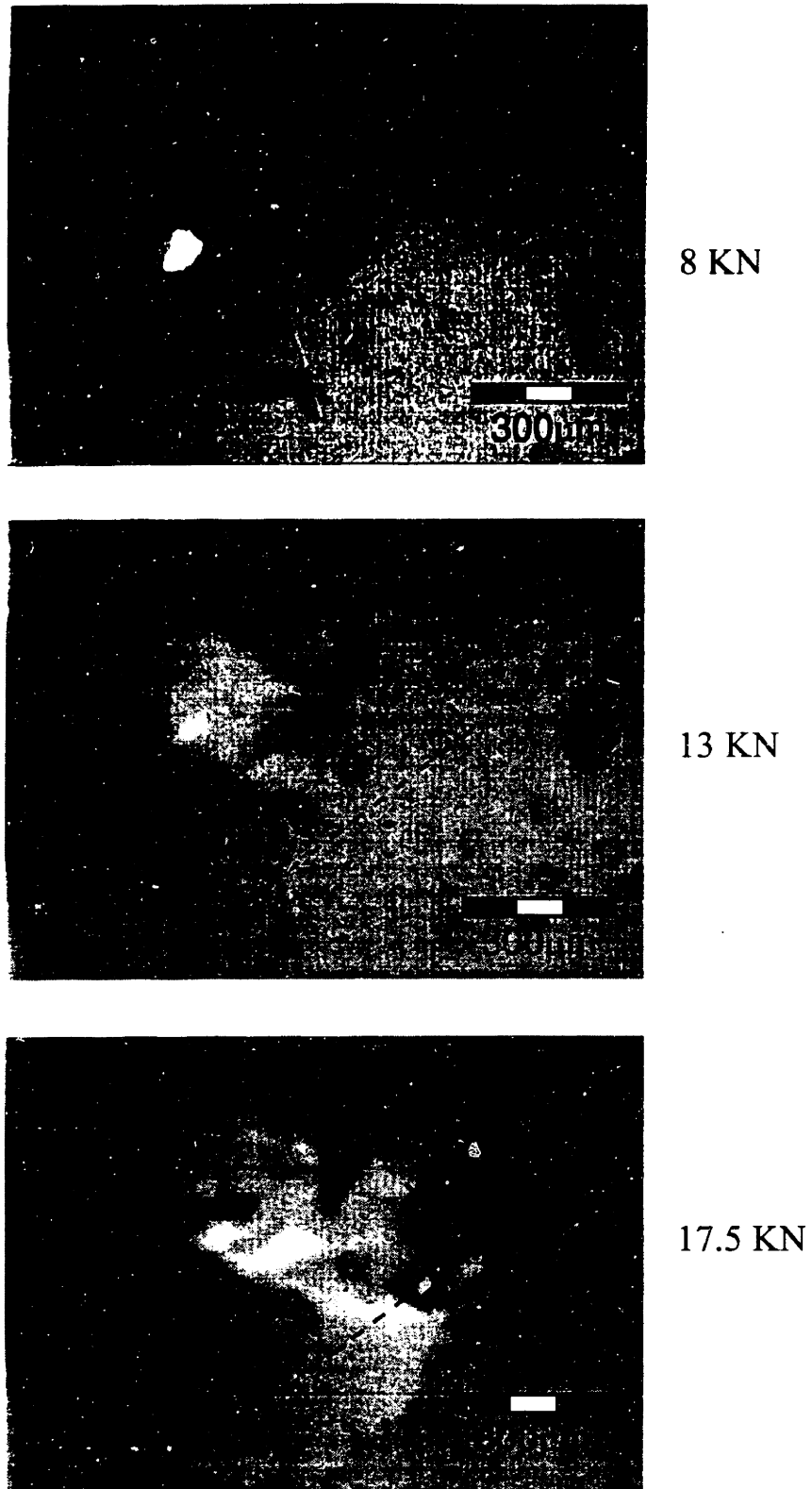
Figure 5.9: Damage at the notch tip upon far-field monotonic compressive loading.

Specimens that did not have precracks sustained very high compressive loads and the mode of fracture was distinctively different from the ones with precracks. The high stored elastic energy caused the specimens to disintegrate into small pieces upon failure. One of the precrack-free monolithic specimen failed at 12.5 KN while another monolithic specimen fractured at 7 KN. This is in contrast with the specimens with shielded notch tips. The average load at failure for the precrack-free shielded-notch blocks were 17.25 KN. This is a remarkable increase in the failure load from the average of 10 KN for the monolithic specimens. The increase in the failure load indicates that the m-ZTA zone around the notch tip is exerting a compressive residual stress to prevent the fracture.

Observation of the changes in the notch tip during the compression test also revealed an important information about the role of the notch tip shield placed by 3DP. Shown in Figure 5.9 are series of frames from the video recording of the notch tip. The sample under compression had 3D-printed built-in notch tip shields. Spalling of the surface started at a monotonic loading of 8 KN as shown in the first frame. More damage in the surface was observed with the slow increase in the far field loading. The second frame in Figure 5.15 was taken from the sample at applied load of 13 KN. The size of the damaged zone increased as the compressive load was increased. The third frame was taken from the notch tip when the applied load was 17.5KN, just before the sample fractured into small pieces. The size of the damaged region matches precisely with the width of the m-ZTA shield. This observation confirms the effectiveness of the m-ZTA shield on preventing the propagation of cracks. The cracks initiating near the notch tip are prevented from propagating through the zone due to the compressive stress. The lack of constraining stress causes the crack to experience an unstable growth once the crack size outgrows the compressive zone size.

The effect of the secondary compressive zone situated in the middle of the ligaments, however, could not be evaluated from this set of test. The crack growth rate for all of the tested specimens were too rapid to be affected by the m-ZTA zone.

Results from the compression tests of notched ZTA blocks demonstrated the role of m-ZTA shield zones in enhancing the load-bearing characteristics. This study showed

that inexpensive computing power can be used to design a component, predict the mode of failure, and then directly construct components with compositional variation to enhance and control mechanical properties.

5.3 OTHER EXAMPLES

5.3.1 DRUG DELIVERY DEVICES

Another example of a SFF-derived component with localized compositional variation is the 3D-printed drug delivery device (DDD) [23,82]. These drug delivery devices are an example of a nonstructural application for a compositionally graded material. They are used when controlling the release rates of different drugs is desirable. A model device was 3D-printed with polymeric matrix that undergoes hydrolytic degradation. Figure 5.10 shows the macroscopic configuration of a model device.
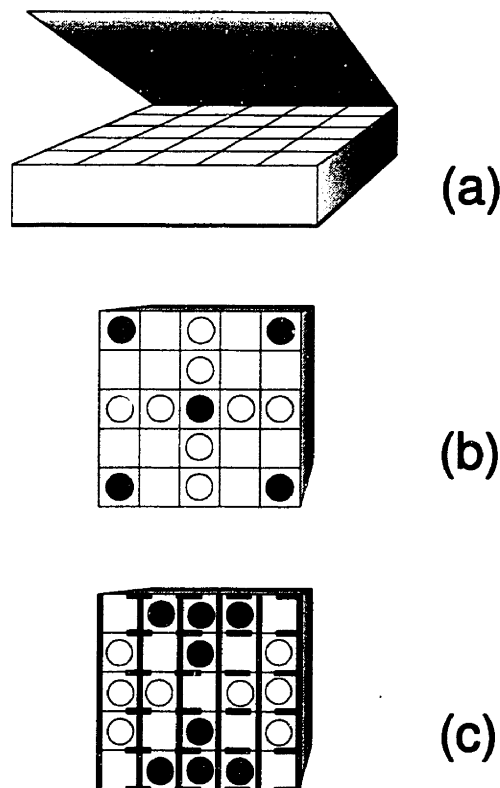
Figure 5.10: (a) Schematic of a 3D-printed model drug delivery device. (b) DDD with strategic placement of two different drugs. Circles with different shades represent different drugs. (c) DDD with compositional variation to control release rate. Thick lines represent the walls that have substantially lower rate of desorption than the ones represented by thin lines. (Wu et al. [82])

Numerous compartments are built into the device and various drugs are appropriately placed. When the device is placed in a patient, either by implantation or taken orally, resorption of the polymer matrix results in release of the drugs from the micro-reservoirs. The lag time required to release drugs from each of the compartments can be tailored to meet specific prescriptions for individual patients. Composition and microstructure of the matrix polymer, and the thickness of the compartment walls have a great impact on both the resorption rate and mechanism. Wu et. al [82] reported promising results in a preliminary investigation where controlled release of various dyes from 3D-printed model devices were tested.

5.3.2 SLIP CASTING MOLDS

Slip casting has been widely used to prepare ceramic green bodies with complex shapes [83]. One of the major difficulties in slip casting is controlling the local casting rate on the surface of the mold. This is particularly important for full section castings where one desires blind surfaces in certain locations where no casting takes place. This ensures that the path for new slip is not blocked off prematurely, resulting in internal cavities. Conventional slip casting practices require complex pre-casting conditioning of molds to eliminate these characteristic deficiencies. 3D-printed molds with compositional variation and internal features designed to control slip casting rates were studied by Grau.[84] A schematic of a split mold is shown in Figure 5.11. Internal channels are strategically positioned as to reduce the driving force for the casting of the slip. A similar effect can be achieved by placing regions of dense glassy layers within the mold walls. Both of these approaches have proven to be effective in controlling the casting rates in 3D-printed alumino-silicate molds. We envision that designers of slip casting molds can use CAD software to provide the macroscopic shape of the desired component and the microstructure within the component simultaneously.
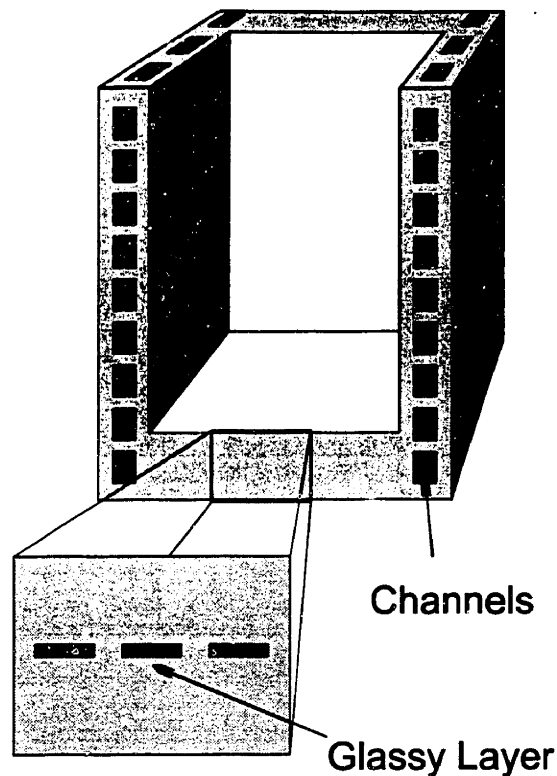
Figure 5.11: Schematic of a 3D-printed slip casting mold with channels and glassy layers to control the casting rate.

5.3.3 Piezoelectric Actuators

Piezoelectric constants of the lead zirconate-lead titanate mixtures (PZT) are known to vary significantly with composition [85,86]. Proportion of the lead zirconate and lead titanate can be controlled to tailor piezoelectric properties. Small amounts of dopants, such as strontium, can also dramatically affect the properties of PZT. 3DP can be used to control the local composition of a PZT component to tailor the piezoelectric response of the structure just as selective doping was used to control mechanical properties of ZTA components [87]. The macroscopic shape and porosity of a PZT structure can be also designed and fabricated to change the effective piezoelectric property of a PZT structure with a fixed composition. 3DP has demonstrated all of the above mentioned property control mechanisms, and can be adapted to fabricate PZT components which can be used for different types of actuation applications.

5.4 CONCLUDING REMARKS

SFF techniques have many different advantages over conventional manufacturing processes. Reduced time and cost for small scale production is one of the advantages. The flexibility in the range of shapes that can be built by SFF methods is revolutionary. 3DP has an additional advantage that even other SFF methods do not possess. The ability to control local composition and macroscopic shape simultaneously sets 3DP apart from other SFF methods. This advantage should be exploited to create structures with tailored properties. Mechanical and thermal response of 3D-printed ZTA components were investigated in this study. The results from this work successfully demonstrated the effectiveness of 3DP in designing and building various ZTA structures. Properties that can be controlled by 3DP are, however, not just restricted to mechanical properties. Many different types of properties that are sensitive to the microstructure and local composition may be designed and controlled by 3DP.

Scale up potentials of 3DP for mass production relies on the ability to incorporate multiple jets to increase the binder deposition rate. It is encouraging to note that current ink-jet printing technology employs hundreds of jets simultaneously to deposit three different colors. 3DP will be able to benefit from the developments in the ink-jet printing technologies to increase the production rate as well as the microstructural complexity.

BIBLIOGRAPHY

1. Marcus, H.L., J.J. Beaman, D.L. Bourell, J.W. Barlow, and R.H. Crawford. (1995). Editors, *Proceedings of the Solid Freeform Fabrication Symposium* (Austin, TX, August, 1995). The University of Texas at Austin, TX.

2. Marcus, H.L., J.J. Beaman, D.L. Bourell, J.W. Barlow, and R.H. Crawford. (1994). Editors, *Proceedings of the Solid Freeform Fabrication Symposium* (Austin, TX, August, 1994). The University of Texas at Austin, TX.

3. Burns, M. (1993). *Automated Fabrication : Improving Productivity In Manufacturing*, PTR Prentice Hall, Englewood Cliffs, NJ.

4. Kochan, D. (1993) Editor, *Solid Freeform Manufacturing : Advanced Rapid Prototyping*, Elsevier, New York, NY.

5. Dvorak, P., L. Teschler, (1993). From Data to Finished Parts, *Machine Design*, p.75~80.

6. Kruth, J.P., Material Incress Manufacturing by Rapid Prototyping Techniques.

7. Benedict, G.F., (1989). Stereolithography-the new design tool for the 1990's, in Proceedings of 6th International Conference on Lasers in Manufacturing, p.249~261.

8. Holusha, J., (1993). Slicing and Molding by Computer, *The New York Times*, D5, April 7.

9. Feygin, M. and B. Hsieh, (1991). Laminated Object Manufacturing (LOM): A Simpler Process, in *Proceedings of the Solid Freeform Fabrication Symposium* (Austin, TX, August, 1991). p. 123, The University of Texas at Austin, TX.

10. Griffin, C., J. Daufenbach, and S. McMillin, (1994). Desktop Manufacturing: LOM vs. Pressing, *Am. Cer. Soc. Bull.* 73[8] p.109.

11. Feygin, M., (1988). Apparatus and Method for Forming an Integral Object from Laminations, U.S. Patent No. 4,752,352.

12. Daufenbach, J., and C. Griffin, (1995). Alumina/Zirconia Layered Composites Formed by Laminated Object Manufacturing, presented at the 97th Annual Meeting of the American Ceramic Society, Cincinnati, OH.

13. Jacobs, P.F. (1992). *Rapid Prototyping & Manufacturing: Fundamentals of Stereolithography*, First Edition, Society of Manufacturing Engineers, Dearborn MI.

14. Griffith, M.L. (1995). Stereolithography of Ceramics, Ph.D. dissertation, Department Materials Science and Engineering, The University of Michigan, Ann Arbor, MI.

15. Deckard, C. and J. Beaman (1987). Recent Advances in Selective Laser Sintering, in *Proceedings of the Fourteenth Conference on Production Research and Technology*, pp. 447-452, University of Michigan, MI.

16. Vail, N.K., J.W. Barlow, and H.L. Marcus (1993). SiC Preforms for Metal Infiltration by Selective Laser Sintering of Polymer Encapsulated Powders, in *Proceedings of the SFF Symposium*, p.204, University of Texas, Austin, TX.

17. Sachs, E.M., M.J. Cima, P. Williams, D. Brancazio, and J. Cornie (1992). Three-Dimensional Printing: Rapid Tooling and Prototypes Directly from a CAD Model, *J. Eng. Ind.*, **114** pp. 481-88.

18. Sachs, E., M.J. Cima, J. Bredt, and A. Curodeau (1992). CAD-Casting: The Direct Fabrication of Ceramic Shells and Cores by Three Dimensional Printing, *Man. Rev.* **5** [2] pp. 117-126.

19. Sachs, E. et al., (1993). Three Dimensional Printing Techniques, U.S. Patent no. 5,204,055.

20. Yoo, J., M.J. Cima, S. Khanuja, and E. Sachs (1993). Structural Ceramic Components by 3D Printing, in *Proceedings of the SFF Symposium*, pp.40-50, Univ. of Texas, TX.

21. Cima, M.J., J. Yoo, S. Khanuja, M. Rynerson, D. Nammour, B. Giritlioglu, J. Grau, and E.M. Sachs (1995). Structural Ceramic Components by 3D Printing, , in *Proceedings of the SFF Symposium*, pp.479-488, Univ. of Texas, TX.

22. Michaels, S., E.M. Sachs, and M.J. Cima (1992). Metal Parts Generation by Three Dimensional Printing, in *Proceedings of the SFF Symposium*, pp.244-250, Univ. of Texas, TX.

23. Cima, M.J., E. Sachs, L.G. Cima, J.Yoo, S. Khanuja, S.W. Borland, B. Wu, and R.A. Giordano (1994). Computer-Derived Microstructures by 3D Printing: Bio- and Structural Materials, in *Proceedings of the SFF Symposium*, pp.181-190, University of Texas, TX.

24. Wales, R., and B. Walters (1991). Fast, Precise, Safe Prototypes with FDM, in *Proceedings of the SFF Symposium*, p. 115, University of Texas, Austin, TX.

25. Agarwala, M.K. et. al (1995). Structural Ceramics by Fused Deposition of Ceramics, in *Proceedings of the SFF Symposium*, pp.1-8, University of Texas, TX.

26. Monti, C., (1996). Setter Design for Binder Removal from Injection-Molded Ceramic Components, Master of Science Thesis, Massachusetts Institute of Technology.

27. Yoo, J., M. Cima, E. Sachs, S. Suresh, (1995). Fabrication and Microstructural Control of Advanced Ceramic Components by Three Dimensional Printing, p.755-762, *Ceramics Engineering and Science Proceedings*, Edited by G.N. Pfendt.

28. Rabin, B.H. and I. Shiota, (1995). Editors, Functionally Graded Materials, *MRS Bulletin*, p.14-55, Jan.

29. Cho, K. and S. Suresh, (1996). Transformation-Toughened Ceramic Multilayers with Compositional Gradients: Part I. Theory, Submitted to *J. Am. Cer. Soc.*

30. Yoo, J., K. Cho, W.S. Bae, S. Suresh, and M. Cima, (1996). Transformation-Toughened Ceramic Multilayers with Compositional Gradients: Part II. Experiments, Submitted to *J. Am. Cer. Soc.*

31. D.J. Green, R.H.J. Hannink, and M.V. Swain, (1989). *Transformation Toughening of Ceramics*, CRC Press, Inc., Boca Raton, FL.

32. N. Claussen, (1984). Microstructural Design of Zirconia-Toughened Ceramics (ZTC), p.321-351 in Advances in Ceramics, Vol.12, *Science and Technology of Zirconia II*, Edited by N. Claussen, M. Ruhle, and A.H. Heuer, American Ceramic Society, Columbus, OH.

33. W. R. Cannon, (1989). Transformation Toughened Ceramics for Structural Applications, Treatise on Mat. Sci. and Tech., 29, p.195-228.

34. N. Claussen and M. Ruhle, (1981). Design of transformation toughened ceramics, p.137-163, in Advances in Ceramics, Vol.3, *Science and Technology of Zirconia*, eds. A.H. Heuer and L.W. Hobbs, Am. Cer. Soc., Columbus, OH.

35. A.G. Evans, (1984). Toughening mechanisms in zirconia alloys, p.193-212 in Advances in Ceramics, Vol.12, *Science and Technology of Zirconia II*, Edited by N. Claussen, M. Ruhle, and A.H. Heuer, American Ceramic Society, Columbus, OH.

36. Kingery, W.D., H.K. Bowen, and D.R. Uhlmann, (1976). Introduction to Ceramics, John Wiley & Sons, Inc., NY.

37. Bruch, C.A., (1962). Sintering Kinetics for the High Density Alumina Process, *Am. Cer. Soc. Bull.*, 41, 12, p.799-806.

38. Lange, F.F., M. Metcalf, (1983). Processing-Related Fracture Origins: II, Agglomerate Motion and Cracklike Internal Surfaces Caused by Differential Sintering, *J. of Am. Cer. Soc.*, 66, 6, p.398-406.

39. Nammour, D., (1995). Fabrication of Glass-Ceramic Components via 3DP, Master of Science Thesis, Massachusetts Institute of Technology.

40. Khanuja, S., (1996). Origin and Control of Anisotropy in Three Dimensional Printing of Structural Ceramics, Doctor of Philosophy Thesis, Massachusetts Institute of Technology.

41. Arthur, T, (1996). Factors Limiting the Surface Finish of Three Dimensional Printed Parts, Master of Science Thesis, Massachusetts Institute of Technology.

42. Lee, J. S., (1992). Powder Layer Generation for Three Dimensional Printing, Master of Science Thesis, Massachusetts Institute of Technology.

43. Lauder, A., M. J. Cima, E. Sachs, and T. Fan, (1991). Three Dimensional Printing: Surface Finish and Microstructure of Rapid Prototyped Components, Proc. Synthesis of Ceramics: Scientific Issues, MRS, Boston.

44. Fan, T., A. Lauder, E. Sachs, and M. J. Cima, (1992). The Surface Finish in Three Dimensional Printing, Proc. 3rd Int. Conf. on Rapid Prototyping.

45. Shaw, F.V., (1990). Spray drying: A Traditional Process for Advanced Applications, Am. Cer. Soc. Bull. 69, 9.

46. Giritlioglu, B., (1995). The Effect of Print Style on Mechanical and Microstructural Properties of Structural Parts via Three Dimensional Printing, Master of Science Thesis, Massachusetts Institute of Technology.

47. Giritlioglu, B., (1995). Unpublished results.

48. Lauder, A., (1992). Microstructure and Particle Arrangement in Three Dimensional Printing, Master of Science Thesis, Massachusetts Institute of Technology.

49. Lange, F.F., (1989). Powder Processing Science and Technology for Increased Reliability, J. Am. Cer. Soc., 72, 1, p.3-15.

50. Grau, J., and M. Caradonna, (1996). Unpublished results.

51. Bang, W., (1996). ,Master of Science Thesis, Massachusetts Institute of Technology

52. Caradonna, M., (1996). Unpublished results.

53. Cannon, W.R. (1989). Transformation Toughened Ceramics for Structural Applications, in Structural Ceramics, Treatise on Materials Science and Technology (Edited by J.B. Wachtman), pp.195-228,. Academic Press, San Diego, CA.

54. Scott, H.G., (1975). Phase Relationships in the Zirconia-Yttria System, *J. Mater. Sci.*, 10, p.1527-.

55. Heuer, A.H. et al., (1982). Stability of Tetragonal ZrO_2 Particles in Ceramic Matrices, *J. Am. Cer. Soc.* **65**, p.642.

56. Evans, A.G., and R.M. Cannon, (1986). Toughening of Brittle Solids by Martensitic Transformations, *Acta Metall*, **34**, 5, p.761-800.

57. Lange, F.F., (1982). Transformation Toughening: Part II, Contribution to Fracture Toughness, *J. of Mat. Sci.*, 17, p.235-239.

58. Gupta, T.K. (1980). Strengthening by Surface Damage in Tetragonal Zirconia, *J. Am. Cer. Soc.*, **63**, pp. 117-.

59. Green, D.J., (1984). Compressive Surface Strengthening of Brittle Materials, *J. Mat. Sci.*, **19**, p.2165-2171.

60. Lange, F.F., M.R. James, and D.J. Green, (1983). Determination of Residual Stresses Caused by Grinding in Polycrystalline Al_2O_3, *Comm. of the Am. Cer. Soc.*, **66**, 2, p.C16-C17.

61. Green, D.J. (1983). A Technique for Introducing Compression into Zirconia Ceramics, *Comm. Am. Cer. Soc.*, C-178, Oct.

62. Virkar, A.V., J.L.Huang, and R.A. Cutler, (1987). Strengthening of Oxide Ceramics by Transformation-Induced Stresses, *J. Am. Cer. Soc.*, **70**, p.164-170.

63. Cutler, R.A., J.D. Bright, A.V. Virkar, and D.K. Shetty, (1987). Strength Improvement in Transformation-toughened Alumina by Selective Phase Transformation, *J. Am. Cer. Soc.* **70**, p.714~718.

64. Sarkar, P., X. Huang, and P.S. Nicholson, (1993). Zirconia/Alumina Functionally Gradiented Composites by Electrophoretic Deposition Techniques, *J. Am. Cer. Soc.* **76**, p.1055~1056.

65. Broek, D., (1988). The Practical Use of Fracture Mechanics, Kluwer Academic Publishers, Boston, MA.

66. Nicholson, P.S., P. Sarkar, and X.N. Huang, (1993). Potentially Strong and Tough ZrO_2-Based Ceramic Composites above 1300°C by Electrophoretic Deposition, Science and Technology of Zirconia V, p.503-516.

67. Toraya, H., M. Yoshimura, and S. Somiya, (1984). Calibration Curve for Quantitative Analysis of the Monoclinic-Tetragonal ZrO_2 System by X-ray Diffraction, *J. Am. Cer. Soc.*, **68**, p.C119-C121.

68. Garvie, R.C., and Nicholson, P.S., (1972). Phase Analysis in Zirconia Systems, *J. Am. Cer. Soc.*, **55**, 6, p.303-305.

69. G.R. Anstis, P. Chantikul, B.R. Lawn, and D.B. Marshall, (1981). A Critical Evaluation of Indentation Techniques for Measuring Fracture Toughness: I, Direct Crack Measurements, *J. Am. Cer. Soc.*, **64**, pp.533-538.

70. Marshall, D.B., (1986). Strength Characteristics of Transformation Toughened Zirconia, *J. Am. Cer. Soc.*, **69**, 3, p.173-180.

71. McMeeking, R.M., (1986). Effective Transformation Strain in Binary Composites, *J. Am. Cer. Soc.*, **69**, p.C301-C302.

72. A. Mortensen and S. Suresh, (1996). Functionally graded metals and metal ceramic composites: Part I. Processing, *Intern. Mater. Rev.*

73. S. Suresh and A. Mortensen, (1996). Functionally graded metals and metal ceramic composites: Part II. Thermal and mechanical analysis, submitted to *Intern. Mater. Rev.*

74. M. Niini, T. Hirai, and R. Watanabe, (1987). Functionally gradient materials for aerospace thermal barrier materials, *J. Jpn. Soc. Comp. Mater.*, 13 [6], 257-264.

75. Underwood, E.E., Quantitative Stereology, (1970). Addison-Wesley Publishing, Reading, MA.

76. D.J. Green, F.F. Lange, and M.R. James, (1983). Factors Influencing Residual Stresses due to a Stress-Induced Phase Transformation", *J. Am. Cer. Soc.*, **66**,p.623-629.

77. Timonshenko, S.P., and J.N. Goodier, Theory of Elasticity, 3rd Edition, McGraw-Hill, NY.

78. Giannakopoulos, A.E., S. Suresh, M. Finot, and M. Olsson, (1995). Elastoplastic Analysis of Thermal Cycling: Layered Materials with Compositional Gradients, *Acta Metall. Mater.*, **43**, 4, p.1335-1354.

79. Chantikul, P., G.R. Anstis, B.R. Lawn, and D.B. Marshall, (1981). A Critical Evaluation of Indentation Techniques for Measuring Fracture Toughness: II, Strength Method, *J. Am. Cer. Soc.*, **64**, 9, p.539-543.

80. Schwartz, M., (1992). Handbook of Structural Ceramics, McGraw-Hill.

81. Ugural, A.C., and Fenster, S.K., (1995). Advanced Strength and Applied Elasticity, PTR Prentice Hall, Englewood Cliffs, NJ.

82. Wu, B.M., S.W. Borland, R.A. Giordano, L.G. Cima, E.M. Sachs, and M.J. Cima, (1996). Solid Free Form Fabrication Of Drug Delivery Devices, *J. of Controlled Release*, 40, 1-2, p.77-87.

83. Reed, J.S., (1989). Introduction to the Principles of Ceramics Processing, John Wiley and Sons, NY.

84. Grau, J., and M.J. Cima, (1996). Alumina molds fabricated by 3-dimensional printing for slip casting and pressure slip casting, Submitted for publication in Ceramic Industry.

85. Greninger, D., V. Kollonitsch, and C.H. Kline, (1975). Lead Chemicals, International Lead Zinc Research Organization, NY.

86. Liberatore, M.J., K.E.A. Rigby, and M.J. Cima, (1996). Processing Piezoelectric Fibers for Structural Actuation, Presented at the 98th Annual Meeting of the American Ceramic Society, Indianapolis, IN.

87. Liberatore, M., (1996). Internal Communication.

APPENDIX

The code used for PDEASE analysis of the notched compression block.

{ COMP7.PDE }

{
This example shows the deformation of a compression sample with a hole.

The hole is octagonal shaped.

The equations of Stress/Strain arise from the balance of forces in a
material medium, expressed as

    dx(Sx) + dy(Txy) + Fx = 0
    dx(Txy) + dy(Sy) + Fy = 0

where Sx and Sy are the stresses in the x- and y- directions,
Txy is the shear stress, and Fx and Fy are the body forces in the
x- and y- directions.

The deformation of the material is described by the displacements,
U and V, from which the strains are defined as

    ex = dx(U)
    ey = dy(V)
    gxy = dy(U) + dx(V).

The eight quantities U,V,ex,ey,gxy,Sx,Sy and Txy are related through the
constitutive relations of the material. In general,

    Sx = C11*ex + C12*ey + C13*gxy - b*Temp
    Sy = C12*ex + C22*ey + C23*gxy - b*Temp
    Txy = C13*ex + C23*ey + C33*gxy

In orthotropic solids, we may take C13 = C23 = 0.

Combining all these relations, we get the displacement equations:

    dx[C11*dx(U)+C12*dy(V)] + dy[C33*(dy(U)+dx(V))] + Fx = dx(b*Temp)
    dy[C12*dx(U)+C22*dy(V)] + dx[C33*(dy(U)+dx(V))] + Fy = dy(b*Temp)

In the "Plane-Stress" approximation, appropriate for a flat, thin plate
loaded by surface tractions and body forces IN THE PLANE of the plate,
we may write

    C11 = G
    C12 = G*nu
    C22 = G
    C33 = G*(1-nu)/2

where G = E/(1-nu**2)

E is Young's Modulus
and   nu is Poisson's Ratio.

The displacement form of the stress equations (for uniform temperature
and no body forces) is then (dividing out G):

dx[dx(U)+nu*dy(V)] + 0.5*(1-nu)*dy[dy(U)+dx(V)] = 0
dy[nu*dx(U)+dy(V)] + 0.5*(1-nu)*dx[dy(U)+dx(V)] = 0

In order to quantify the load boundary condition mechanism,
consider the stress equations in their original form:

dx(Sx) + dy(Txy) = 0
dx(Txy) + dy(Sy) = 0

These can be written as

div(P) = 0
div(Q) = 0

where P = [Sx,Txy]
and   Q = [Txy,Sy]

The "load" (or "natural") boundary condition for the U-equation defines
the outward surface-normal component of P, while the load boundary condition
for the V-equation defines the surface-normal component of Q. Thus, the
load boundary conditions for the U- and V- equations together define
the surface load vector.

On a free boundary, both of these vectors are zero, so a free boundary
is simply specified by

load(U) = 0
load(V) = 0.

Here we consider a tension strip with a hole, subject to an X-load.

}

Title "Plane Stress in a Compression Block with an Octagonal Hole"

select macsyma
select painthcopy
select printplots = on
ERRLIM = 0.0005

variables
u   { declare u and v to be the system variables }
v

definitions

mm=1e-3
Lx=20*mm

146

```
Ly=20*mm
side=Lx/6
notch=0.2*Lx
hole=0.45*Lx
rad=0.2*Lx
nu=0.25                   {Poison's ratio}
E=300e9                   {Young's Modulus}
c=E/(1-nu**2)
G=E/[2*(1+nu)]
dabs=sqrt(u**2+v**2)
ex=dx(u)
ey=dy(v)
exy=dx(v)+dy(u)          {Strains}
sx=c*(ex+nu*ey)
sy=c*(nu*ex+ey)
sxy=G*exy                {Stresses}

initial values

equations          { define the Plane-Stress displacement equations }

  dx[c*(dx(u) + nu*dy(v))] + dy[G*(dy(u) + dx(v))]  = 0
  dy[c*(dy(v) + nu*dx(u))] + dx[G*(dy(u) + dx(v))]  = 0

boundaries

 region 1
   start (0,0)
   load(u)=0
   value(v)=0
   line to (Lx/2,0)

   point value(u)=0

   load(u)=0
   value(v)=0
   line to (Lx,0)

   load(v)=0
   load(u)=0
   line to (Lx,0.5*Ly-0.5*notch)
   line to (Lx-0.866*notch,0.5*Ly)
   line to (Lx,0.5*Ly+0.5*notch)
   line to (Lx,Ly)

   load(v)=-43860000
   value(u)=0
   line to (0,Ly)

   load(u)=0
   load(v)=0
   line to (0,0.5*Ly+0.5*notch)
   line to (0.866*notch,0.5*Ly)
   line to (0,0.5*Ly-0.5*notch)
```

```
line to finish

            { Cut out a hole }
load(u)=0
load(v)=0
start(Lx/2-1.207*side,Ly/2-0.5*side)
line to (Lx/2-1.207*side,Ly/2+0.5*side)
line to (Lx/2-0.5*side,Ly/2+1.207*side)
line to (Lx/2+0.5*side,Ly/2+1.207*side)
line to (Lx/2+1.207*side,Ly/2+0.5*side)
line to (Lx/2+1.207*side,Ly/2-0.5*side)
line to (Lx/2+0.5*side,Ly/2-1.207*side)
line to (Lx/2-0.5*side,Ly/2-1.207*side)
line to finish

{load(U) = 0
load(V) = 0
start(0.5*Lx-side,0.5*Ly)
line to (0.5*Lx-0.5*side,0.5*Ly+0.866*side)
line to (0.5*Lx+0.5*side,0.5*Ly+0.866*side)
line to (0.5*Lx+side,0.5*Ly)
line to (0.5*Lx+0.5*side,0.5*Ly-0.866*side)
line to (0.5*Lx-0.5*side,0.5*Ly-0.866*side)
line to finish}

{load(U)=0
load(V)=0
start(hole-rad,hole)
arc(center=hole,hole) angle=-360 to finish}     {cuts out a big circle}

{load(U)=0
load(V)=0
start(hole-rad,Ly-hole)
arc(center=hole,Ly-hole) angle=-360 to finish

load(U)=0
load(V)=0
start(Lx-hole-rad,hole)
arc(center=Lx-hole,hole) angle=-360 to finish

load(U)=0
load(V)=0
start(Lx-hole-rad,Ly-hole)
arc(center=Lx-hole,Ly-hole) angle=-360 to finish}  {cuts out small circles}

monitors
   grid(x+U,y+V)     { show deformed grid as solution progresses }

plots              { hardcopy at finish: }
   grid(x+200*u,y+200*v)      { show final deformed grid }
   contour(u) as "x-position" pause
   contour(v) as "y-position" pause
   vector(u/dabs,v/dabs) as "displacement vector direction" pause
   vector(u,v) as "displacement"       { show displacement field } pause
```

```
  contour(ex) as "x-strain" pause
  contour(ey) as "y-strain" pause
  {contour(exy) as "xy-strain" pause}
  contour(sx) as "x-stress" pause
  contour(sy) as "y-stress" pause
  contour(sy) as "y-stress" zoom(0.75*Lx,0.375*Ly,0.25*Lx,0.25*Ly) pause
  {contour(sxy)as "xy-stress"}
  surface(sx) interactive
  surface(sy) interactive zoom(0.75*Lx,0.375*Ly,0.25*Lx,0.25*Ly)
 end
17689
```

THESIS PROCESSING SLIP

FIXED FIELD: ill. _____ name _____

index _____ biblio _____

► COPIES: (Archives) Aero Dewey Eng Hum

Lindgren Music Rotch (Science)

TITLE VARIES: ►☐ _____

_____

_____

NAME VARIES: ►☐ _____

_____

IMPRINT: (COPYRIGHT) _____

►COLLATION: _____149 p_____

_____

►ADD. DEGREE: _____ ►DEPT.: _____

SUPERVISORS: _____

_____

_____

___ __ _____

___ __ _____

___ __ _____

___ __ _____

___ __ _____

___ __ _____

NOTES:

_____ cat'r: _____ date:

►DEPT: MatSci&E   page: ► 540

►YEAR: 1996 ____ ►DEGREE: Ph.D.

►NAME: YOO, Jaedeok